Assessment of Optical Micro-AngioGraphy Technique to Image 3D Blood Flow within Microcirculatory Tissue Beds in vivo

Yali Jia

B.S., Yantai Normal University, China, 2001

Presented to the Department of Biomedical Engineering

And the Oregon Health & Science University

School of Medicine

in partial fulfillment of

the requirements for the degree of

Doctor of Philosophy

in

Biomedical Engineering

November 2010

Department of Biomedical Engineering

School of Medicine

Oregon Health & Science University

_____

CERTIFICATE OF APPROVAL

_____

This is to certify that the Ph.D. dissertation of

Yali Jia

has been approved

_____

Dr. Ruikang Wang, Ph.D.

Professor, Thesis Advisor*

_____

Dr. Nabil Alkayed, M.D. Ph.D.

Professor

_____

Dr. Andras Gruber, M.D.

Associate Professor

_____

Dr. Owen McCarty, Ph.D.

Assistant Professor

_____

Dr. Sandra Rugonyi, Ph.D.

Assistant Professor

Contents

List of Figures

brain tissue damage is shown by a typical histological section across the center of the injury site. The injury depth is around 1.5mm measured from the surface of the parenchyma. (C) is the schematic of the OMAG system used to collect the 3D micro-angiography of traumatic brain tissue in small animal model in vivo. CCD represents the charge coupled device, PC the polarization controller. 39

List of Abbreviations

ACS	anterior coronal suture
ANOVA	analysis of variation
BW	bandwidth
CBF	cerebral blood flow
CCD	charge coupled device
CMOS	complementary metal–oxide–semiconductor
CNS	central nervous system
CPP	cerebral perfusion pressure
CT	computed tomography
CVR	cerebral vascular resistance
CYP-2C	cytochrome P450-2C
DC	direct current
DOCT	Doppler optical coherence tomography
DOMAG	Doppler optical micro-angiography
ECM	extracellular matrix
EETs	eicosanoid epoxyeicosatrienoic acids
FDOCT	frequency domain optical coherence tomography
fMRI	functional magnetic resonance imaging
H&E	Hematoxylin and Eosin
HFUS	high frequency ultrasound
IAP	iodoantipyrine
ICP	intracranial pressure
KO	knockout
LDF	laser Doppler flowmetry

LDP	laser Doppler perfusion
LSI	laser speckle imaging
MABP	mean arterial blood pressure
MCA	middle cerebral artery
MCAO	middle cerebral artery occlusion
MPCM	multi-photon confocal microscopy
MRI	magnetic resonance imaging
OCT	optical coherence tomography
OMAG	optical micro-angiography
PAD	peripheral arterial disease
PBF	peripheral blood flow
PBS	phosphate buffered saline
PC	polarization controller
PCS	posterior coronal suture
PET	positron emission tomography
PRDOCT	phase-resolved DOCT
PVD	peripheral vascular disease
RBC	red blood cells
rCBF	regional cerebral blood flow
S.D.	standard deviation
SDH	subdural hemorrhage
SDOCT	spectral domain optical coherence tomography
sEH	soluble epoxide hydrolase
SEM	scanning electron microscopy
SLD	superluminescent diode
SLDI	scanning laser Doppler imaging

SS	sagittal suture
TBI	traumatic brain injury
TDOCT	time domain optical coherence tomography
UHS-OMAG	ultrahigh sensitive optical micro-angiography
VEGF	vascular endothelial growth factor
VP	venous pressure
vWF	von Willebrand factor
WT	wild type

Acknowledgements

First and foremost I would like to express my sincere gratitude to my thesis advisor, Dr. Ricky Wang. Without his guidance and persistent support, this dissertation would not have been possible. By enrolling me into his lab at OHSU as his first graduate student, Ricky accepted the daunting task of teaching me first-hand the most fundamental techniques used in the lab; and yes, this included how to handle a mouse and how to successfully obtain an optical image. I am grateful to him for giving me the freedom to explore and develop my own research directions. Additionally, his passion and constant enthusiasm for research have been extremely motivational to me. I appreciated his open-door policy that allowed for constant communication flow and his encouragement throughout my research. I have been extremely fortunate to have Ricky as my mentor.

I would like to thank my committee members for their valuable suggestions and careful assessment of my work. To Dr. Nabil Alkayed and Dr. Andras Gruber for opening wonderful collaboration environment through the brain imaging project. To Dr. Sandra Rugonyi for being available at a moment's notice to answer my questions on fluid flow and discuss my project with her insightful questions. To Dr. Owen McCarty for his endless encouragement throughout my study.

I am thankful to all of my colleagues and friends who made my stay at the university a memorable and valuable experience. I would like to give special thanks to Dr. Zhenhe Ma and Dr. Yi Wang for patiently explaining signal and optics knowledge. Lin An has been a great friend and teammate these past four years. I am very fortunate to have had the chance to work with him. Many thanks to Sawan Hurst for collaborating on the project and discussing the research, to Tim Zhi for helping with data collection.

Finally I thank my family for their years of support and encouragement. To my parents, for teaching me the determination and supporting me. To my lovely two daughters, Carol and Grace, for offering me endless energy and boundless strength on the work. Most of all to my husband, Kai, for being beside me through the good and bad times.

Abstract

Assessment of Optical Micro-AngioGraphy Technique to Image 3D Blood Flow within Microcirculatory Tissue Beds in vivo

Yali Jia

Doctor of Philosophy
Department of Biomedical Engineering
and the Oregon Health & Science University
School of Medicine

November 2010

Thesis Advisor: Dr. Ruikang Wang

Functional microcirculation, a system consisting of intact blood vessels perfused with red blood cells (RBCs), is required for the maintenance of O_2 and nutrient delivery to living tissues. Disruption of this system can be indicative of organ dysfunction and is characteristic of various disease pathologies. In vascular diseases, development and maintenance of functional microvasculature are crucial to facilitate the recovery of tissue functions in the body.

To quantify changes in microvascular perfusion in animal models of vascular diseases, it is necessary to directly visualize the microcirculation in vivo and quantify functional microvascular blood flow. Although non-invasive methods, such as magnetic resonance imaging (MRI) and ultrasound, have greatly advanced in temporal and spatial resolution, they remain limited in their ability to resolve vascular structures and to assess

microhemodynamics at the capillary level. For these reasons, our group has chosen optical microangiography (OMAG) to evaluate microcirculatory function in various disease models.

The broad goal of this research is to assess the OMAG technique to image 3D blood flow within microcirculatory tissue beds in vivo, so that it may be accepted as a standard imaging modality for preclinical study on vascular disease. This thesis addresses a number of animal models regarding blood flow under pathological conditions. In particular, we used OMAG for imaging cerebral blood flow (CBF) and peripheral blood flow (PBF). For CBF measurement, we included animal models that represent trauma, stroke and meningeal thrombosis. For PBF measurement, we studied diabetic peripheral neuropathy (DPN). In each animal model, (1) we optimize the scanning protocols and optics to test the feasibility of OMAG for 3D dynamic visualization of specific microvasculature; (2) we establish quantification algorithms to process OMAG data in order to obtain the parameters for tissue perfusion, such as blood volume, vessel density, blood velocity, etc.

Based on the OMAG results obtained in this study, we find that 3D OMAG can be a useful tool to non-invasively and quantitatively characterize cerebral tissue perfusion responses due to trauma, stroke and meningeal thrombosis, and peripheral tissue perfusion responses due to diabetes in mouse models. Based on these findings we further conclude that OMAG imaging method in conjunction with the quantifying methods developed on it will provide a new level of information regarding blood flow in the functions of human brain and other organs.

Chapter 1

Introduction

The blood flow within microcirculatory tissue beds offers a fascinating challenge for imaging modalities. The microvasculature is essential for the survival and well-being of all organs. It shows remarkable stability and organ specificity, and yet provides incredible potential for very rapid as well as sustained adaptation to changes. During embryonic development, precise programming of the microvasculature is critical for survival [1]. Adult tissues show functional changes in microvasculature that are coupled tightly with acute cellular demands and tissue activity and show structural changes that are associated with sustained changes in tissue requirements and are tightly linked with tissue remodeling. Examples for the former include hemodynamic response to functional brain activity and response to acute stress. The latter include physiological processes, such as the cyclic changes in the female reproductive organs and muscle buildup with exercise, as well as pathological processes, including wound healing and tumor growth. Aberrations in vascular development are frequently linked with pathologies, demonstrating the absolute requirement for homeostasis in vascular structure and function. Many internal or external agents that are involved in microvascular development and function have been discovered over the past decade and provide attractive targets for therapeutic intervention [2].

In order to demonstrate our aim directed toward the development of noninvasive imaging of the 3D blood flow within microcirculatory tissue beds, primarily using optical micro-angiography (OMAG), in this Chapter, we will specify the blood flow studied in this research as cerebral blood flow (CBF) and peripheral blood flow (PBF) and discuss their functions and characteristics and the popular diseases related to their abnormity.

1.1 Cerebral Blood Flow

1.1.1 Relationships between CBF and neurological activity

In mammals, brain tissue is undeniably the most sensitive of all tissue to energy deprivation and it is dependent on aerobic metabolism. The delivery of oxygen and metabolic substrate to the brain is maintained by a constant supply of blood known as cerebral blood flow (CBF). CBF, defined as the amount of blood in transit through the brain at one given point in time, is estimated to be 50mL/100g/min in a health adult [3]. If blood flow to the brain is compromised, even for a short time, loss of consciousness or irreversible neurological injury can occur. In rat, cortical activity ceases after only two minutes of complete oxygen deprivation [4]. This emphasizes the importance of the cerebral circulation in maintenance of normal neurological activity.
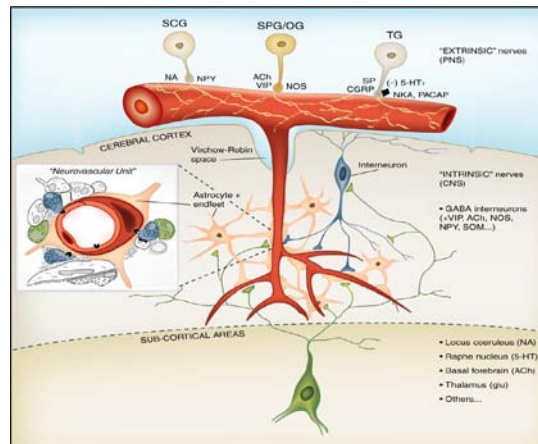
Figure 1.1 The communication between neurons and vessels. Vessels get the regulation from nerves, and they also supply the nutrition and oxygen to nerve cells. Inset: schematic representation of the "neurovascular unit" as seen at the electron microscopic level with the vascular [endothelium (medium red) and smooth muscle or pericyte (dark red)], astroglial (light red), and neuronal compartments. This graph is adapted from [5].

Meanwhile, cerebral arteries are innervated and regulated by perivascular nerves. In addition, there is a network of nerves within the brain itself, known as intrinsic innervations, which also can modulate CBF. **Figure 1.1** shows the communication

between neurons and vessels. Vessels not only supply the nutrition and oxygen to nerves cells, but also get the regulation from nerves.

1.1.2 Cerebrovascular autoregulation

If the viscosity of blood is not altered, CBF is determined by two factors, cerebral perfusion pressure (CPP) and cerebral vascular resistance (CVR). CBF is proportional to CPP divided by CVR as shown in **Eq. 1.1**:

$$CBF = CPP / CVR \tag{1.1}$$

CPP is defined as the pressure gradient in the brain; that is the difference between mean arterial blood pressure (MABP) and venous pressure (VP) as shown in **Eq. 1.2**:

$$CPP = MABP - VP \tag{1.2}$$

Since venous pressure is essentially equal to the intracranial pressure (ICP), therefore

$$CPP = MABP - ICP \tag{1.3}$$

Vascular resistance essentially reflects changes in diameter of the vasculature: vasoconstriction causes an increase in resistance, while vasodilation causes a decrease in vascular resistance. Under physiological conditions, CBF is mainly regulated by changes in the resistance of cerebral arteries. Unlike in many peripheral tissues where the microvasculature plays a dominant role, the larger cerebral arteries, such as the middle cerebral artery (MCA), provide approximately 45-50% of the overall resistance of the cerebral resistance of the cerebral circulation [6]. A number of factors contribute towards changes in cerebrovascular resistance including local chemical factors [7], and endothelial factors, such as vasoconstricting factors, and vasodilating factors.

The control of blood flow in the brain can be accomplished by CPP and CVR, however, CBF is largely independent of CPP within the range of MABP, due to the phenomenon known as cerebral autoregulation.

Cerebrovascular autoregulation is defined as the capacity of the brain to maintain a constant CBF in the face of variations in systemic arterial pressure. This homeostatic mechanism is effective between systemic arterial pressures of approximately 50 and 150

mmHg, known as the lower and upper limits of autoregulation, respectively [8]. When MABP is reduced, cerebral vessels will compensate by dilating until a maximum limit is reached. As is shown in **Fig. 1.2**, beyond this lower limit of autoregulation, CBF will decrease passively in response to further reduction in MABP. Similarly, a rise in MABP will cause cerebral vessels to constrict until upper limit of autoregulation is reached above which further increases in MABP result in an increase in CBF.
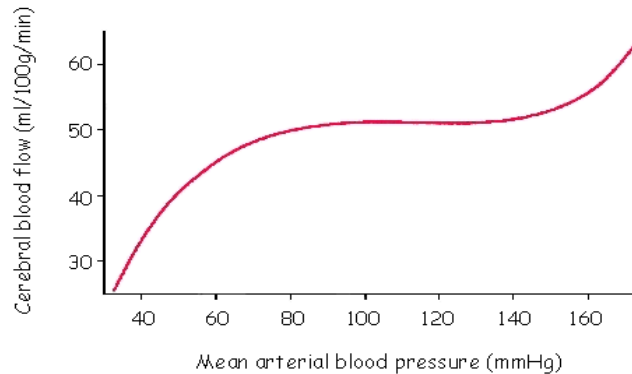
Figure 1.2 Autoregulation of CBF in relation to MABP. Over a wide range of blood pressure, CBF remains constant if metabolic demands are unchanged. Beyond the lower limit (~50mmHg), CBF will decrease passively in response to further reduction of blood pressure; and beyond the upper limit (~150mmHg), CBF will increase passively in response to further rise of blood pressure.

1.1.3 CBF perturbation in brain injury

Disease states of the brain may impair or abolish CBF autoregulation. Autoregulation is easy to be lost in severe head injury or acute ischemic stroke, leaving surviving brain tissue unprotected against the potentially harmful effect of blood pressure changes. Unlike brain trauma influencing CPP to destroy the CBF balance, ischemic stroke usually increases CVR by forming a clot to block cerebral arteries. This increase in resistance produces a decrease in the CBF and finally results in cerebral ischemic state.

1.1.3.1 Focal traumatic brain injury

Traumatic brain injury (TBI), traumatic injuries to the brain, also called intracranial injury, is the fourth leading cause of death in the United States and is the leading cause of death in persons aged 1-44 years [9]. TBI can result from a closed head injury or a

penetrating head injury and is one of two subsets of acquired brain injury. The other subset is non-traumatic brain injury (e.g. stroke, meningitis, anoxia). The principal mechanisms of TBI are classified as (a) focal traumatic brain damage due to contact injury types resulting in contusion, laceration, and intracranial hemorrhage or (b) diffuse traumatic brain damage due to acceleration or deceleration injury types resulting in diffuse axonal injury or brain swelling [10, 11] A focal traumatic injury resulted from direct mechanical impact is usually associated with brain tissue damage visible to the naked eye. A common cause of focal injury is penetrating head injury, in which the skull is perforated, as frequently occurs in auto accidents, blows, and gunshot wounds. The current increase in firearm-related violence and subsequent increase in TBI remains of concern to neurosurgeons in particular [11].

Improvements in the understanding of the mechanisms of injury may lead to improved outcomes. Outcome from TBI is determined by two substantially different stages [12]: (a) the primary damage (mechanical damage) occurring at the moment of impact. Primary damage exposes the brain tissue to shear forces with consecutive structural injury of neuronal cells and cerebral microvascular and endothelial cell damage [13]. The mechanism by which post-traumatic ischemia occurs at local trauma zone may be related with morphological injury (e.g. vessel distortion or vessel destruction) as a result of mechanical displacement [13]. (b) The secondary damage (delayed non-mechanical damage) represents consecutive pathological processes initiated at the moment of injury with delayed clinical presentation. Under physiological conditions, intact blood brain barrier forms a semi-permeable membrane. The rate of fluid movement (FM) between the cerebral capillaries (c) and brain parenchyma or interstitial fluid (if) is expressed by $FM = K_f [(H_c-H_{if})-(O_c-O_{if})]$, where H_c is capillary hydrostatic pressure, H_{if} is interstitial hydrostatic pressure, O_c is capillary osmotic pressure, O_{if} is Interstitial osmotic pressure and K_f is filtration coefficient. After TBI, big protein and electrolytes flow across membrane due to the disrupted blood brain barrier. Hence, flow movement is dominantly driven by hydrostatic pressure gradient, resulting in increased brain tissue volume and cerebral spinal fluid volume. Accordingly, CPP is decreased caused by the intracranial hypertension [14-17]. Cerebrovascular autoregulation (i.e. cerebrovascular

dilation in response to decreases in CPP) is an important mechanism to provide adequate CBF at that time. Once CBF autoregulation is impaired or abolished, consequently, cerebral hypotension can result in global or regional cerebral ischemia [15]. The presence of cerebral ischemia is associated with poor ultimate neurological outcome.

1.1.3.2 Focal ischemic brain injury

Focal ischemic brain injury is the clinical manifestation of ischemic stroke. Stroke, a cerebrovascular disease, is the third most common causes of mortality and morbidity in United States with 700,000 new or recurring cases annually [18]. It is already, and will continue to be, the most challenging disease. In stroke, the cerebrovascular system is impaired when the blood supply to a part of the brain is suddenly interrupted by occlusion (an ischemic stroke) or by hemorrhage (a hemorrhagic stroke) [19]. Ischemic stroke accounts for approximately 85% of all strokes and results from a thrombotic or embolic occlusion of a major cerebral artery (most often MCA) or its branches [20]. Ischemic stroke can further be divided into two main types: thrombotic and embolic. A thrombotic stroke occurs when diseased or damaged cerebral arteries become blocked by the formation of a blood clot within the brain. Clinically referred to as cerebral thrombosis or cerebral infarction, this type of event is responsible for almost 50% of all strokes. An embolic stroke is also caused by a clot within an artery, but in this case the clot (or emboli) was formed somewhere other than in the brain itself. Often from the heart, these emboli will travel the bloodstream until they become lodged and cannot travel any further. This naturally increases CVR and restricts the flow of blood to the brain and results in almost immediate physical and neurological deficits. Most commonly, the focal metabolic impairment and neurological dysfunction is restricted to a specific area, thus giving so call focal ischemic brain injury [21].

1.1.4 CBF restoration after brain injury

The vascular response to brain injury during intra-traumatic or intra-ischemic period [22] and the fundamental mechanism of CBF fluctuation and the CBF restoration during post-traumatic or post-ischemic phases [23] has been the focus of a great deal of research as it

is believed to play an integral role in reducing the risk for brain damage. It is generally believed that a thorough understanding of the mechanism of CBF alteration during or after brain injury will lead the way to aid the development of novel therapeutic strategies in their treatments. Advances in our understanding of the coupling of CBF and brain metabolism in these pathophysiologic conditions have highlighted a clear need for the ability to visualize and quantify dynamic cerebral blood perfusion and its response to novel brain injury therapies.

Also, it has been observed by ultrastructural studies and indicated by immunohistochemistry measurements that beside the recovery of global cerebral blood perfusion, the vessel remodeling (a vascular repair process) around traumatic or ischemic area is also involved in the restoration of CBF and then rehabilitation of injury [24, 25]. There are three ways of blood vessel formation in the body. Vasculogenesis means angioblasts differentiate into endothelial cells to form a vessel lumen. The primary vessels in the body are established by this way. Angiogenesis means new vessels are formed by sprouting or splitting from preexisting vessels. It is responsible for the development of vessels after birth. It is also required for pathological process, such as tumor growth, ischemic disease etc. Arteriogenesis refers to the enlargement of preexisting ipsilateral arterioles to form larger arteries which can deliver more blood to specific tissues. Vessel remodeling usually means angiogenesis or arteriogenesis. It also be suggested that therapeutic angiogenesis may repair damaged and leaky vessels, ameliorate vascular insufficiency and replenish ischemic tissue during inflammation and probably also provide direct beneficial effects on axonal remodeling or neural integrity, indicating a new paradigm for the treatment of neural disorders caused by brain injury [26].

Currently, extensive research goes into CBF restoration after focal brain injuries, however, it is difficult to say how it actually alter structurally and functionally in vivo as none of the studies to date have non-invasively visualized 3D cerebral blood perfusion at capillary resolution level.

1.2 Peripheral Blood Flow

1.2.1 Peripheral vascular system and its functions

Peripheral blood flow (PBF) refers to blood flow that occurs in the extremities as opposed to blood that flows to the brain, heart, lungs, and vital organs [27]. The peripheral vasculature is a branching, tapering network of distensible tubes. Blood enters the network from the heart at a pressure of about 100 mm Hg and at a flow rate of 4-6 liters/min in the resting adult human. The blood ejected from the heart during each systole, approximately 70 ml, is received by the aorta and large arteries, which constitute the reservoir and conduit portion of the arterial system. During diastole, the recoil of these elastic reservoirs provides a supply of arterialized blood under pressure to the periphery [28]. Peripheral vascular system consists of five types of vessels, arteries, arterioles, capillaries, venules and veins [29]. Arteries are a type of vessels with heavy elastic walls. Due to their elasticity, they convert intermittent heart pumping action to continuously maintained pressure. Thus, there is continuous capillary flow, despite the pulsating nature of cardiac ejection. Because of low resistance to flow, arteries distribute blood pumped by the heart to the microvascular bed. Arterioles and associated structures are sites of controlled resistance. They acting as variable resistance valves control the flow to individual vascular beds accordance with its needs. Capillaries are small vessels with 5-10 µm inner diameters. They are non-contractile and have a very thin wall (single cell layer), which promote exchanging substances between blood and interstitial fluid. Venules are small but larger than capillaries, in the order of 18 µm inner diameter. They collect blood from capillaries and also support diffusion between blood and interstitial fluid. Veins are large vessels which normally contain about 55% of body's total blood and can expel blood to the remaining circulation by vasoconstriction. They can aid in return of blood to the heart by rhythmic skeletal muscle contraction (muscle pump) and respiratory movements (respiratory pump).

The peripheral circulation carries out a variety of functions that maintain homeostasis [27]. Among these are delivery of nutrients to the tissue, removal of waste

products, maintenance of normal tissue fluid volume, bulk transfer between organs, and facilitation of the processes of food absorption and waste excretion in specialized organs. Generally, their function can be categorized into five types. First, they transport metabolic substrates from their source (e.g. alimentary tract, lungs, liver) to the tissues that utilize them (e.g. muscles). Second, they transport metabolic end products (e.g. carbon dioxide, urea, heat) to the organs that dispose of them (e.g. muscles, skin). Third, they transport endocrine from the organs that secret them to their target tissues. Fourth, they provide a short diffusion distance between the vascular system and the cells. Fifth, they contribute to maintaining the consistency of the cells' internal environment (e.g. interstitial fluid) which is called homeostasis.

1.2.2 Autoregulation of PBF

In keeping with the multiplicity of functions performed, blood flow in some organs is far above that required to meet local nutritional needs. Thus it seems inappropriate to assume that regulatory mechanisms are geared entirely to satisfying tissue nutritional requirements. In reality, regulation of the peripheral circulation involves a variety of central and local control mechanisms that serve to maintain organismic and local tissue homeostasis. It can be basically divided into extrinsic control performed by neurohumoral system and intrinsic control performed locally in the tissues and determined by the conditions in the immediate vicinity of the blood vessels [30].

Moment-to-moment regulation of vascular tone in individual organs is largely carried out by local control mechanisms that are not neural in nature. These mechanisms become apparent when local conditions, i.e., blood flow, intravascular pressure, or tissue metabolism, change. Autoregulation is the tendency for blood flow to remain constant in the face of changes in arterial pressure to the organ. It is seen in virtually all organs and tissues of the body. It is most pronounced in brain which we have described above. It is also quite prominent in skeletal muscle. Autoregulation could be explained as being due either to a pressure sensitivity of the arterioles (a myogenic response) or flow sensitivity (due to an accumulation or washout of vasodilator metabolites during the period of altered flow) [31].

One of the most fundamental principles of circulatory function is the ability of each tissue to control its own local blood flow in proportion to its metabolic needs [32]. Any intervention that results in an inadequate oxygen (nutrient) supply for the metabolic requirements of the tissues results in the formation of vasodilator substances which increase blood flow to the tissues. When the pressure increases to a tissue, the flow increases, and excess oxygen and nutrients are provided to the tissues. These excess nutrients cause the blood vessels to constrict and the flow to return nearly to normal despite the increased pressure. The feedback loop for metabolic regulation is shown in **Fig. 1.3**. In this feedback loop, vasodilator metabolites are released from endothelial cells in response to increased metabolic activity or decreased O_2 supply and diffuse to nearby arteriolar smooth muscle cells, where they cause relaxation. Relaxation of arteriolar smooth muscle cells increases diameter and blood flow, supplying more O_2 and other nutrients.
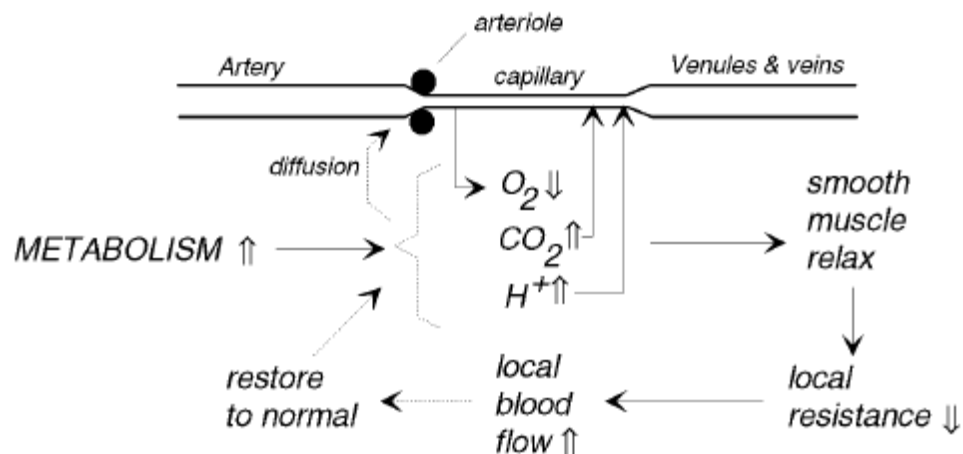
Figure 1.3 Feedback loop used to describe metabolic regulation of blood flow. Increased tissue metabolism reduces tissue PO_2. This leads to release of vasodilatory metabolites, relaxation of arteriolar smooth muscle, and decreased vascular resistance. This figure is adapted from [33].

1.2.3 PBF perturbation

Many medical conditions that afflict the heart may also or independently affect the network of arteries and veins that carry blood to and from the body's tissues. Such

damage is generally referred to as peripheral vascular disease (PVD). Arterial diseases may cause narrowing or blockage of vessels in the legs and other parts of the body distant from the heart (known as the periphery). In peripheral arterial vascular disease, however, the most common symptoms are leg pains from decreased circulation. The veins, which send blood from the limbs and other tissues back to the heart, are also vulnerable to a variety of disorders that can cause blood clots to form or inflammation to develop.

1.2.3.1 Peripheral arterial disease

PVD commonly referred to as peripheral arterial disease (PAD) [34], is a disease of the arteries that affects 10 million Americans and affects 12-20 percent of Americans age 65 and older. It can happen to anyone, regardless of age, but it is most common in men and women over age 50 [35]. PAD is a common circulation problem in which the arteries that carry blood to the legs and arms become narrowed or clogged. This interferes with the normal flow of blood, sometimes causing pain, but often causing no symptoms at all. The most common cause of PAD is atherosclerosis, often called "hardening of the arteries" [36]. Atherosclerosis is a gradual process in which cholesterol and scar tissue build up, forming a substance called "plaque" that clogs the blood vessels. In some cases, PAD may be caused by blood clots that lodge in the arteries and restrict blood flow. Left untreated, this insufficient blood flow will lead to limb amputation in some patients. In atherosclerosis, the blood flow channel narrows from the buildup of plaque, preventing blood from passing through as needed, restricting oxygen and other nutrients from getting to normal tissue. The arteries also become rigid and less elastic, and are less able to react to tissue demands for changes in blood flow. Many of the risk factors-high cholesterol, high blood pressure, smoking and diabetes-may also damage the blood vessel wall, making the blood vessel prone to diffuse plaque deposits [37].

The most common symptom of PAD is called claudication, which is leg pain that occurs when walking or exercising and disappears when the person stops the activity. Other symptoms of PAD include: numbness and tingling in the lower legs and feet, coldness in the lower legs and feet, and ulcers or sores on the legs or feet that don't heal.

1.2.3.2 Diabetic peripheral neuropathy

The perturbation of PBF sometimes occurs when a person has had diabetes mellitus for a long time. High blood glucose levels cause the endothelial cells lining the blood vessels to take in more glucose than normal (these cells do not depend on insulin). They then form more glycoproteins on their surface than normal, and also cause the basement membrane to grow thicker and weaker. The walls of the vessels become abnormally thick but weak, and therefore they bleed, leak protein, and slow the flow of blood through the body. Then some cells, for example in the retina (diabetic retinopathy) or kidney (diabetic nephropathy), may not get enough blood and may be damaged. Nerves, if not sufficiently supplied with blood, are also damaged which may lead to loss of function, which is usually called diabetic neuropathy [38].

Vascular and neural diseases are closely related and intertwined. Blood vessels depend on normal nerve function, and nerves depend on adequate blood flow. The first pathological change in the microvasculature is vasoconstriction. As the diabetic neuropathy progresses, neuronal dysfunction correlated closely with the development of vascular abnormalities, such as capillary basement membrane thickening and endothelial hyperplasia, which contribute to diminished oxygen tension and hypoxia. Neuronal ischemia is a well-established characteristic of diabetic neuropathy. Vasodilator agents can lead to substantial improvements in neuronal blood flow in the peripheral vascular system, with corresponding improvements in nerve conduction velocities. Thus, microvascular dysfunction occurs early in diabetes, parallels the progression of neural dysfunction, and may be sufficient to support the severity of structural, functional, and clinical changes observed in diabetic neuropathy [39].

1.2.4 PBF restoration

Blood perfusion restoration plays a prominent role for the survival of peripheral tissue suffered from circulatory aberration. In the adult organism, vessels grow either via capillary sprouting, a process called angiogenesis [26], or via in situ proliferation of preexisting arteriolar connections into true collateral arteries, a process we named arteriogenesis [40, 41]. Although capillary sprouting may deliver some relief to the

under-perfused territory, only true collateral arteries are principally capable of providing large enough amounts of blood flow to the ischemic area at risk for necrosis or loss of function. Arteriogenesis is by far the most efficient adaptive mechanism for the survival of ischemic limbs or other peripheral organs such as skin because of its ability to conduct, after adaptive growth, relatively large blood volumes per unit of time [42]. An increase in the number of capillaries, the result of stimulated angiogenesis, is unable to do that. Arteriogenesis differs from angiogenesis in several aspects, the most important being the dependence of angiogenesis on hypoxia and the dependence of arteriogenesis on inflammation. However, angiogenesis and arteriogenesis share several mechanisms of action, e.g., their dependence on growth factors. Whereas angiogenesis can be largely explained by the actions of vascular endothelial growth factor (VEGF), arteriogenesis is probably a multifactorial process in which several growth factors are orchestrated [43].

Recently the hindlimb ischemia models are frequently used to describe the PBF restoration. In these models, collateral growth (arteriogenesis) was usually restricted to the thigh, whereas capillary sprouting (angiogenesis) was observed in the calf muscles upon femoral artery occlusion. Both arteriogenesis and angiogenesis were initiated and showed proliferation after arterial occlusion. However, in clinical practice the endogenous angiogenic response is often suboptimal or impaired, e.g., by factors such as ageing, diabetes or drug therapies. Therapeutic angiogenesis or arteriogenesis is an application of biotechnology to stimulate new vessel formation via local administration of pro-angiogenic growth factors in the form of recombinant protein or gene therapy or by implantation of endothelial progenitor cells [44]. Numerous experimental and clinical studies have sought to establish "proof of concept" for the therapeutic angiogenesis or arteriogenesis in PAD, DPN or other peripheral vascular diseases using different treatment modalities.

However, how to evaluate the therapeutic treatment poses immense challenges for current vascular imaging techniques as none of them have non-invasively visualized and quantified 3D peripheral blood perfusion at capillary resolution level.

1.3 Thesis outline

This thesis aims to investigate the utility of OMAG for non-invasive monitoring of changes in microcirculation within both cerebral and peripheral tissue beds.

In this thesis, Chapter 2 presents the microvascular imaging methods for visualizing or quantifying blood flow within microcirculatory tissue beds. We summarize the current widely used techniques in small animal models for preclinical purpose. We introduce optical micro-angiography (OMAG), the system used in this study, describe its basic principles and report its validation results for quantification of blood flow in vitro or in vivo. We also briefly described the recent generations of OMAG: Doppler OMAG (DOMAG) and ultrahigh sensitive OMAG (UHS-OMAG).

Chapter 3 details three cerebral experiments using OMAG and quantification algorithms developed. In trauma experiment, we demonstrate OMAG can in vivo monitor post-traumatic revascularization and evaluate agents that promote this process by quantifying the restored blood volume in injury site. In stroke experiment, we demonstrate OMAG can evaluate in vivo vascular response during intra-ischemic period by visualizing and quantifying residual blood volume and track neovascularization in real time in the post-ischemic period by longitudinally imaging and measuring vessel density. In meningeal thrombosis experiment, we show UHS-OMAG method is able to dynamically visualize meningeal microcirculation decoupled from the cortical blood flow and chronically measure blood velocity, vessel diameter, flow rate and blood volume during thrombotic event.

Chapter 4 details one peripheral experiment using OMAG and quantification algorithms developed. OMAG is utilized to characterize blood perfusion of peripheral nerve in diabetic mice. The results indicate the potential of OMAG to assess the blood supply of nerve involved in the pathology and treatment of peripheral diabetic neuropathy.

Chapter 5 summaries our findings and contributions, and provides recommendations for future investigation.

Chapter 2
Vascular Imaging Methods

In characterizing the cerebral and peripheral vascular diseases in humans, the guiding study is the visualization of animals which faithfully mimic the clinical symptoms. Preclinical vascular imaging modalities have long been crucial to the researcher in observing changes, either at the macro- or micro-vessel level, in animals responding to physiological or environmental changes. Imaging modalities that are non-invasive and in vivo have become especially important to study animal models longitudinally.

The discussion in the previous chapter motivates the need for non-invasive visualization and quantification of microvascular blood flow, primarily as a standard tool for monitoring vascular diseases and the response to their therapies. In order to help illustrate why currently available techniques are insufficient for the task we present a brief review of vascular imaging modalities.

2.1 Current vascular imaging methods

Firstly, we need be aware of the important parameters commonly used to describe the specific tissue perfusion. Then we will review the corresponding available methods to acquire these parameters. To my best knowledge, usually, four parameters are used to characterize tissue perfusion in experimental studies. They are vessel morphology, blood flow volume, blood flow rate, and blood perfusion rate. **Table 2.1** summarizes the definitions of these important perfusion parameters. In literatures, people like to use two terminology "blood volume" and "blood flow". Blood flow means either blood flow rate or perfusion rate. Here we clarify them. Blood flow rate means blood volume per unit time. Blood perfusion rate means flow rate is divided by tissue mass.

Microscopic methods to evaluate vessel morphology include scanning electron microscopy (SEM), confocal and multi-photon confocal microscopy (MPCM). SEM is performed by first casting the vascular network with a polymer which hardens inside

blood vessels. The tissue is subsequently eroded away and imaged with a scanning electron microscope, which yields 3D information on vessel dimension, branching and tortuosity, defined as the ratio of the distance between two points in the vascular network measured along the blood vessel and the corresponding geometric distance between the two points (see **Table 2.1**). In one recent study this technique was used to analyze the age-dependent morphological and architectural changes of the cerebral vasculature of APP23 transgenic (tg) mice which mimic Alzheimer's disease [45]. The study demonstrated vessel eliminations forming holes associated with angiogenesis in old APP23 tg mice relative to wide-type mice. Representative images are shown in **Fig. 2.1**.

Table 2.1 Four important perfusion parameters and their definitions

Parameters		Definition
1.Vessel Morphology	Vessel diameter (μm)	D_v=Inner diameter at vessel cross-section
	Vessel density (ratio, %)	Geometrical length of all vessels within VOI divided by volume of VOI
	Tortuosity (ratio, %)	Total pathlength of a vessel divided by the linear distance between its endpoints
2. Blood flow volume (μL/g)		Volume of blood within VOI divided by the mass of VOI
3. Blood flow rate (μL/s)		$V = v_m \pi R^2$, where V_m is the mean velocity at vessel cross-section and $R=D_v/2$
4. Blood perfusion rate (μL/g/s)		Net blood flow through the VOI divided by the mass of VOI

Studies like this help demonstrate the power of SEM as a tool to assess microvascular morphology. However, it also comes with some practical limitations, specifically: (1) SEM cannot be performed longitudinally (2) SEMs are costly and not widely available.
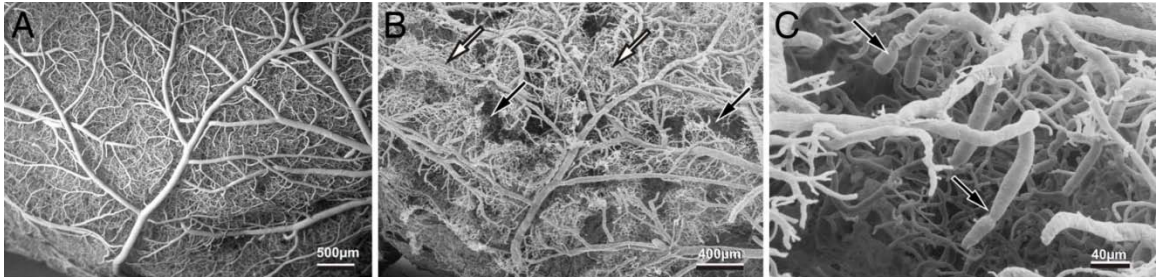
Figure 2.1 Vessel deformation and elimination imaged by SEM, adapted from [45]. (A) Overview of the left anterior cortex of a 18-month-old APP23 WT mouse. (B) In comparison, an 18-month-old APP23 tg mouse. The missing microvasculature is forming holes (black arrows) in the dense vascular network. (C) Detail of a hole illustrating the multitude of typical vessel deformations.

Much more practical and more widely available than SEM are light based microscopes. These can be used in a limited set of in vivo preclinical models, such as mouse ear, retinal imaging, dorsal and cranial window chamber models, to perform longitudinal microvascular imaging. Specifically, intravital MPCM can be used in conjunction with fluorescently labeled dextrans to obtain 3D images of the microvascular network. This technique has been used a number of preclinical studies involving CBF and PBF to evaluate vascular response and effectiveness [46, 47]. A typical example of an intravital fluorescence confocal image from mouse cortical region under cranial window is shown in **Fig. 2.2**. Standard metrics used to quantify vascular networks obtained with MPCM are vascular density, vessel diameter, branching points and vessel tortuosity. MPCM, like SEM, suffers from a number of drawbacks that makes it impractical for large preclinical studies (1) it is time consuming; scanning a 5mm×5mm region takes over one hour (2) it requires removal of intervening tissues to access vascular layers since its imaging depth is only up to 200 μm, which is not desirable for repeated and long-term imaging studies (3) it requires injection of fluorescent tissue markers, which may complicate the interpretation of the results
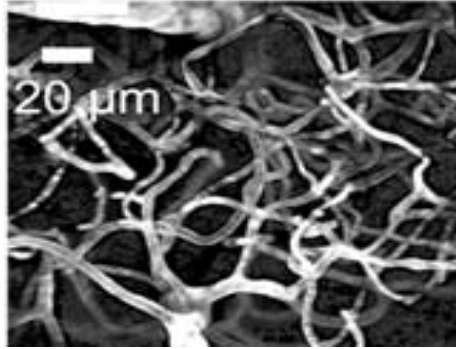
Figure 2.2 Dorsal view of the microvasculature from mouse cortical region (maximal intensity projection) imaged by MPCM. This image is from 100 planar scans acquired every 2 µm, adapted from [46].

Due to the limitation of intravital confocal microscopy and the limited number of suitable animal models, the vast majority of preclinical studies involving measurements of vascular response still rely on animal sacrifice followed by histochemical staining with CD31 or von Willebrand factor (vWF), and quantitative analysis using parameters such as Mean Vascular Density (MVD, number of vessel per unit area) and Luminal Vascular Area (LVA, the cross sectional area of vasculature in the stained histological section). Functionality of blood vessels can also be assessed using intravital tracers (fluorescent lectins) that are injected into the circulatory system prior to tissue fixation. However, the obvious limitation of histochemical staining techniques is that only a single time point or snapshot of the vascular network is obtained and the longitudinal effects of disease progression and reponse to therapy cannot be followed in a single animal. Furthermore, 3D parameters to quantify the vascular structure are difficult to obtain from a stack of histological sections, primarily due to physical processing artefacts.

Preclinical imaging methods such as micro magnetic resonance imaging (micro-MRI), micro computed tomography (micro-CT), micro positron emission tomography (micro-PET) and high frequency ultrasound (HFUS) all have the ability to longitudinally image deeply seated tissue, but lack the spatial resolution to actually resolve microvasculature in the 10-50 µm diameter range and, therefore, are unable to assess the full 3D vasculature. However, each of these methods does have the capability to make blood volume measurements through the use of various contrast agents. MRI

macromolecular contrast agents such as superparamagnetic iron oxide particles [48] and gadolinium-labled albumin, dendrimers or liposomes can be used to estimated functional cerebral blood volume [49]. However, due to the low molecular weight of the iodinated contrast agents, there is rapid diffusion into the surrounding tissue, making measurements inaccurate in the absence of a blood brain barrier. PET can be used to measure blood volume by inhaling small amounts of carbon monoxide composed of radioactive isotopes ^{11}C or ^{15}O [50]. The carbon monoxide permanently binds to red blood cells, which distribute according to the vascular volume. HFUS can be used in conjunction with microbubbles composed of a hydrophobic shell that encapsulates various types of perfluro hydrocarbon gas [51]. The microbubbles can be burst using HFUS, yielding a strong transient signal that reflects the microvascular blood volume.

In order to obtain the blood flow information besides vessel morphology, attention has been paid to some optical methods, such as laser speckle imaging (LSI) [52] and scanning laser Doppler imaging (SLDI) [53] techniques. In LSI, speckle contrast is a measure of speckle visibility, which is related to the motion of the scattering particles and therefore blood flow. A relative blood-flow image was then obtained by using speckle-contrast values. A typical example of LSI used for CBF measurement is shown in **Fig. 2.3**. Laser speckle images reflect local standard deviation of speckle patterns divided by the mean gray value. Occlusion of the right MCA results in a large blood flow deficit. Actually, laser Doppler flowmetry (LDF) is a widely used method to detect blood flow or flux in small animal models. LDF is a non-invasive technique based on the well-known Doppler shift principle for detecting changes of blood flow at a single point. Now SLDI extends this technique by scanning a laser beam across the tissue to generate a spatial map of perfusion with hundreds or thousands of measurement points per scan, depending on the area scanned [54]. This technique has proved to be of value in assessing CBF or PBF fluctuations [55]. Both LSI and SLDI are based on the Doppler effect that is induced by the moving blood cells in the micro-vessels, and more importantly, they provide longitudinal images. With these approaches, high flow sensitivity (~10 μm/s) is typically achieved. However, these optical imaging techniques do not have the depth-resolved

capability to image 3D microvasculature. Another apparent drawback of them is the relative blood flow values.
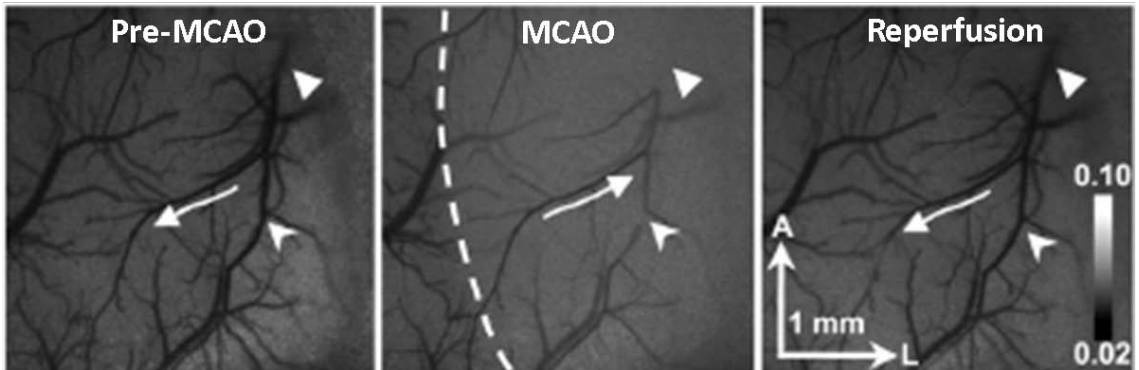
Figure 2.3 Regional assessment of cortical blood flow in mice using LSI, adapted from [47]. Laser speckle images reflect local standard deviation of speckle patterns divided by the mean gray value. Occlusion of the right MCA results in a large blood flow deficit. The white arrowheads indicate the blood vessel flowing before middle cerebral artery occlusion (MCAO) and after reperfusion, and stalled during MCAO. The white arrows show the direction of blood flow.

Recently, photoacoustic microscopy [56] is another promising imaging technique that provides the volumetric imaging of microcirculations deep within the brain of small animals, and dynamically measures blood volume and relative blood flow. This technique relies on the transient optical energy deposition within blood (i.e., due to light absorption) and subsequent detection of acoustic emission from the blood volume to achieve blood vessel isolation for imaging. Though it has high enough penetration depth (>1 mm), the relatively low spatial resolution (~50 μm) makes it difficult to resolve the capillary blood vessel networks, which requires an imaging resolution at ~10 μm.

Currently, autoradiographic is the only gold standard method used in preclinical study to identify the endpoint blood flow information, blood perfusion rate (μL/g/s). For example, ^{14}C-iodoantipyrine (IAP) autoradiography [57] is widely used for CBF quantitative measurement. Autoradiography is performed by first injecting radioactive tracer at a constant flow rate. The brain tissue is subsequently removed and sectioned into coronal slices, on which tracer's concentration can be determined. The localized tracer

concentration is proportional to the tissue localized perfusion rate. However, undoubtedly this imaging method is of limited use in delineating the dynamic vascular evolution.

2.2 The imaging system used in the study

An ideal modality to image and quantify microvascular perfusion in 3D should have a high sensitivity and specificity for the detection of moving red blood cells (RBC), and be able to detect RBC in all vascular beds with high target-to-background ratios. To monitor dynamic blood flow longitudinally, it is imperative that this system is non-invasive and reproducible, can detect blood flow changes sensitively and rapidly.

Recent study has shown the DOCT is able to characterize the dynamic blood flow with high-resolution and high-velocity sensitivity, especially in human retina. DOCT is a functional extension of optical coherence tomography (OCT), which is a non-invasive, three dimensional, interferometric imaging technique with a high resolution approaching that of conventional histology within highly scattering sample, such as biological tissue [58]. OCT is analogous to ultrasound, except that near infrared light is used as opposed to sound, and its imaging contrast is based on optical properties of tissue rather than acoustic properties. Because of the use of optical wavelengths, OCT provides an imaging resolution that is of an order of magnitude higher than that of ultrasound [59-61]. Standard OCT utilizes only the amplitude of back-scattered light as a function of depth within the tissue, whereas DOCT uses the additional phase information of the OCT signals to monitor the velocities of moving particles in the back-scattered spectrum. This is based on the principle that the Doppler frequency shift of the light that is backscattered from the moving objects within a sample is either added to or subtracted from the probing optical frequency, depending on the flow direction [62]. Because DOCT is built on the phase assessment of OCT signals, it is inherently sensitive to phase stability caused by both the system and the measurement environments, e.g. sample movement.

To overcome the problems involved in DOCT, we recently developed a novel imaging technique, OMAG that is capable of imaging dynamic blood flow, down to

capillary level resolution, within tissue beds up to 2mm beneath the surface [63]. Imaging contrast of blood perfusion in OMAG is based on endogenous light scattering from moving blood cells within biological tissue; thus, no exogenous contrast agents are necessary for imaging. In OMAG a constant modulation frequency is introduced in the spectral interferograms. This make it possible to use the mathematical properties of Hilbert and Fourier transformations of real-valued interferometric signal, then to separate the moving scattering elements, such as flowing blood cells, from the static elements, such as bulk tissue, within an illuminated tissue [63]. In essence, OMAG mathematically maps the backscattered optical signals from the moving particles into one image – that is, the blood flow image – while it simultaneously maps the backscattered optical signals from the static particles into a second image, which is the microstructural image. Because it is not built on the phase assessment of OCT signal, OMAG is not sensitive to the environmental phase stability and has higher resolution and higher sensitivity than DOCT for *in vivo* imaging.

2.2.1 Doppler Optical Coherence Tomography

Doppler OCT was developed that essentially combines OCT with the well known laser Doppler velocimetry [64, 65]. By relying on the Doppler frequency shift that is imposed on the light when the light interacts with a moving particle, i.e., the Doppler effect, DOCT provides an optical tool to quantitatively evaluate the velocity information of flow within functional blood vessels in a depth-resolved manner. Due to its relevance to OMAG, we will discuss it before we explain OMAG technique.

For a typical DOCT as illustrated in **Fig.2.4**, according to the Doppler principle, the optical wave-vector reflected from the moving particle, k_d, will be modulated by the velocity projection along the beam direction with a Doppler shift, Δf, compared with the initial optical wave-vector, k_0. Δf could be presented as the following equation:

$$\Delta f = \frac{2}{2\pi}(k_d - k_0) \times u\cos\theta \qquad (2.1)$$

If the Doppler shift, Δf, of the back scattered light from the moving particle is determined and the angle, θ, is known *a priori*, then the velocity of the moving particles can be directly evaluated by,

$$u = \lambda_0 \frac{\Delta f}{2\cos\theta}$$

(2.2)

Where λ_0 is the central wavelength of the light source.
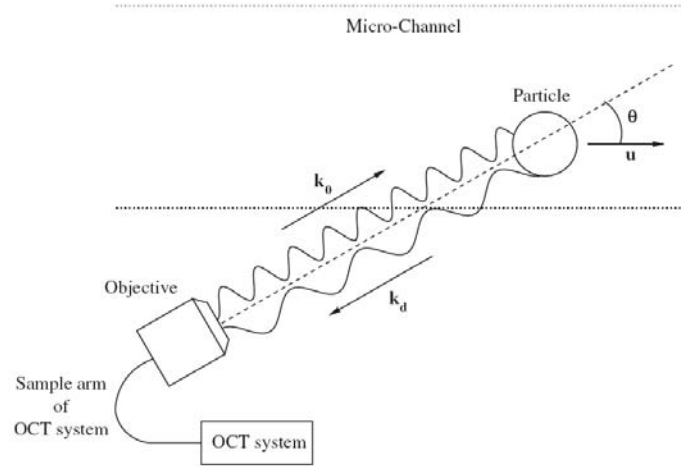
Figure 2.4 Schematic for the operation of Optical Doppler Tomography. The OCT system is the same as described in [8]. The angle between incident light beam from the sample arm and the flow direction is set at angle θ, k_0 is the initial optical wave-vector before the light hit the moving particle, while kd is the modulated optical wave-vector reflected from the moving particle. u is the velocity of moving particle.

To extract the Doppler shift, the phase-resolved DOCT is developed, first in the time domain OCT [66-68], and later in Fourier domain OCT [69-73]. Because of the significant advantage in imaging speed and sensitivity of frequency domain OCT (FDOCT) over time domain OCT (TDOCT), the FDOCT method is now becoming increasingly adopted in many *in vivo* imaging applications. In Fourier domain phase-resolve DOCT, the acquired spectral interferogram, $I(k)$, was Fourier transformed to generate a depth-resolved complex OCT signal, $\tilde{I}(z) = FFT(I(v)) = A(z)\exp(i\Phi(z))$, where k is the wavenumber and z is the depth coordinate. The magnitude $A(z)$ is used to generate cross sectional microstructure image of the sample which is the standard OCT

image, while the phase difference between adjacent A-lines, $\Delta\Phi(z)$, is used to obtain velocity map [70, 72].

$$u(z) = \Delta\Phi(z,\tau)\frac{\lambda_0}{4\pi\tau\cos\theta} \tag{2.3}$$

Where τ is the time delay between adjacent A-lines.

Using phase-resolved method, DOCT has shown to achieve high speed, high resolution cross sectional, microstructural image and the velocity image, simultaneously. The axial resolution is dependent on the coherence length of the light source used, while the lateral resolution is determined by the probe beam spot size on the sample. The velocity sensitivity is dependent on a number of factors, such as the time delay between adjacent A-lines, the system SNR, optical properties of the sample, as well as the Doppler angle θ.

2.2.2 Optical Micro-Angiography

OMAG is a functional extension of FDOCT. The key difference between OMAG and FDOCT is that, in OMAG, the spatial interferogram in the lateral direction (B-scan) is modulated with a constant frequency that can separate the moving and static scattering components within the sample. This modulation frequency can be introduced by mounting the reference mirror in the reference arm onto a linear Piezo-translation stage, which moves the mirror at a constant velocity across the B-scan (i.e., x direction scan), or simply via inherent scattering fluid flow within the sample.

We achieved this by mounting the reference mirror in the reference arm onto a linear Piezo-translation stage that moved the mirror at a constant velocity across the B-scan (i.e., the x direction scan). However, the latest version of OMAG utilizes the spatial modulation frequency provided by the inherent blood flow rather than reference arm modulation.

2.2.2.1 OMAG theory

In OMAG/FDOCT, the camera records the spectral interference fringe signal formed between the reference light and the light backscattered from within sample. Because the light backscattered from the sample is quite weak compared to the light reflected from the reference mirror, we do not consider the self cross-correlation between the light backscattered from different positions within the sample. We also do not consider the direct current (DC) signals because they do not contribute to useful OMAG signals. As a consequence, it can be written as a function of wavenumbers k and time variable t that relates to the position of focus beam spot on the sample.

$$I(k_j, \ t) = 2S(k_j)E_R \int_{-\infty}^{\infty} a(z,t)\cos(2k_j nz)dz \qquad (2.4)$$

where k_j is the wavenumber of the light captured by the jth detector (pixel) of the charge coupled device (CCD) camera, I is the light intensity, $S(k_j)$ is the spectral density of the light source at k_j, n is the refractive index of the sample, a is the magnitude of the backscattered light.

It is clear that **Eq. (2.4)** is constant if the sample is totally optically homogeneous, which means that $a(z,t)$ and n do not vary within the entire sample. If this is the case, then the spatial frequency components of the sample in lateral direction presented by Eq. (2.4) will be a delta function, shown as a black arrow in **Fig. 2.5 (A).** However in real situations, our imaging sample is often optically heterogeneous, which means that $a(z,t)$ and n are functions of time variable t. Thus, Eq. (2.4) can be expressed as:

$$I(k_j, \ t) = 2S(k_j)E_R \int_{-\infty}^{\infty} a(z,t)\cos(2k_j n(z,t)z)dz \qquad (2.5)$$

As a consequence, **Eq. (2.5)** is not constant anymore. The intensity captured by the CCD camera will be modulated by the heterogeneous properties of the sample along each B-scan. The spatial frequency components of a static tissue sample, which we call the heterogeneous frequencies, will exhibit as a randomly distributed function around zero frequency with a bandwidth of BW, as shown in gray curve in **Fig. 2.5 (B)**.

On the other hand, the moving particle at a velocity v, produces a frequency shift, which is caused by the Doppler effect of the moving particles and shifts them away from

the heterogeneous frequencies of the static tissues. This is expressed as **Eq. (2.6)** and illustrated in **Fig. 2.5 (C)**. The red curves are the Doppler beating frequency part.

$$I(k_j, \ t) = 2S(k_j)E_R\left[\int_{-\infty}^{\infty} a(z,t)\cos(2k_j n(z,t)z)dz + a(z_1,t_1)\cos\left[2k_j n(z_1,t_1)(z_1 - vt)\right]\right] \quad (2.6)$$
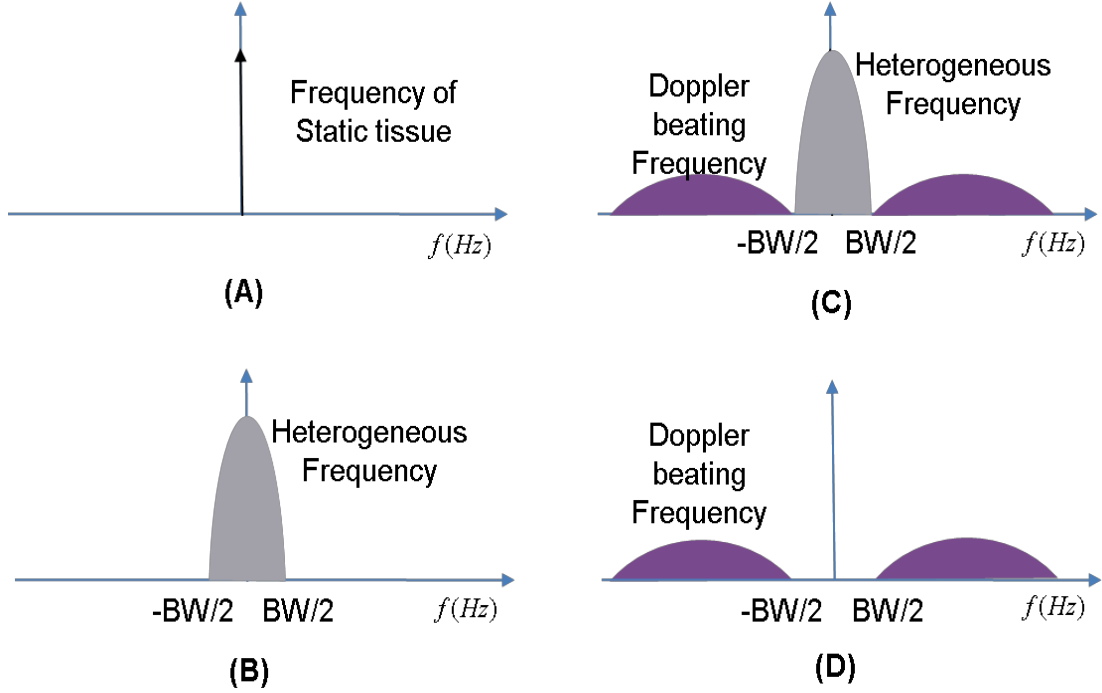
Figure 2.5 Diagram of frequency components for different tissue sample (A) an ideal tissue sample (optically homogeneous sample) with no moving particles; (B) a real tissue sample (optically heterogeneous sample) with no moving particles; (C) a real tissue sample (optically heterogeneous sample) with moving particles.(D) moving particles only. This figure is adapted from [74].

Next, the structural signal is filtered out in the frequency domain. The cut-off frequency, $fc = BW/2$, which depends upon the heterogeneity of the static scatterers. Now the remaining flow signals can be expressed as **Eq. (2.7)** and illustrated in **Fig. 2.5 (D)**

$$I(k_j, \ t) = 2S(k_j)E_R a(z_1,t_1)\cos\left[2k_j n(z_1,t_1)(z_1 - vt)\right] \quad (2.7)$$

Then we use the Hilbert transform to convert the flow signal to an analytic signal, which includes both the amplitude and phase of the flow signal. For the flow signal, the inverse Fourier transforms have positive and negative frequencies. After inverse transforming from the frequency domain, we apply the conventional spectral Fourier transform along

the depth direction to retrieve the strength of the flow signal. Based on the signal processing, the real flow signal is transformed to an analytic signal by the Hilbert transform, which enables the bidirectional flow configuration. In other words, the positive and negative flows can be separated in different imaging planes.

2.2.2.2 OMAG system setup

Figure 2.6 shows a schematic of a typical OMAG system based on the spectral domain OCT system. In this case, the system typically employs a superluminescent diode (SLD) as the light source, with its bandwidth and central wavelength determining the axial resolution of the system. The light eliminated from the SLD is coupled into a fiber based Michelson-based optical interferometer where it splits into two arms, the reference arm and the sample arm. In reference arm, the mirror is either stationary or mounted on a piezo-stage. In the sample arm, the light is delivered onto the sample by a probe, in which a pair of X-Y galvanometer scanners is used to achieve 2D scanning. The collimating and objective lens in the probe determine the lateral resolution of the system. The light back scattered from the sample and reflected from the mirror is then collected by the fiber coupler and delivered into a high speed spectrometer for capturing the spectral interferograms. The spectral resolution in the spectrometer, together with the wavelength of the broadband source, determines the maximum detectable range of the system. Because the whole system is based on the optical fibers, polarization controllers (PC) are often used in the reference arm, sample arm and/or detection arm in order to maximum the spectral interference fringe contrast at the detector.

For the first version OMAG technology, the key point is the introduction of modulation frequency, which will make it feasible to separate the moving signals from the static background tissue signals. Previously, there are two methods from our group to achieve this purpose. The first one is mounting the reference mirror onto a linear pizeo-stage [63, 75], which moves the mirror with a constant velocity during one B-scan. Another approach is to offset the incident beam of the sample arm away from the pivot of the x scanner [76]. For the latest version OMAG, this technique works on inherent

Doppler beating frequency rather than the additional modulated frequency, therefore current OMAG system is same as FDOCT system.
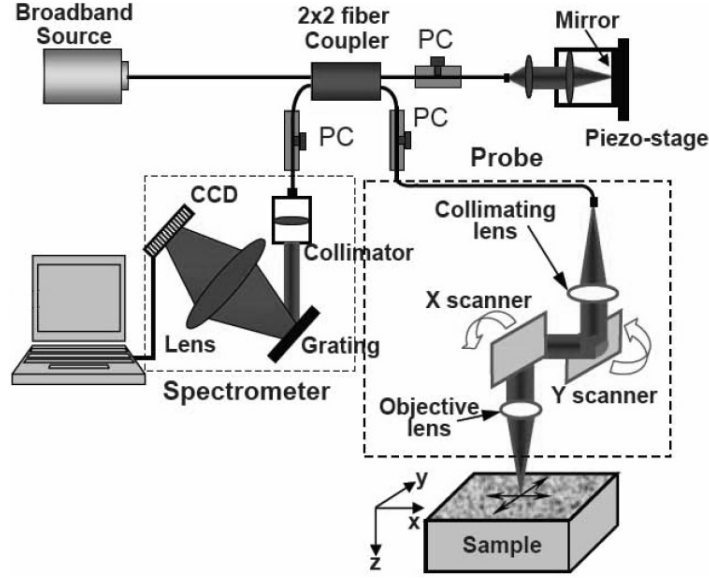
Figure 2.6 Schematic of the OMAG system used to collect the 3-D spectral interferogram data cube to perform the 3-D angiogram of thick tissue in vivo. CCD: the charge coupled device, PC: the polarization controller.

2.2.3 Doppler OMAG

The key advantage of OMAG is that only the signals backscattered by the functional blood appear in the OMAG flow output plane; this makes the blood flow imaging almost free of artifact-induced noise. However, the early version of OMAG is incapable of providing flow velocity information like phase-resolved DOCT can. This is because, in the OMAG flow image, the regions that are occupied by microstructural signals are rejected by OMAG. Thus, the required correlation between the adjacent A-scans within the static tissue regions are totally lost, leading to a rather noisy appearance in the output plane of flow velocity.

$$I(k_j,\ t) = 2S(k_j)\left\{E_R \int a_0 \cos(2k_j n_0 z)dz + E_R a(z_1,t_1)\cos\left[2k_j n(z_1,t_1)(z_1 - vt)\right]\right\} \qquad (2.8)$$

To overcome this, we digitally reconstructed an ideal static background tissue [the first term in **Eq. (2.8)**] that is totally optically homogeneous to replace the real heterogeneous tissue sample. This tissue provides a constant background signal that

makes the adjacent A-scans totally correlated, leading to a dramatic increase of the phase signal-to-noise ratio for the phase-resolved signals that represent flow velocities. This method inherits the advantages of both OMAG and DOCT.

In ref.[74], we then demonstrated the feasibility of Doppler OMAG (DOMAG) for imaging cerebral blood perfusion in mice *in vivo*. We also showed that the in vivo performance of DOMAG imaging of blood flow is superior to the traditional DOCT. To show the advantages of DOMAG in imaging the fluid flow velocities over DOCT in tissue engineering field, in Chapter 5, we compared DOMAG and DOCT images evaluated from a scanned tissue volume from both a fluid flow phantom and an engineered construct.

2.2.4 Ultra-high sensitive OMAG

Previous OMAG methods have demonstrated flow sensitivity (~160μm/s) within the reach for imaging microcirculations within biological tissue beds, limited by the optical heterogenous property of tissues. However, the blood flow in some tissues, for example cutaneous blood flow [77], cochlear blood flow and meningeal blood flow [78], particularly in their capillaries, is slow. In order to visualize the capillary plexus with slow velocity, our group designed an improved and ultrahigh sensitive OMAG (UHS-OMAG) system [77].

The essential principle of UHS-OMAG is the same as the traditional one [20], except that the OMAG algorithm is applied on slow axis (C scan direction) rather than fast axis (B scan direction). So, the scanning protocol is modified in UHS-OMAG. In order to keep the imaging time at the same order as conventional OMAG, we need to acquire low density B-scan frame and high density C-scan, which is opposite in OMAG. Then, Using high pass filtering along C-scan to isolate optical scattering signals between the static and moving scatters, the maximum resolvable velocity that is not wrapped is determined by the time spacing, Δt, between adjacent B frames, according to $v = \lambda/2n\Delta t$, where λ is the central wave length of the light source and n is the refractive index of the sample. The minimal flow velocity that can be detected by the system is

determined by the system phase noise floor, S, of the OMAG/OCT system by $\sigma_{\Delta\varphi}^2 = 1/S$ [74]. Thus, with the current system signal to noise ratio at 85dB, the minimum detectable flow velocity would be ~4.0 μm/s.

2.2.5 Validation of OMAG

Since OMAG has high spatial resolution and velocity sensitivity, it has been used in different applications to visualize the micro-circulatory vessel networks within the tissue bed. Combined with Doppler method, OMAG also can provide axial velocity values; and then using the 3D vasculature, OMAG will be a promising method to calculate parameters related to blood flow, such as flow rate (μL/s) and perfusion rate (μL/g/s). In this section, we will briefly discuss two important experiments which were designed to validate whether OMAG can quantify blood flow in vitro and in vivo.
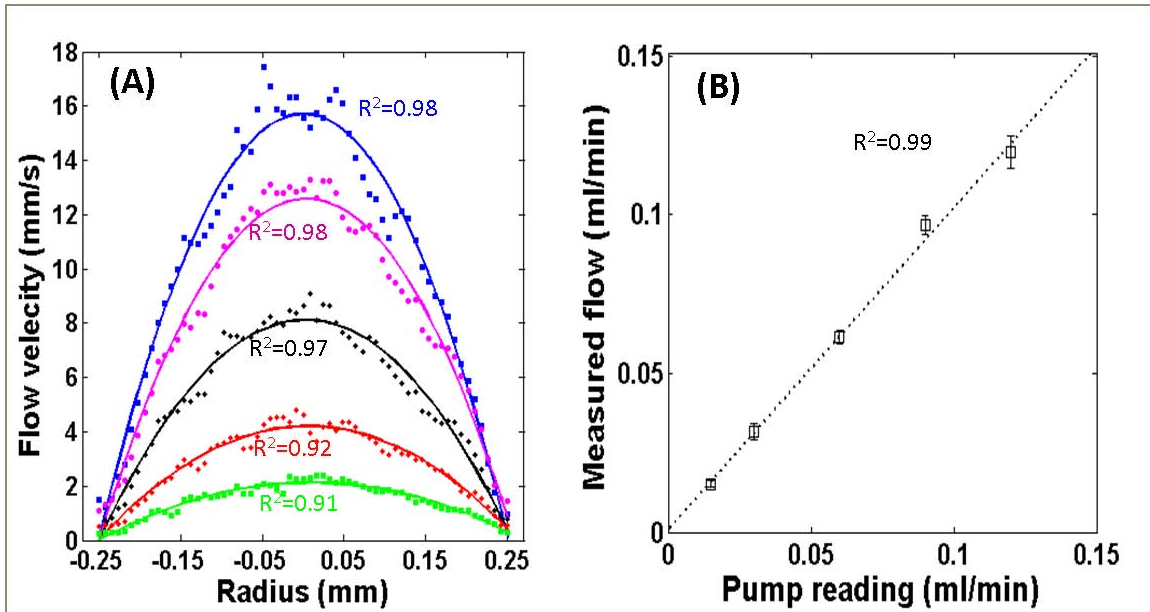
Figure 2.7 The correlation results between OMAG and pump readings. All OMAG values shown here were corrected by Doppler angle. In (A), the flow velocities on the midline obtained from OMAG are compared with the ideal parabolic profile at five different flow rates. (B) shows the high correlation between the flow rates calculated by OMAG and the real pump readings.

Firstly, we did in vitro validation on flow phantom because it is easy to control flow parameters in the simple structure. To fabricate a flow phantom to simulate a blood

vessel in the biological tissue, a glass capillary was imbedded in heterogeneous tissue, and then perfused by scattering solution at different known flow rates. We used OMAG to image it with a Doppler angle, and then calculated flow rate (Mean velocity × cross-sectional area) using OMAG velocity map. The correlation results between OMAG and pump readings are shown in **Fig. 2.7**. All OMAG values shown here were corrected by Doppler angle. In **fig. 2.7 (A)**, the flow velocities on the midline obtained from OMAG were compared with the ideal parabolic profile at five different flow rates. They are highly correlated. **Fig. 2.7 (B)** shows the high correlation between the flow rates calculated by OMAG and the real pump readings.

Then we did in vivo validation on normal mice. We compared perfusion rates obtained by OMAG with the gold standard values from autoradiography. In this study, we calculated regional blood perfusion rate in both methods at 12 representative spots shown in the OMAG projection view (**Fig. 2.8(A)**). We collected 36 individual values on three animals to do correlation analysis. **Figure 2.8 (A)** depicts the locations of regions selected for correlative studies using OMAG in vivo and IAP autoradiography post mortem. **Figure 2.8 (B)** is a scatter plot relating blood flow rates obtained by OMAG in vivo against postmortem measurements using IAP autoradiography. The correlation between OMAG and IAP was ~0.79. They are correlated but with some acceptable error. This is because the volumetric region used for quantification in two methods is not exactly same. Then, we averaged the six values over each hemisphere, and found their correlation is increased. **Figure 2.8 (C)** shows plot of the averaged regional CBF (rCBF) over the hemispheres for each mouse obtained from OMAG in vivo and IAP post-mortem. The correlation between OMAG and IAP was ~0.96. Although the result is promising, in the future work we need increase the number of animal to do statistics for further validation.
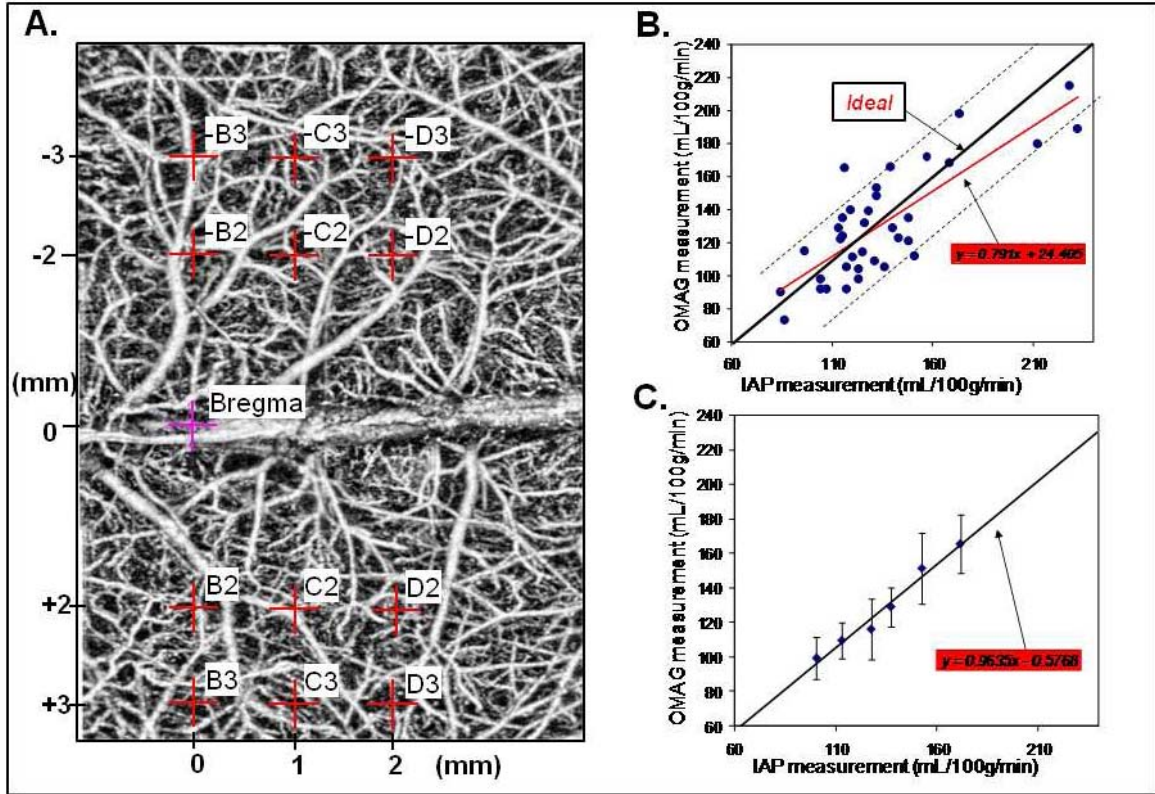
Figure 2.8 Correlation of in-vivo measurements of cortical perfusion using OMAG and post-mortem blood flow rates using IAP autoradiography [79]. (A).Coordinates used to match areas sampled in vivo using OMAG with corresponding areas on post mortem brain slices. The 12 regions of were located 2 and 3 mm lateral and 0, 1 and 2 mm posterior to Bregma on both sides. C. Summary table from showing close blood flow rate values obtained in 12 ROI from 2 mice using OMAG and IAP autoradiography. (B). Scatter plot of blood flow rates obtained from OMAG in vivo against IAP postmortem. The correlation coefficient was 0.8. The slight difference between the two measurements may be due to: 1) errors in accurately localizing the volumes used for quantification, 2) errors in calculating Doppler angles from 3D OMAG flow image, and 3) the minimal resolvable blood flow velocity of ~200μm/s in OMAG. (C). Plot of averaged rCBF over the hemispheres for each mouse obtained from OMAG in vivo and IAP post-mortem. The correlation between OMAG and IAP was ~0.96.

2.3 Objectives of my study

Since OMAG has high spatial resolution and velocity sensitivity over other imaging modalities, **the primary objective** of this work is to demonstrate the utility of OMAG system to visualize the 3D micro-circulatory vessel network within the tissue beds. The imaging targets involved in this work are both the cerebral tissues and the peripheral tissues.

The direct motivation of this research is to accelerate the usage of OMAG in basic scientific research for better understanding the basic mechanisms involved in vascular diseases. Accordingly, **the secondary objective** of this work is to evaluate the capability of OMAG for in vivo chronic imaging vessel morphology and quantifying blood flow changes in mouse under diverse pathologic conditions. Correspondingly, we aim to:

1. Establish the animal models for this work which closely mimics cerebral physiology and peripheral physiology observed in humans, which will help our imaging studies toward understanding fundamental aspects of human physiology as well as toward the development of clinical diagnostic instrumentation.

2. Assess the utility of OMAG on imaging and quantifying of blood perfusion within microcirculatory tissue beds in vivo; and compare the in vivo results obtained by OMAG with those from invasive gold standard methods in animal models.

3. Assess the feasibility of OMAG for differentiating the vascular responses between vehicle and treated animals in order to facilitate the application of OMAG on identifying therapeutic effects.

The major contributions include the establishment of experimental base or guide for the application of OMAG in the explored animal models and corresponding biological tissues, the discovery of the characteristics of vascular development in animal models studied and the effects of agents which promote tissue perfusion restoration.

Chapter 3

Assessment of Optical Micro-AngioGraphy in Cerebral Blood Flow

Functional changes in CBF are tightly coupled with neural activity, closely associated with brain tissue requirements, and tightly linked with brain tissue remodeling in pathological processes [80]. In an effort to better understand brain activity and response to internal or external stimulus [81], and cerebrovascular diseaseses, the detailed information on cerebal microvasculature is a requirement. However, microscopic methods cannot provide their highest resolution without compromise of the integrity of the cranium, whereas in vivo methods cannot give images of 3D vasculature down to microcirculatory tissue beds [82]. Further, very few methods can simultaneously provide multiple perfusion parameters, such as vessel morphology, blood velocity, blood volume, blood flow rate or perfusion rate, etc. The newly developed method, OMAG is proposed to be a non-invasive and quantitative method to image depth-resolved cerebral blood flow, especially the microcirculatory network. By collaborating with other groups, the relationship between CBF and neural activity is being studied by OMAG in whisker and electrical stimulation animal models. In this Chapter, the assessment of OMAG was performed in three pathological animal models respectively described in three sections. Focal traumatic brain injury model is an easy-handling model to obtain restored microcirculation for testing OMAG performance and optimizing its configuration. Focal ischemic brain injury model is an extensively-used model which demonstrates a typical hemodynamic process for detection of in vivo imaging system. The third model, meningeal thrombosis model was used to test the flow sensitivity of OMAG and to see if OMAG can document the meningeal blood circulation which may be responsible for the cause of some pathological conditions, such as migraine.

3.1 In vivo optical imaging of revascularization after brain trauma[1]

Brain trauma is a leading cause of death and long-term cognitive and behavioral dysfunction in children and young adults, yet effective treatments are lacking, in part because critical aspects of post-traumatic repair are not understood. Vascular imaging methods play a critical role to address the reconstruction of damaged tissue perfusion which is essential to brain tissue repair after trauma. In this section, penetrating brain injury model as a representative brain injury model was employed to assess new vascular imaging technique, OMAG. The microvasculature emerging during recovery process demonstrates the high resolution of OMAG, and the difference of restored blood volume between normal and transgenic mice exhibits the quantitative property of OMAG.

3.1.1 Abstract

Revascularization following brain trauma is crucial to the repair process. We used OMAG to study endogenous revascularization in living mice following brain injury. OMAG is a volumetric optical imaging method capable of *in vivo* mapping of localized blood perfusion within the scanned tissue beds down to capillary level imaging resolution. We demonstrated that OMAG can differentiate revascularization progression between traumatized mice with and without soluble epoxide hydrolase (sEH) gene deletion. A quantitative time course of revascularization was determined from serial imaging of the traumatic region in the same mice over a one-month period of rehabilitation. Restoration of blood volume at the lesion site was more pronounced in sEH knockout mice than in wild-type mice as determined by OMAG. These OMAG measurements were confirmed by histology and showed that the sEH knockout effect may be involved in enhancing revascularization and may thus contribute to an effective

---

treatment strategy for brain trauma. The correlation of OMAG with histology also suggests that OMAG is a useful imaging tool for real-time *in vivo* monitoring of post-traumatic revascularization and for evaluating agents that inhibit or promote endogenous revascularization during the recovery process.

3.1.2 Background

Revascularization is an endogenous process or a surgical procedure for the provision of new, additional or augmented blood supply in order to restore the impaired circulation of affected organ [83]. It is also in conjunction with other medical terms such as neovascularization (new vessel formation) [84], vascular remodeling (structural rearrangement) [85] and vascular reperfusion (reopening of occluded vessels) [86] to denote specific forms of revascularization.

Endogenous revascularization occurs in a wide range of pathologic processes. Following an ischemic event, the injured tissue is dependent on peripheral blood perfusion; and revascularization can play a pivotal role in the design of therapeutic strategies against ischemic injury [87, 88]. Following penetrating brain trauma, when the layers of the meninges are breached and the brain parenchyma is disrupted by mechanical damage, ultra-structural studies indicate that neovascularization occurs in the traumatized brain of adult rats [89, 90]. Previous studies also suggest that therapeutic revascularization after therapeutic treatment may repair damaged and leaky vessels, ameliorate vascular insufficiency, and replenish ischemic tissue during inflammation [26]. Revascularization may also provide direct beneficial effects on axonal remodeling or neural integrity, indicating a new paradigm for treating neural disorders caused by traumatic brain injury [26].

To design an effective treatment, we must have a better understanding of vascular restoration under traumatic neurological conditions. However, no means are currently available that can visualize and quantify the dynamic process of revascularization in the course of post-traumatic rehabilitation. Thus, assessing therapeutic potential based on vascular modulation in brain injury models is difficult, if not impossible. In this regard, methods are required that can provide precise identification and quantification of

revascularization and monitor the effects of promising agents on augmenting vascular activity in preclinical studies.

Vascular imaging is indispensable for studying trauma-related revascularization and for evaluating the potential of novel modulators to restore microvascular activity. Currently, microscopic methods – ranging from fluorescence, confocal, and multiphoton microscopy to electron microscopic imaging – are often used to elucidate the structure of blood vessels. Magnetic resonance imaging, positron emission tomography, ultrasonography, and optical imaging provide non-invasive, functionally relevant images of angiogenesis in animals and humans. An ongoing dilemma, however, is that microscopic methods provide their highest resolution on preserved tissue specimens, whereas *in vivo* methods give images of living tissues deep within the body but at much lower resolution and specificity and generally cannot resolve vessels of the microcirculation [82].

To circumvent limitations of non-invasive imaging of endogenous revascularization in small animal models of brain injury, we used high-resolution OMAG [63] to observe the process of revascularization in traumatized mice *in vivo*. OMAG is a recently developed novel imaging technique capable of producing 3D images of dynamic blood perfusion within microcirculatory tissue beds at an imaging depth up to ~2 mm below the surface. As a variation of optical coherence tomography technology [58, 60], OMAG produces imaging contrasts via endogenous light scattering from moving particles (eg, flowing blood cells within open vessels); thus, no exogenous contrast agents are necessary. The basic physics behind this type of imaging is the well-known Doppler effect. The light backscattered from moving particles has a beating frequency that can be used to distinguish scattering signals by moving elements from those by static elements. Briefly, OMAG mathematically maps the backscattered optical signals from moving particles into one image – the blood flow image – while it *simultaneously* maps the backscattered optical signals from static particles into a second image – the microstructural image. In this study, we demonstrated that the imaging resolution of OMAG is sufficient to visualize lesion-induced cerebral endogenous revascularization.

Because new functional vasculature (with flowing red blood cells) growing in damaged tissue could be detected and quantified, we demonstrated the potential of OMAG to study the therapeutic regulation of revascularization in the mouse brain after trauma.

P450 eicosanoid epoxyeicosatrienoic acids (EETs), which are derived from arachidonic acid, are endogenous bioactive lipid mediators that play important roles in vasodilation [91], promotion of angiogenesis [92], and many pathophysiological processes. The beneficial effect of EETs, however, is limited by their metabolism via sEH [93, 94]. Targeted deletion of sEH, therefore, inhibits EETs breakdown, causing intracellular accumulation and increased levels of EETs in brain. Previous studies showed that sEH pharmacological inhibitors can significantly protect brain from ischemic injury through a vascular mechanism linked to the reduced hydration of EETs [95]. Here, for the first time, we used OMAG to investigate endogenous revascularization for up to four weeks after penetrating brain trauma in live mice with and without sEH gene deletion. Our data demonstrated that sEH gene deletion promotes revascularization earlier and more rapidly in genetically engineered mice than in their wild-type counterparts.

3.1.3 Materials and Methods

All experimental animal procedures performed in this study conform to the guidelines of the US National Institutes of Health. The laboratory animal protocol was approved by the Animal Care and Use Committee of Oregon Health & Science University (Portland, OR, USA)

3.1.3.1 Animal model and experimental protocol

Three-month-old C57BL/6 male mice weighing 20-30g without (wild type, WT) (n=5) and with targeted deletion of sEH (sEH knockout, sEHKO) (n=5) were subjected to penetrating brain trauma by inducing a traumatic lesion in the cortex through the cranium. A 21-gauge needle was disinfected, mounted on a stereotaxic device (Stoelting Co., IL), and used to puncture a round vertical hole at a point 1.0 mm caudal to bregma, 2.0 mm lateral from the midline suture through the skull, schematically shown in **Fig. 3.1A**. Brain tissue damage induced by needle insertion is shown in a typical histological

section crossing the center of the injury site (**Fig. 3.1B**). The injury depth is ~1.5mm measured from the surface of the parenchyma. All mice were euthanized four weeks after brain trauma.
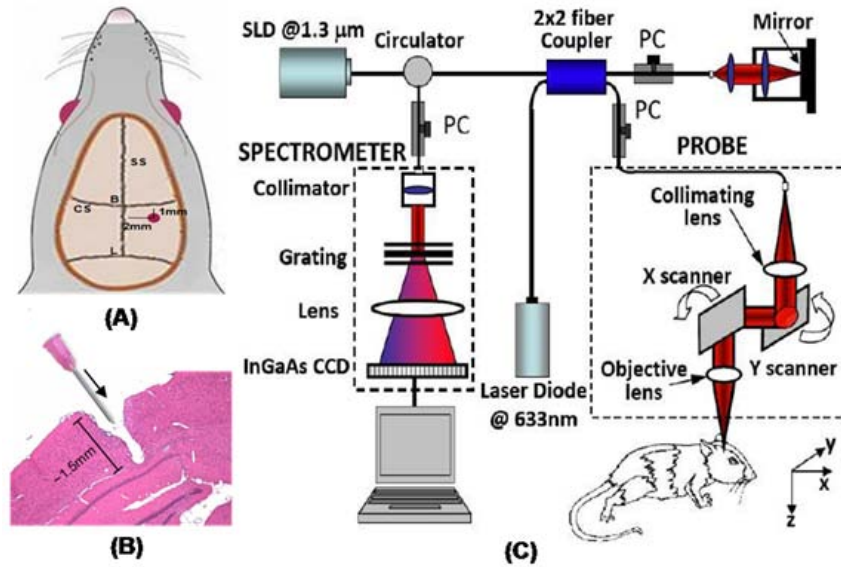
Figure 3.1 OMAG system and imaging protocol. (A) shows the mouse skin window created for OMAG imaging, where a penetrating brain trauma (shown by a pink dot) was introduced at a region 1.0mm caudal to bregma and 2,0mm lateral from the sagittal suture through the skull. SS, sagittal suture; CS, coronal suture; B, bregma; L, lambda. In (B), brain tissue damage is shown by a typical histological section across the center of the injury site. The injury depth is around 1.5mm measured from the surface of the parenchyma. (C) is the schematic of the OMAG system used to collect the 3D micro-angiography of traumatic brain tissue in small animal model in vivo. CCD represents the charge coupled device, PC the polarization controller.

3.1.3.2 OMAG in vivo imaging

OMAG measurements were performed using the system illustrated in **Fig. 3.1C**, similar to the one previously described [96]. Briefly, a broadband infrared SLD with a central wavelength of 1310 nm and a spectral bandwidth of 56 nm served as the light source. The light from the SLD was coupled into a fiber-based Michelson interferometer and subsequently delivered onto a stationary mirror (the reference arm) and focused into the brain tissue via an objective lens (the sample arm). The light backscattered from the sample and reflected from the reference mirror were recombined and then recorded by a home-built high-speed spectrometer that employed a line scan infrared InGaAs array

detector. The system had an imaging resolution of 16 x 16 x 8 μm^3 at x-y-z imaging direction and an imaging depth of ~2 mm in brain tissue. The minimum detectable blood flow velocity of the system was ~160 µm/s. To achieve 3D imaging, a pair of X-Y galvo-scanners were used to raster-scan the focused beam across the tissue, with one scanner for the X-direction (lateral) scan over ~2.5 mm of the sample and the other for the Y-direction (elevational) scan also over ~2.5 mm of the sample. The imaging rate in this study was set at 20 frames (X-scan) per second. The data cube of each 3D image was composed of 500 discrete frames, which took ~25 seconds to acquire.

The animal head was shaved and depilated before OMAG imaging. During the imaging, the animal was immobilized on a custom-made stereotaxic stage and was lightly anesthetized with isoflurane (0.2 L/min O_2, 0.8 L/min air). The body temperature was kept at 35.5-36.5°C with a warming blanket and monitored by a rectal thermal probe throughout the experiment. An incision of ~1 cm was made along the sagittal suture, and the frontal parietal and interparietal bones were exposed by pulling the skin to the sides. The animal was then positioned under the OMAG scanning probe. In order to acquire the blood perfusion images over a large area of the cortex, the scan was performed clockwise, which resulted in six OMAG images covering the area between the anterior coronal suture and the posterior coronal suture. In this study, the total acquisition time for six images was ~8 minutes. A volume segmentation algorithm [96] was then applied to each OMAG image to isolate the blood flow signals within the cortex. After stitching the six images together and cropping them, the final OMAG image represented the cerebral blood perfusion over an area of ~4.2 x 7.2 mm^2 in the mouse cortex. If necessary, maximum amplitude projection was used to project the volumetric blood flow signals onto the X-Y plane to give a 2D view of blood vessel networks, ie, the projection image. Before inducing brain trauma, a control OMAG image was acquired as the baseline. After the trauma surgery, the animal was sutured, disinfected, and given antibiotics and then returned to the cage for rehabilitation. A series of OMAG images were taken at 30 minutes, 24 hours, and weekly up to 4 weeks after brain trauma for all animals.

3.1.3.3 Histological evaluation

After the last OMAG images were taken on day 30 after brain trauma, anesthetized mice were transcardially perfused with 0.9% saline for 2 minutes, followed by 4% ice-cold paraformaldehyde. The brains were removed together with the intact cranium and post-fixed in 4% paraformaldehyde at °C overnight. Blocks of 3 -mm-thick slices of brain tissue were then cut, decalcified in 10% formic acid, processed, and embedded in paraffin. Six- micron sections were cut on a sliding microtome (Leica 2155). After drying, the sections were deparaffinized and rehydrated through graded ethanol. Coronal sections were first stained with Hematoxylin and Eosin (H&E) to detect all types of vessels and then stained by CD34 immunohistochemical staining to identify the newly formed vessels around the wound site [97]. The primary antibody (rabbit anti-CD34, 1:2000) was bridged with a secondary goat anti-rabbit biotinylated antibody (Amersham) and avidin-biotin-peroxidase complex (Vectastain Elite kit, Burlingame, CA), and then visualized with 3, 3 -diaminobenzidine. Negative controls were performed by replacing the primary antibody with non-immune rabbit serum. Each coronal section stained by H&E or CD34 was digitized under a 10x or 40x objective (Nikon), and traumatic areas were identified and compared to the homologous areas in the contralateral side.

3.1.3.4 Data and statistical analysis

The extent of endogenous revascularization or recovered blood supply in the trauma zone was evaluated based on the total volume of blood flow in injured tissue that was identified from the OMAG 3D flow data for each animal. OMAG observations are expressed as mean values with standard deviation (S.D.). Two-way mixed-model analysis of variation (ANOVA) was performed on the mean blood volume at injury site between WT and sEHKO groups and between different time points to determine whether there is any statistical difference ($p<0.05$). Depending on the variances of the data, post-hoc test (Tukey) was conducted to determine where the differences were.

3.1.4 Results

OMAG imaging results provide evidence of revascularization after trauma in both WT

and sEHKO mice. Two sets of the projection images of cerebrovascular perfusion from representative WT and sEHKO animals are shown in **Fig. 3.2**. Because revascularization can now be assessed without sacrificing the animal, it is possible to determine a time course for individual animals. **Figure 3.2** shows sequential intravital images of revascularization during rehabilitation following trauma in a single WT (**Fig. 3.2A**) and sEHKO (**Fig. 3.2B**) mouse. Before revascularization, the blood flow is totally absent as shown by the black hole in **Figs. 3.2A1, A2, B1, and B2**, ie, OMAG detected no blood flow signal. This is due to damage to the vessel walls and hemostasis after bleeding at the trauma site. New blood flow signals within the trauma region indicate the formation of new functional vessels. In the WT mouse, this revascularization process first appeared by week 2 and continued to increase until week 3; whereas in the sEHKO mouse, new blood flow signals were clearly visible by week 1 and continued to increase and connect with established vasculature at least until week 4 after trauma. It should be noted that some veins proximal to the injury site were activated after trauma in both WT and sEHKO mice, expressed by the increased flow intensity and vessel diameter in OMAG images. Their functions were probably related to draining excessive fluid caused by post-traumatic edema and promoting the growth of new microvessels in the avascular area. In the WT mouse, a draining vein only responded to the injury at day 1 (green arrow in **Fig. 3.2 A2**). However, in the sEHKO mouse, one branch of a draining vein was immediately promoted at 30 minutes after trauma (yellow arrow in **Fig. 3.2 B1**), and its elevated function was later taken over by another branch of the same draining vein (green arrow in **Fig. 3.2 B2**) from week 1 to week 4, probably due to its position priority.

The cross-sectional OMAG maps in **Fig. 3.3** detect the precise location of revascularization and exhibit typical evolution patterns of revascularization for the same WT and sEHKO mice imaged in **Fig. 3.2**. In the representative WT mouse, the cortical vessels were destroyed by the penetrating injury; and early revascularization occurred on the scanned layer of the brain cortex at week 2. The remodeled vessels were present and extruded into the wound site from week 2 to week 3 and then stopped and regressed by week 4 after trauma. In the representative SEHKO mouse, initial revascularization occurred on the left side of the trauma site before week 1. The vessel density was

elevated rapidly and peaked at week 4, nearly filling the whole lesion.
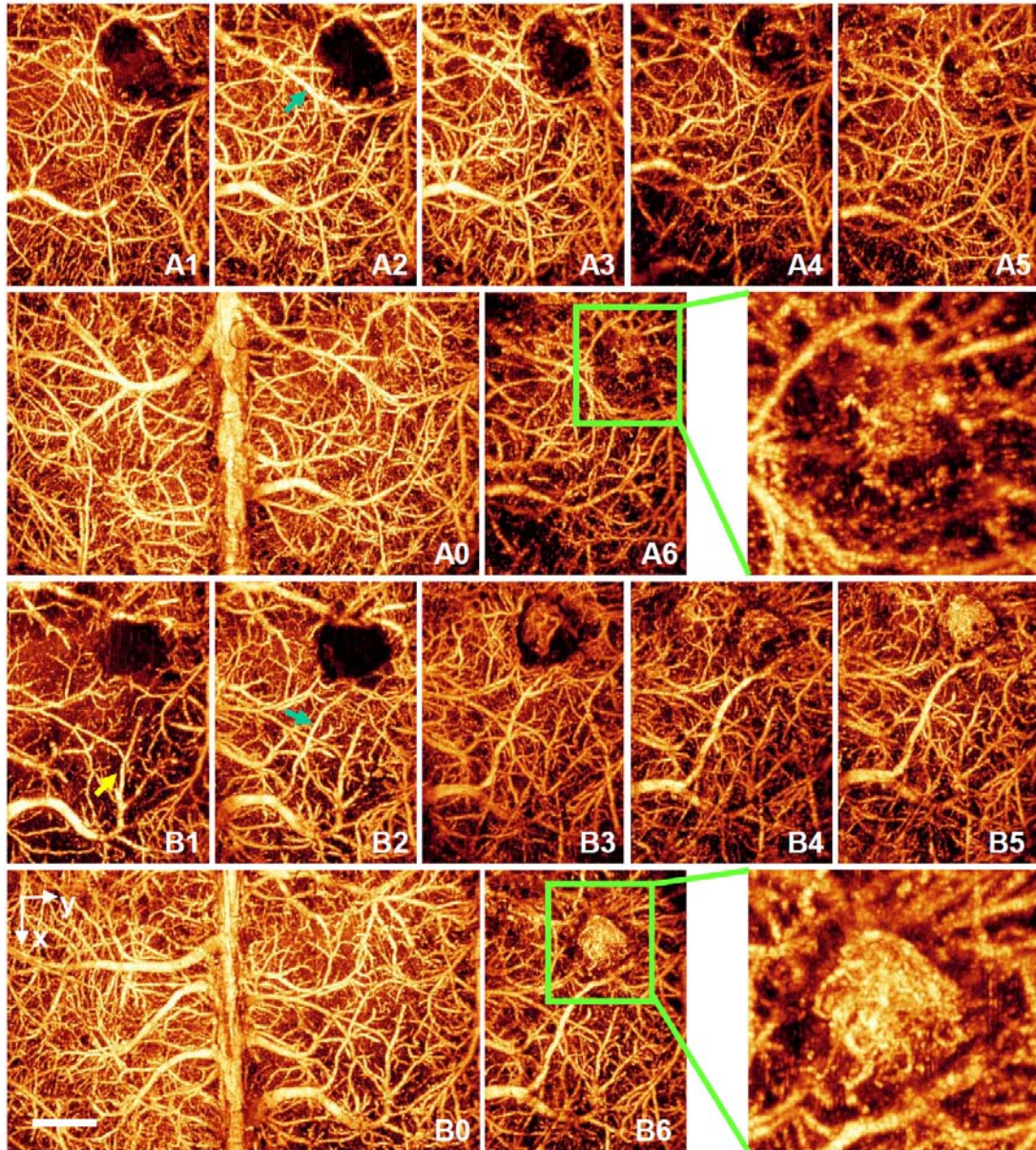
Figure 3.2 In representative WT (A) and sEHKO (B) mice, OMAG projection images of cerebro-vascular perfusion tracked revascularization at injured regions (green boxes) during trauma rehabilitation (A0&B0, baseline; A1&B1, 30 minutes; A2&B2, day 1; A3-A6&B3-B6, week 1- week4). All images except baseline only show ipsilateral sides. For this WT mouse, revascularization first appeared by week 2, and kept growing until week 3; a draining vein (green arrow in A2) responded only at day 1. For this sEHKO mouse, the recovered blood supply was visible by week 1, and continued to increase at least until week 4; a draining vein (yellow arrow in B1) responding to

traumatic environment was substituted by another branch (green arrow in B2). The white bar is 1 mm.
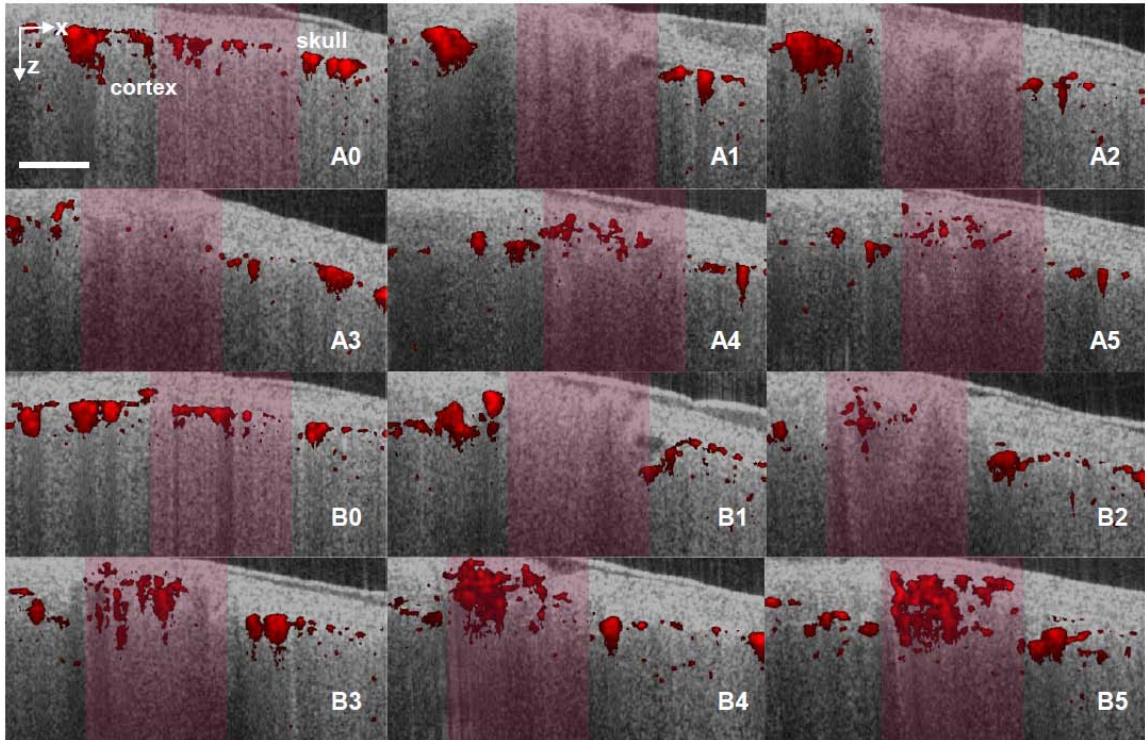
Figure 3.3 In representative WT (A) and sEHKO (B) mice, the cross-sectional (x-z) OMAG flow images (red color) fused with OMAG structure images (grey color) detect the precise location of revascularization in trauma zone (pink shadow). Newly formed blood flow migrated into the lesion and nearly filled the wound site in the process of recovery (A0&B0, baseline; A1&B1, day 1; A2-A5&B2-B5, week 1- week4) which is more apparent in sEHKO mouse. These OMAG fused maps also exhibit typical evolution patterns of restored circulation that has described in Fig. 2. The white bar is 500µm.

OMAG maps in both **Fig. 3.2** and **Fig. 3.3** comprise the cross-sectional optical images of revascularization development with semi-quantification of the time course of vascular morphogenesis in WT and sEHKO mouse brains. Supportive 3D data from the same representative WT and sEHKO mice are shown in **Fig. 3.4** and exhibit significant differences in new established circulation (green) between WT and sEHKO at week 4 after trauma.
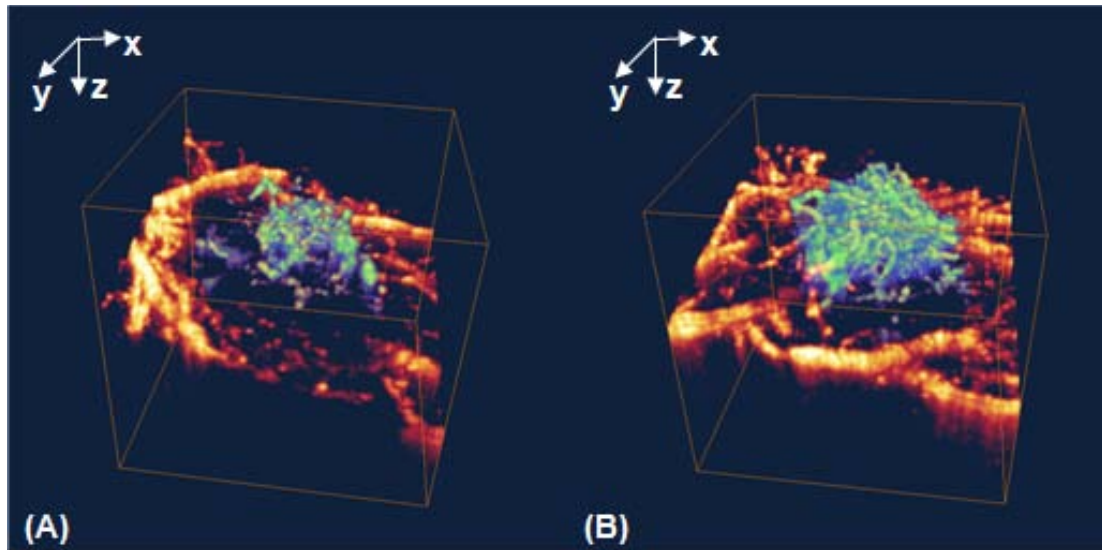
Figure 3.4 3D OMAG images (2.2x2.2x2.2mm) at week 4 (the last imaging point) show revascularization (green color) situated in the wound site and surrounded by the undamaged functional vessels (yellow color) in representative WT (A) and sEHKO (B) mice. Restored microvessels are clearly seen in both types of mice, but more revascularization is present in the sEHKO mouse.
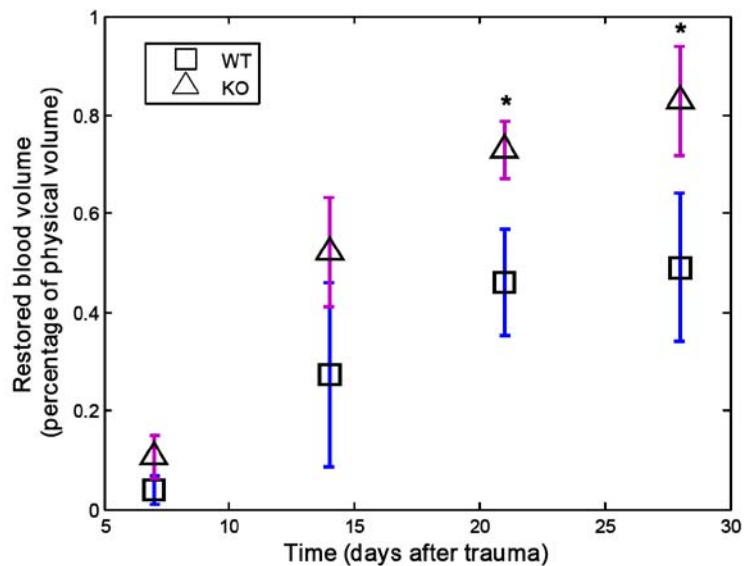
Figure 3.5 The time course and quantification of restored blood volume (mean ± s.d.) are determined by the OMAG method and are compared between WT and sEHKO mice. The data is obtained from five pairs of animals. Statistically, revascularization was significantly enhanced by sEH gene deletion in the traumatized mice with the greatest differences occurring between weeks 3 and 4 ($p < 0.03$).
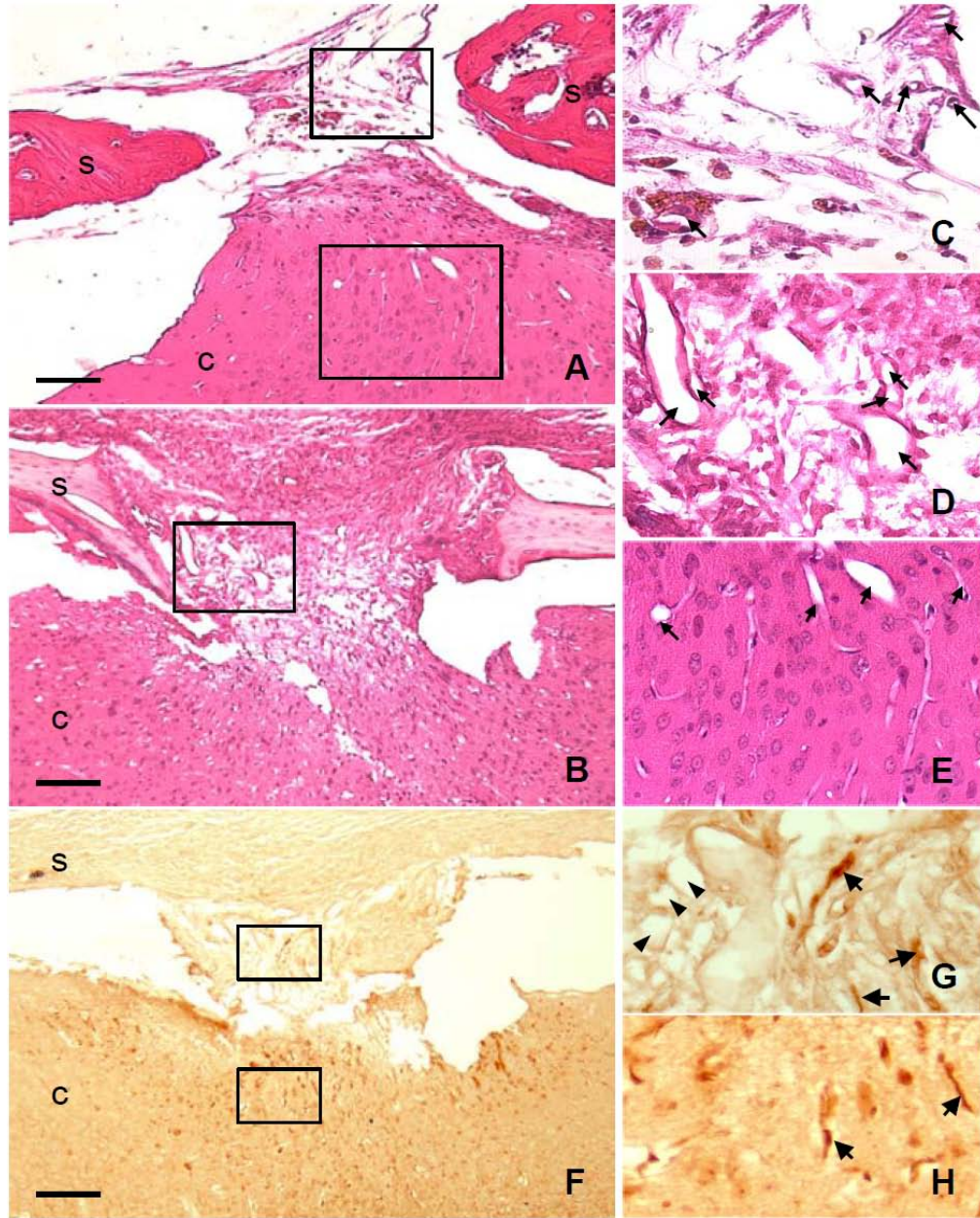
Figure 3.6 H&E staining shows revascularization after brain injury at week 4 for representative WT (A) and sEHKO (B) mice, indicated by arrows in the zoomed images (C) and (D), which correspond to the boxes between skull (s) and cortex (c) in (A) and (B) under 10x magnification. CD34 immunoreactive images from sEHKO mice are used to detect neovascularization, denoted by arrows in the enlarged images of the extracortical (G) and cortical (H) sites, which correspond to the boxes in (F) under 10x magnification. The CD34 immuno-negative vessels, denoted by arrow heads in (G), indicate that vascular remodeling or reperfusion is also involved in trauma-induced revascularization, which was also detected by OMAG. The black bar in (A), (B), and (F) is 500 µm.

The well-resolved, high contrast 3D OMAG images afforded by light scattering from moving elements in the newly formed blood vessels also allow quantitative measurements of revascularization *in vivo* (**Fig. 3.5**). The number of voxels in the same chosen volume at the trauma site from each animal was calculated and reported as the blood volume due to revascularization. The mean value with the SD among the animals examined was then determined. Within 4 weeks after trauma, the restored circulation detected by OMAG imaging in sEHKO animals increased markedly and reached a maximum at week 4. In contrast, the blood volume due to revascularization in WT animals increased gradually and peaked at week 3 after trauma. **Figure 3.5** shows that this parameter is significantly different between the sEHKO and WT groups from week 3 to week 4 after injury (P<0.03). Thus, by using OMAG, revascularization post trauma can be quantified without sacrificing the animal.

OMAG data for detecting revascularization in this study were confirmed by histological evaluation 4 weeks after trauma using H&E staining, as shown in **Fig. 3.6 (A-E)**. H&E-stained slices (10x) crossing the center of the trauma site from both WT mice (**Fig. 3.6A**) and sEHKO mice (**Fig. 3.6B**) demonstrate revascularization, denoted by arrows in the enlarged images (**Figs. 3.6C and 3.6D**) where vessels are highly intertwined with fibrous tissue. The comparison between **Figs. 3.6C and 3.6D** also demonstrates that revascularization is enhanced by sEH gene deletion, which is consistent with OMAG results. CD34 immunohistochemical staining was used to differentiate neovascularization from vascular remodeling or vascular reperfusion. The monoclonal antibody against CD34 reacts with endothelium of arteries and venules, and has been found to stain more intensely capillary endothelim [97]. It has been used for the diagnosis of vascular tumors and detection of small vessel proliferation representing neovascularization [98, 99]. In this study, the CD34 staining results from sEHKO mice showed that the vessels localized at the injury site are partially sensitive to CD34 staining, ie, newly formed vessels (denoted by arrows in **Fig. 3.6G**) are intensely stained while remodeled or reperfused vessels (denoted by arrow heads in **Fig. 3.6G**) are immune-negatively expressed. In addition, at the parenchymal defects (**Fig. 3.6H**), CD34 is densely expressed on new microvessels (denoted by arrows), which are also visualized

by H&E staining in Fig. 6E. It should be noted that histological studies show the cortical lesion induced by needle was healed and integrated into the healthy unaffected brain tissue after four-week recovery and repaired tissue with newly appearing vasculature further extruded into the extracortical lesion, suggesting such vascular neoformation detected by OMAG either within or above cortical defects are partially originating from the new vessels growing inside the cortex.

3.1.5 Discussion

Because OMAG permits serial monitoring of microcirculation on the same experimental animal over time, it may be particularly useful for *in vivo* evaluation of evolutional revascularization observed following brain trauma. Furthermore, OMAG may prove useful in evaluating the effectiveness of therapeutic interventions on revascularization. In our study, by showing the temporal profiles of cerebral blood perfusion at the injury site, the evolution of revascularization could be differentiated between WT and treated mice; and by providing the quantitative information on the evolution of revascularization, the effects of treatment could be further analyzed.

OMAG is a new optical angiography technology that provides markedly improved resolution over the previous *in vivo* vascular imaging systems. For example, the optical methods, laser speckle imaging and scanning laser Doppler imaging [100], have recently been reported to map cerebral vascular structure in small animals, but are of limited use in delineating microvascularization. In practice, the lower limit of flow imaging of OMAG is determined by the optical heterogeneous properties of the sample. For detecting the microvascular flow that has lower velocity, the OMAG imaging speed may need to be reduced in order to increase the dwell time of the probe beam on the slow flows, which would inevitably increase the imaging time required to obtain the necessary blood flow images. Nevertheless, our studies demonstrated that the current OMAG system has sufficient resolution to distinguish revascularization in the brains of mice that were sedated and restrained during imaging. Thus, assessment of the restored blood flow and, presumably, the patterns of both non-capillary and capillary flow in real time are possible without sacrificing the animal, as would be required in other types of structural

imaging studies. Comparing OMAG images between WT (**Fig. 3.2A**) and sEHKO (**Fig. 3.2B**) animals, revascularization began to mature in 1 week after trauma in treated animals and was accelerated compared to WT mice, in which revascularization began in week 2 after trauma. These data indicate that the sEH knockout mice evoke early and rapid revascularization in response to traumatic brain injury.

Furthermore, OMAG is capable of resolving both the cortical structures and blood perfusion at depths of ~2 mm through the intact cranium, a penetration depth that cannot be achieved with confocal microscopy. The localized signals from flowing blood may be combined with signals from static structures to capture a complete view of the orientation of blood vessels within the tissue. Thus, we expect that the OMAG technology will be useful not only in providing serial revascularization images, but also in localizing the sites of revascularization in living animals. In this work, 2D OMAG flow images fused with structure images (**Fig. 3.3**) clearly identified the dynamic position of endogenous revascularization in two types of traumatized animals over a one-month period of rehabilitation. 3D OMAG flow images around the wound site at week 4 (**Fig. 3.4**) compared the recovered functional vasculature in detail between WT and sEHKO mice, as confirmed by H&E histological evaluation (**Fig. 3.4**). From the histology studies, we are convinced by CD34 immunoreactive images in both extracortical and cortical defects that new endothelial cells were recruited to form new functional blood vessels after brain injury. We note, then, that the restored cerebral perfusion imaged by OMAG can be attributed to new vessel growth as well as to remodeling of undamaged vessels or reperfusion of blocked vessels.

In addition to *in vivo* volumetric imaging of revascularization after trauma, OMAG can be used to quantify the restored blood flow volume by measuring the number of signals from flowing particles, ie, red blood cells in newly formed vessels. In our study, these quantitative values distinguished the time course of revascularization between WT and sEHKO animals (**Fig. 3.5**). The results indicated that revascularization in mice with sEH gene deletion accelerated from week 1 to week 4 after trauma, while revascularization in WT mice was observed at week 2 and slowly developed until week 3

after trauma. The coupling between revascularization and neurogenesis has been demonstrated by previous studies [101-103]. Furthermore, revascularization after trauma may alleviate neuronal damage by improving local blood flow and metabolite delivery to the nutrient-deprived neurons [89]. However, whether the noted accelerated revascularization and the extended time window of revascularization in mice with sEH gene deletion aides axonal remodeling or neural integrity deserves further investigation.

In addition, as a non-invasive imaging method, OMAG allows visualization of the dynamic fluctuation in global or localized blood perfusion as well as accurate localization of individual vascular activities that are likely related to pathological revascularization as a consequence of trauma. The serial imaging of our two groups of animals revealed that the enhanced revascularization response in sEHKO mice may relate to vascular regulation from a proximal draining vein that may be associated with proper disposal within the revascularization environment. For the WT animals, no apparent draining vein connected to the trauma region was found after day 1, despite a tendency toward recovery of vascular function; and revascularization remained more depressed in WT after week 3 compared with sEHKO mice, indicating that sEHKO mice have better potential for promoting revascularization. Somewhat surprisingly, the whole-head hemodynamic activity in animals with and without gene deletion dropped markedly at some time points, for example, during the emergence of revascularization (**Fig.3.2 A4, B3**). This vascular depression may be involved in regulating vascular plasticity during this early and vulnerable phase of revascularization. Unlike the draining vein, the fluctuation in cerebral blood perfusion is an unsteady phenomenon in the current animals examined. However, OMAG is undoubtedly a useful tool to investigate this phenomenon on revascularization following pathological conditions.

The current OMAG system is only sensitive to blood flow that is faster than ~160 µm/s, which is limited by the optical heterogamous property of the tissue as well as the detection unit in the system, i.e., the speed of the camera used. However, the flow velocity in capillaries ranges between 50 and 1000 µm/s [104], and is even slower under pathological conditions, such as the current study. Therefore, if the investigation focuses

on the initial event of revascularization following trauma, observation of the generation of precursor microvessels will possibly be inhibited, given that this beginning event has a flow velocity slower than 160 µm/s. Future studies, then, will focus on developing an ultra-high sensitive OMAG system based on CMOS (Complementary metal–oxide–semiconductor) detectors, so that capillary blood flows within injured tissue regions can be detected and imaged. The high speed afforded by a CMOS camera will not only increase the OMAG imaging speed, but will also facilitate the design of flexible optical beam scanning patterns. These will minimize the effect of the optical heterogeneous property of tissue on the minimal detectable flow velocity, so that the OMAG system will be sensitive to the precursor microvessels within injured tissue regions.

3.1.6 Conclusion

The present study demonstrated that OMAG is a useful imaging tool capable of serial imaging of cerebral endogenous revascularization after brain trauma in mice *in vivo*. Using OMAG, we have shown that the differences in revascularization between WT and sEHKO animals can be identified. In contrast to the WT mouse, revascularization detected by OMAG was significantly accelerated after trauma in the sEHKO mouse, indicating that sEH gene deletion protects the endogenous vasodilator EETs. Because of its capability to image blood perfusion with high resolution, OMAG may prove to be a practical tool for tracking revascularization and its vascular regulation following trauma. Without the necessity to sacrifice the animal, we anticipate that OMAG will enhance the use of rodent models to study novel anti-traumatic therapeutics and repair strategies that are designed to manipulate revascularization for brain injury and other brain disorders.

3.2 In vivo optical imaging of vascular response to cerebral ischemia and neovascularization

Stroke is the third leading cause of death in the United States, affecting more than 700,000 people annually, and may be ischemic or hemorrhagic in nature. Ischemic stroke

also called cerebral ischemia accounts for approximately 85% of all strokes. In this section, ischemic stroke model, the most popular cerebrovascular disease model, was used to indicate the functions of OMAG in imaging this type of acute brain dyscirculation event. This work shows different detections during intra- or post-ischemic period currently can be achieved by one imaging system, OMAG.

3.2.1 Abstract

In cerebral ischemic disease, hemodynamic response during intra-ischemic period and neovascularization in the post-ischemic period are two crucial ways to restore local blood supply and consequently protect neurological functions. In this paper, we used OMAG, a volumetric optical imaging method capable of in vivo mapping localized blood perfusion within the scanned tissue beds, down to capillary level imaging resolution, to study vascular perfusion response during occlusion and neovascularization following occlusion in living mice. We demonstrate that OMAG is capable of differentiating the residual blood flow during ischemia between ischemic mice with and without sEH gene deletion, which was confirmed by traditional method laser Doppler flowmetry (LDF). We also show that OMAG is feasible to dynamically distinguish the neovascularization at ischemic penumbra between ischemic mice with and without cytochrome P450-2C (CYP-2C) epoxygenase gene overexpression, which was also retested by immunohistochemistry. These OMAG measurements indicated that two types of transgenic effects may be involved in enhancing vasodilation and angiogenesis, respectively, which will contribute to the pharmacological benefits in the treatment of cerebral ischemia. The consistency of OMAG and conventional methods also suggest that OMAG has potentials to be utilized for in vivo tracking intra-ischemic vascular response and post-ischemic neovascularization and characterizing their pharmacological interventions during the progression and regression of brain ischemia.

3.2.2 Background

Cerebral ischemia, also called ischemic stroke, induced by the occlusion of one or more cerebral artery/arteries, dramatically decreases local cerebral blood flow and causes cell

death, brain atrophy, and functional deficit [105]. Previous studies suggested that preservation of surviving cells, tissue repair, and functional recovery largely depend on appropriate restoration of local blood supply. Studies from human and experimental stroke indicate that neovascularization is present in the adult brain after ischemic stroke [106, 107] and ischemic brain can be stimulated to amplify its intrinsic restorative processes to improve neurological function by cell-based or pharmacological-based therapies [25, 108]. Therefore, neovascularization has been an intriguing research area in the investigation of ischemic stroke. In recent years, there has been another considerable interest in the determination of cerebral hemodynamic response in ischemic injury, because it may be possible to protect ischemic cerebral tissue against an impending cerebral infarction by increasing cerebral blood flow through use of appropriate treatment [22].

Our current understanding of the ischemic cerebral vascular response during the intra-ischemic interval has been derived mainly from laser Doppler flowmetry (LDF) and autoradiography [109, 110]. However, LDF only provides the relative values obtained from the blood perfusion in the surface and autoradiography is a one-point measure [111]. The differential assessment of microvascular density during post-ischemic period is traditionally achieved by histology or immunohistochemistry [112], whereas these methods do not allow dynamical study in a given animal. MRI is the only imaging modality applied for repeatedly monitoring CBF regulation during intra-ischemic period and neovascularization during post-ischemic period [113], but its low resolution prohibits localizing and precisely describing the changes of microcirculation after stroke. Recent study has shown a novel and non-invasive three-dimensional optical imaging method, OMAG [63] can be used for in vivo monitoring and quantification of blood perfusion in the brain through an intact skull. In light of this, the vascular response to cerebral ischemia may be dynamically investigated using OMAG. Additionally, its resolution, down to capillary level, would make it also possible to monitor neovascularization after stroke. To our knowledge, few studies to date have provided evidence to show achieving these dual functions via one method.

The purpose of the present study was to apply this new technique for monitoring cerebral circulation during intra-ischemic period (short-term) and tracking neovascularization during post-ischemic period (long-term). To further test its ability to identify the effect of pharmacological therapies in the ischemic brain, we examined the protective effect during intra-ischemic period that is correlated with EETs which are well-known vasodilation agents [114, 115]. sEH is an important enzyme involved in the metabolism and terminal inactivation of EETs [114]. Recent studies have demonstrated that sEH knockout male mice were protected from ischemic brain injury compared to WT male mice due to the higher residual blood flow during ischemia [95, 116]. In our study, we employed our new method, OMAG, on both WT and sEHKO mice subjected to a well-defined middle cerebral artery occlusion (MCAO) model. By comparing with the results from LDF, we confirmed the reliability of OMAG and discussed its advantages over current measuring modalities. Besides promoting vasodilation, additionally, EETs has been shown to stimulate angiogenesis by the studies in vitro [117]. In our study, we not only demonstrated the capability of OMAG to in vivo monitor neovascularization during post-ischemic period, and but also tested the hypothesis that higher EETs production contributes to more neovascularization by overexpressing cellular CYP-2C epoxygenase which is a major enzyme in the synthesis of EETs. To achieve this goal, we used OMAG to investigate cerebral neovascularization up to 4 weeks after MCAO in mice with and without CYP-2C overexpression. By comparison with immunohistological study, our data demonstrated that OMAG can repeatedly characterize cerebral neovascularization and help to define if elevated expression of ETTs enhances new vessel growth.

3.2.3 Materials and Methods

All experimental animal procedures were performed in conformity with the guidelines of the US National Institutes of Health. The laboratory animal protocol for this work was approved by the Animal Care and Use Committee of Oregon Health and Science University (Portland, OR, USA).

3.2.3.1 Animals

Group 1: C57BL/6 male mice without (WT) (n=5) and with targeted deletion of sEH (sEHKO) (n=5) was used for the study of vascular response to cerebral ischemia.

Group 2: C57BL/6 male mice without (WT) (n=4) and with overexpression of CYP-2C (2C) (n=4) was used for the study of neovascularization in the post-ischemic period. All mice weigh 25 to 28g at ages of three months.

3.2.3.2 Middle cerebral artery occlusion in mice

All mice were subjected to transient focal cerebral ischemia by use of the intraluminal MCAO technique [116]. Briefly, mice were anesthetized with isoflurane (1.5-2%) and kept warm with water pads. A transcranial laser-Doppler probe was secured on the right temporal side of the head to verify vascular occlusion and reperfusion. A silicone-coated 6-0 nylon monofilament was advanced into the right internal carotid artery by passing external carotid artery until laser-Doppler signal dropped to less than 30% of baseline. After affixing the filament in place, the surgical site was closed. The animal was awakened and assessed at 2 hours of occlusion for neurological deficit. Mice with clear neurological deficit were re-anesthetized, laser-Doppler probe repositioned over the same site on the skull, and the occluding filament was withdrawn to allow reperfusion. Mice for long-term imaging were euthanized four weeks after brain ischemia.

3.2.3.3 OMAG in vivo imaging

OMAG measurements were performed using a system illustrated in **Fig.3.1C** , similar to the one described previously [96]. A broadband infrared SLD (Denselight, Singapore) with a central wavelength of 1310 nm and a spectral bandwidth of 56 nm was adopted as the light source. The light from SLD was coupled into a fiber-based Michelson interferometer and delivered onto a stationary mirror (the reference arm) and focused into the brain tissue via an objective lens (the sample arm). The light backscattered from the sample and reflected from the reference mirror were recombined and then recorded by a home built high-speed spectrometer that employed a line scan infrared InGaAs detector. The system has the imaging resolution of 16 x 16 x 8 µm3 at x-y-z imaging direction, and

an imaging depth of ~3 mm in brain tissue. To achieve 3D imaging, a pair of X-Y galvo-scanners were used to raster-scan the focused beam spot across the tissue, with one scanner for X-direction (lateral) scan over ~2.5 mm at the sample, and the other for Y-direction (elevational) scan of also ~2.5 mm. The imaging rate in this study was set at 20 frames (X-scan) per second. The data cube of each 3D image was composed of 500 discrete x-scans, which took ~25 s to acquire. The minimal flow velocity that can be detected by the system was ~260µm/s.

The animal head was shaved and depilated before OMAG imaging. During the imaging, the animal was immobilized in a custom made stereotaxic stage and was lightly anesthetized with isoflurane (1.5-2%) and kept warm with heating pads. An incision of ~1 cm was made along the sagittal suture, and the frontal parietal and interparietal bones were exposed by pulling the skin to the sides. The animal was then positioned under the OMAG scanning probe. In order to acquire the cerebral blood perfusion images over a large area of the cortex, the scan was performed clockwise that resulted in six OMAG images covering areas between anterior coronal suture (Bregma) and posterior coronal suture (Lambda). The total imaging acquisition time for six OMAG scans was ~8 minutes. For each 3D OMAG image, a volumetric segmentation algorithm [96] was applied to isolate the blood flow signals within the cortex, and a maximum projection method was then used to project the blood flow signals into X-Y plane in order to reduce the image size. The final image, representing the CBP over the mouse cortex, was obtained by stitching six resulted images together and cropping, covering an area of ~4.2 x 7.2 mm^2 over the mouse head. Before inducing MCAO, a control OMAG image was acquired as the baseline. Then the mouse was subjected to MCAO surgery. For group 1 animals, at 30 min after filament insertion, OMAG imaging was again initiated and laser-Doppler probe was left in position during OMAG imaging. Animal were euthanized when imaging was done. For group 2 animals, in 2-hour occlusion, the animal was sutured, disinfected and injected with antibiotics, and then returned to the cage for rehabilitation. For long-term assessment, a series of OMAG imaging were performed weekly up to 4 weeks after brain ischemia for all animals.

3.2.3.4 Histological immunohistochemistry

Group 2 mice were transcardially perfused with 0.9% saline for 2 min, followed by 4% ice-cold paraformaldehyde. The brains were removed and post fixed in 4% paraformaldehyde at 4ºC overnight, after which a total of 3-mm-thick blocks of brain tissue over infarct area were cut, processed , and embedded in paraffin. Six micron sections were cut on a sliding microtome (Leica 2155), and following drying, the sections were deparaffinized and rehydrated through graded ethanol. Coronal sections were firstly stained with von Willebrand factor (vWF) [118] to detect all types of vessels and describe vessel densities, and then stained by CD34 immunohistochemical staining [97] to localize the newly formed vessels around ischemic core area. The primary antibody (rabbit anti-vWF or rabbit anti-CD34 1:2000) was bridged with a secondary goat anti-rabbit biotinylated antibody (Amersham) and avidin-biotin-peroxidase complex (Vectastain Elite kit, Burlingame, CA), and then visualized with 3, 3′-diaminobenzidine. Negative controls were performed by replacing the primary antibody with non-immune rabbit serum. Each coronal section stained by vWF or CD34 was digitized under a 10x or 40x objective (Nikon). Ischemic cores were identified by fibrosis in combination with inflammatory cells, and neovascularization at ischemic penumbras are characterized by the positive expression of CD34, compared to the homologous areas in the contralateral side.

3.2.3.5 Data and statistical analysis

Image analysis of OMAG was performed with Matlab software. The extent of residual blood flow in the ischemic region was evaluated based on the volume of blood perfusion at ipsilateral side. In order to compare with LDF data, all OMAG blood volume value was normalized and represented by the percentage of the pre-interventional baseline (BVt, % baseline, where t=30 min, 1, 2, 3, 4 weeks). The vessel density values produced by OMAG are based on the volume of blood flow signals in a certain tissue volume unit. In this study, OMAG vessel density values at different weeks after stroke were normalized and represented by the ratio of that in ipsilateral side and that of homologous tissue in the contralateral side.

OMAG observations and LDF measurements are expressed as mean value with S.D.. The differences of OMAG and LDF between two groups were analyzed by t-test. All t-test were two-tailed. The significance level was set at 0.05.

3.2.4 Results

3.2.4.1 Vascular response to cerebral ischemia (short-term)

OMAG maps in **Figure 3.7A** detect the evidence of ischemia in the ipsilateral cerebral cortex compared to the contralateral cortex during MCAO in WT (**Fig. 3.7A3**) and sEHKO (**Fig. 3.7A2**) mice. Ischemic images were obtained at 30 min after onset of occlusion, and compared to pre-occlusion baseline. As there is no difference on baseline OMAG maps between WT and sEHKO mice, here we only used the baseline image from sEHKO mice. The suppression of cortical blood flow in ipsilateral cortex determined in terms of the percentage of the baseline (BVt, % baseline) was quantified and compared among groups. **Fig. 3.7B** demonstrates in deeply situated cortical regions that the suppression rates of blood flow in the ischemic cortex were higher in sEHKO mice compared to WT mice ($P<0.05$). We confirmed OMAG finding using Laser-Doppler perfusion (LDP) data in **Fig. 3.7C**. Similarly, LDP at time point of 30 min was higher in sEHKO mice compared to WT mice.

3.2.4.2 Neovascularization after stroke (long-term)

OMAG perfusion views in **Fig. 3.8A** show representative vasculature maps of 2C mice at various time points (baseline and week 4). Comparison of the network of blood vessels in ischemic cortex of 2C mice between baseline and week 4 after stroke (shown in white line box in **Fig. 3.8A** and magnified in **Fig. 3.8B**) illustrates the change of the profiles of dominant vessels and their branches which were supplying the ischemic area, and gives some evidence of neovascularizaiton during the post-ischemic periods (pointed by red arrows in **Fig. 3.8B**). For WT mice, whereas, no significant changes of vessel profile and vessel density caused by neovascularization are noted in ipsilateral side which is shown by **Fig. 3.8C**. **Figure 3.8D** shows the temporal features of vessel density in stroke mice with and without 2C over-expression. Compared with WT group, 2C group had relatively

higher density values at 1 to 4 weeks after stroke, but the differences were significant (P<0.05) during 2 to 4 weeks. By post-ischemia week 1, the functional vessels in 2C animals almost recovered to contralateral level. However, the functional vessel restoration wasn't seen in WT group until 3 weeks after stroke.
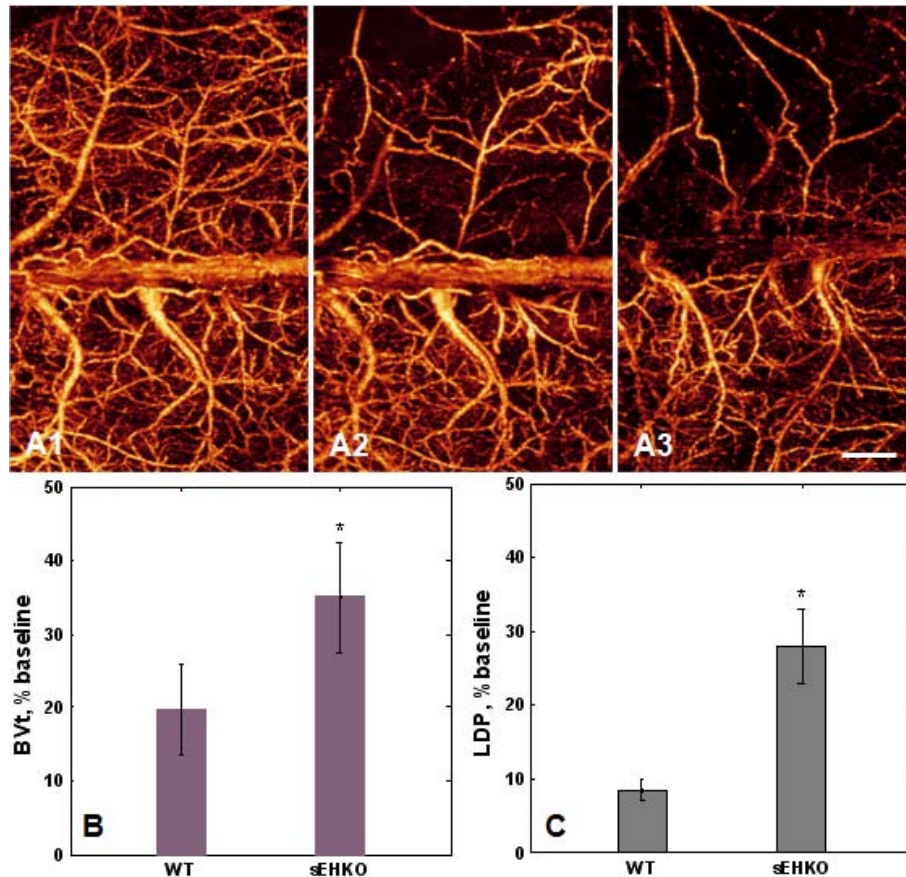
Figure 3.7 Vascular Response to cerebral ischemia identified and quantified by OMAG and compared with conventional results from LDF. (A) Cerebral blood perfusion obtained by OMAG (projection views) illustrates the drop of perfusion in ipsilateral cortex at 30 min after onset of occlusion in WT (A3) and sEHKO (A2) mice as compared with baseline image (A1). (B) Quantification of blood volume by OMAG in ipsilateral cerebral cortex at 30 min during MCAO. (C) LDP values to confirm the difference of vascular perfusion between two groups of mice visualized and quantified by OMAG. The white bar is 1mm.
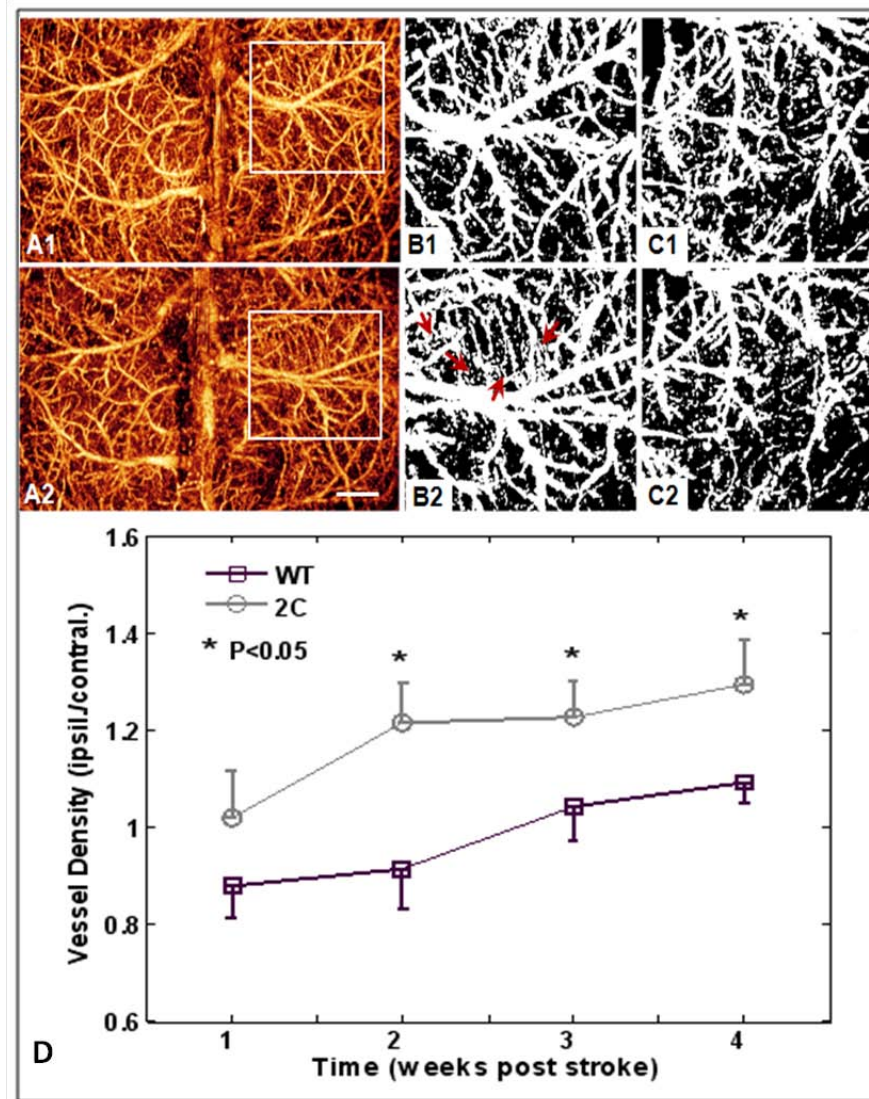
Figure 3.8 OMAG projection views illustrating neovascularization of WT and 2C mice at week 4 and their temporal profile along 4 weeks. Representative vasculature maps of 2C mice illustrate neovascularization at week 4 (A2) after ischemic stroke as compared with baseline (A1). (B1) & (B2) corresponding to the images in the boxes show the new microcirculation (indicated by red arrows) between vascular branches. The comparison on WT mice between baseline (C1) and week 4 (C2) shows no significant changes of vessel density at ipsilateral side. Dynamic vessel density measurements show 2C group had relatively higher values at 1 to 4 weeks after stroke, but the differences were significant (P<0.05) during 2 to 4 weeks. The white bar indicates 1mm.

To further demonstrate new blood flow signals captured by OMAG, cross-sectional images (x scan) locating in the ischemic penumbra extracted from 3D OMAG blood perfusion images are shown in **Fig. 3.9A**. For 2C mice, the cross-section in

ipsilateral side at week 4 (**Fig. 3.9A2**) clearly detects the new flow signals caused by neovascularization in cortex compared to baseline (**Fig. 3.9A1**). Whereas, vessel density at week 4 after ischemi (**Fig. 3.9A4**) was also increased in WT mice compared to baseline (**Fig. 3.9A3**), but the increase was not as significant as in 2C mice. The vascular density of corresponding homologous region in the contralateral hemisphere was also compared between baseline (**Fig. 3.9A5**) and week 4 (**Fig. 3.9A6**), but the difference between them is hard to be distinguished.

OMAG data for detecting newly formed vessels at penumbral areas after were confirmed by histological measurements at 4 weeks after ischemic stroke using vWF staining, as shown in **Figure 3.9B**. vWF stained slices (10 x) crossing the center of the infarct site from both WT mice (**Fig. 3.9B1**) and 2C mice (**Fig. 3.9B2**) demonstrate ischemic core and penumbra. Apparently, core area was filled with fibrosis tissue and inflammatory cells which are stained non-specifically by vWF antibody. Surrounding ischemic core, the vessels highly positively expressed by vWF are distributed in penumbra area. Specifically, the lumens of these vessels in 2C mice (**Fig. 3.9B4**) were enlarged (i.e., the vessel diameters were increased) compared with those in WT mice (**Fig. 3.9B5**). Because vessel densities in the homologous area of the contralateral hemisphere were not different between WT and 2C mice, in this figure (**Fig. 3.9**), only contralateral images from 2C mice are shown. Obviously, much less vessels expressed by vWF are present at contralateral side (**Fig. 3.9B3**). The comparison between enlarged images (**Fig. 3.9B4-B6**) corresponding to the images in the boxes in **Fig. 3.9B1-B3** also demonstrates vascular densities related to neovascularization at the boundary area of ischemic core were enhanced by CYP-2C overexpression. In order to further indicate new formed vessels are involved into the ipsilateral vessels with high density shown by OMAG optical method and vWF staining method, CD34 staining method was used to exclusively illustrate neovascularization. In this study, as we expected the newly formed vessels at ischemic boundary area were intensively expressed by CD34. Specifically, we found more new microvessels densely stained in 2C transgenic mice (**Fig. 3.9C1**) than those in WT mice (**Fig. 3.9C2**), and new vessels are barely recognized in the contralateral hemisphere (**Fig. 3.9C3**).
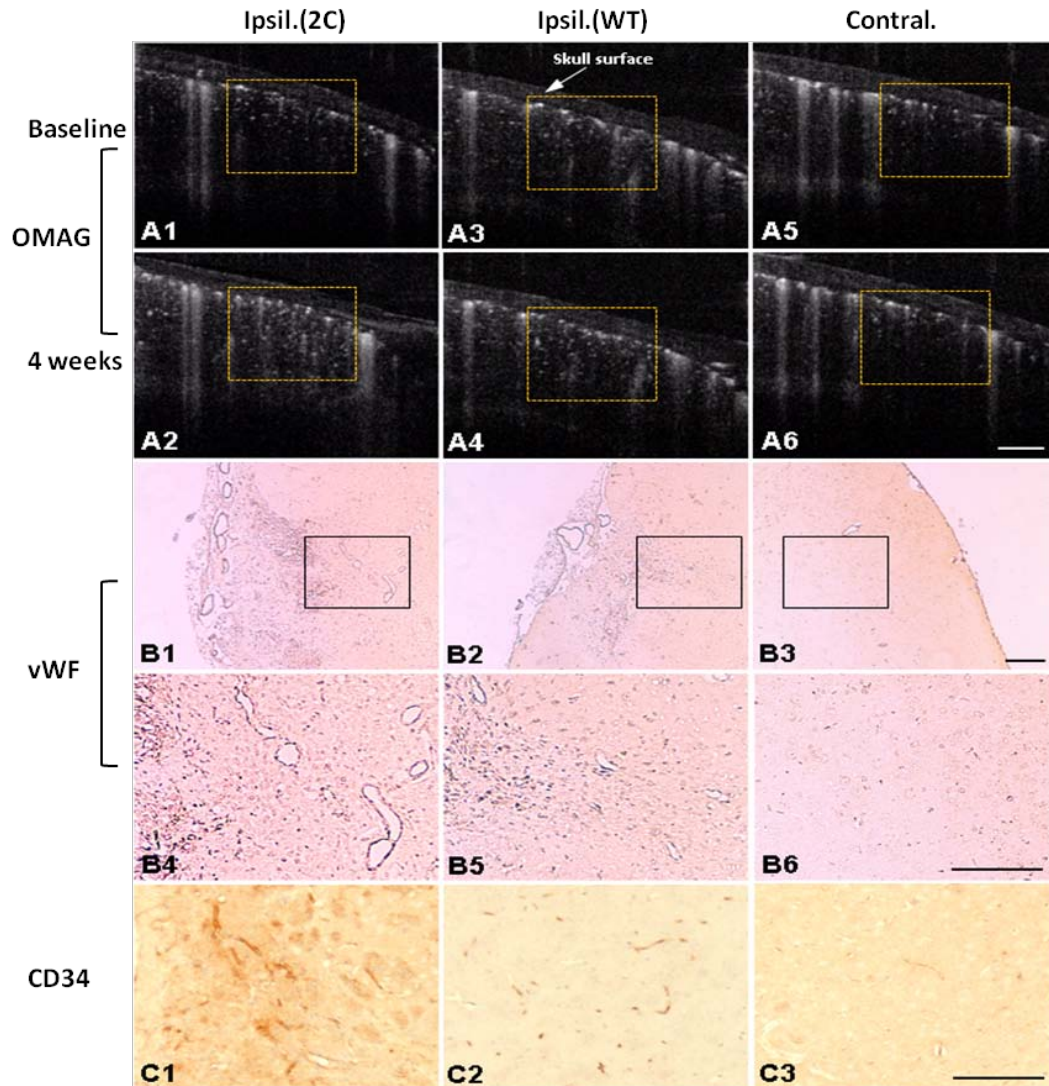
Figure 3.9 Cross-sectional OMAG perfusion images (A1-A6) and immunohistochemical method, vWF (B1-B6) & CD34 (C1-C3) to show neovascularization at ischemic penumbra. OMAG detected the increased vessel density at ipsilateral side at week 4 after stroke in 2C mice (A2) and WT mice (A4) as compared with their corresponding baseline (A1&A3), but this rise is more significant in 2C mice. The comparison from contralateral sides between baseline (A5) and week 4 (A6) shows no evident difference. vWF staining shows vessel density at penumbra is highly increased in 2C mice (B1) and WT mice (B2) when they are compared with the homologous area in the contralateral side (B3). The enhanced increase of vessel density along with enlarged vascular lumens is shown in 2C mice. B4-B6 corresponds to the regions in the boxes in B1-B3. CD34 exclusively confirmed newly formed vessels during stroke recovery. More new microvessels densely stained in 2C mice (C1) than those in WT mice (C2), and new vessels are barely recognized in the contralateral hemisphere (C3). Bars indicate 500µm.

3.2.5 Discussion

In our experiments, cerebral perfusion images of OMAG are achieved by the efficient separation of the moving scattering elements from the static scattering ones, i.e., the signals measured here by OMAG directly relate to blood vessels and is only sensitive to functional blood flow. In addition, the imaging contrast of blood perfusion in OMAG is based on endogenous light scattering from moving blood cells within blood vessels; thus, no exogenous contrast agents are necessary for imaging. Its signal and imaging characteristics permit OMAG repeatedly monitor hemodynamic changes during MCAO. Our imaging results from short-term observation on baseline and 30 mins after onset of occlusion illustrate OMAG is capable of precisely documenting the drop of blood flow in ischemic hemisphere. The comparison between WT and sEHKO mice demonstrated OMAG is sensitive enough to distinguish the amount of residual blood flow among different groups. The quantitative results from OMAG are almost consistent with the measurements from LDP. It is noted that LDF reflects brain surface perfusion and depicts the relative change in perfusion and OMAG we used here can provide quantitative blood volume values and apparently the std. in **Fig. 3.7B** is larger than that of LDP in **Fig. 3.7C** due to the enhanced sensitivity using OMAG.

Additionally, OMAG permits 3D monitoring of microvasculature down to capillary level, so it was expected to be used to detect the cerebral neovascularization after ischemic stroke. It also can be expected that OMAG may prove useful in evaluation the effectiveness of therapeutic intervention on the neovascularization after stroke that is probably related to the anti-stroke medication and therapies. The long-term study demonstrated that OMAG not only can detect neovascularization after stroke, but can also distinguish the difference of neovascularization between WT and 2C animals. By projecting 3D blood flow signals in one X-Y plane, the neovascularization was barely identified in WT mice, although we did find some new blood signals on ischemic area in 2C mice. However, by extracting the cross-sectional image in X-Z plane, the depth-dependent signals from neovascularization and their difference was revealed in both WT

and 2C mice. The newly formed vessels are found to be located around the ischemic penumbral area rather than ischemic core area which is consistent with previous reports [119-121]. The difference between two groups was also confirmed by histological measurements. We primarily tested our hypothesis that higher CYP-2C epoxygenase expression in cerebral vasculature resulting in higher production of EETs contributes to more neovascularization during post-ischemic phases. Although we only provided the cross-sectional information in this study, there is no doubt that OMAG has a lot of potential to do quantitative measurement on neovascularization after stroke. Here, it should be noted that in the cross-sectional OMAG images, there are apparent "shadows" which run perpendicularly to the cortical surface (e.g. **Fig. 3.9A**). This "shadowing" effect is primarily due to the strong forward or backwards scattering of the red blood cells in the large vessels. This effect results in the loss of perfusion signal under the vessel and therefore will also affect the future quantitative results. However, if the relative comparison only exists between the same regions of same animals at different time point, this "shadowing" effect will be minimized.

It has been shown that active neovascularization expressed as increased microvessel density develops in the penumbral area both in patients with cerebral stroke [88] and in experimental stroke in rats [119-121]. Although post-stroke neovascularization has been recognized, a convincing method is required to evaluate the treatments which drive vascular activity. In our study, by increasing the expression of EETs in cerebral blood vessels, which can promote vasodilation and angiogenesis, we proved the capability of OMAG on assessment of pro- neovascularization agents and also tested our hypothesis that higher level of EETs due to high expression of CYP-2C epoxygenase in cerebral vasculature contributes to more neovascularization during post-ischemic phases.

3.2.6 Conclusion

In summary, the present study demonstrates, for the first time, OMAG can be used to investigate the vascular response to cerebral ischemia and neovascularization in the post-ischemic period. We found that deletion of sEH increases residual blood flow which is in

agreement with our previous observation that the down-regulation of sEH contributes to the up-regulation of blood flow in response to focal vascular occlusion. We further found that over expression of CYP-2C epoxygenase will enhance the neovascularization after stroke that has not been reported in previous studies.

3.3 In vivo optical imaging of functional microcirculations within meninges and cortex[2]

As demonstrated in the above sections, OMAG is a wonderful tool for imaging cerebral blood flow, especially cortical blood flow in the animal models we studied. However, it has yet to uncover its significance for the study of brain diseases related to meningeal circulation. In this section, we report a new version of OMAG with sensitivity enhanced, and its performance on imaging slow blood flow in meningeal layers. Here we use a simple chemical-induced thrombosis mouse model to show OMAG can chronically and quantitatively monitor meningeal vascular responses to insult and aim to show its potential in studying migraine pain, a vasomotor instability of the meningeal circulation.

3.3.1 Abstract

Abnormal microcirculation within meninges is common in many neurological diseases. There is a need for an imaging method that is capable of visualizing dynamic meningeal microcirculations alone, preferably decoupled from the cortical blood flow. OMAG is a recently developed label-free imaging method capable of producing 3D images of dynamic blood perfusion within micro-circulatory tissue beds at an imaging depth up to ~2 mm, with an unprecedented imaging sensitivity to the blood flow at ~4 μm/s. In this paper, we demonstrate the utility of OMAG in imaging the detailed blood flow distributions, at a capillary level resolution, within meninges and cortex in mice with the

---

cranium left intact. By use of a thrombotic mouse model, we show that the OMAG method can yield chronic measurements of meningeal vascular responses to the insult decoupled from the responses in the cortex, giving valuable information regarding the localized hemodynamics along with the dynamic formation of thrombotic event. The results indicate that OMAG can be a valuable tool for the preclinical models to study therapeutic strategies to mitigate various pathologies that are mainly related to meningeal circulations.

3.3.2 Background

Meninges are the system of membranes enclosing central nervous system (CNS), which consists of three histological layers, i.e., the dura, the arachnoid and the pia. The dura is traditionally considered as an inert, fibro-elastic membrane, serving largely the mechanical and periosteal functions [104, 122]. Review of the anatomy reveals that the dura is not a simple fibrous tissue covering, but a complex structure innervated with dense micro-blood vessels [123]. Recently, a complete description of dural vascularity is made possible by use of the radiography, microdissection, clearing and histology techniques [124]. The postmodern studies show the presence of a fine anastomotic network emerging from middle meningeal arteries, located close to the bone. Despite the fact that the branches of arterioles in the dural membrane supply the metabolic needs of the cranium, it was speculated that this dural plexus is likely a source of collection of blood or fluid in subdural space caused by traumatic or nontraumatic subdural hemorrhage (SDH) and may be responsible for the causes of migraine and meningiomata [125]. A more thorough understanding of this dural plexus in terms of its hemodynamic response to the internal or external stimulus and its interaction with the pial or cortical microvessels may help to reveal mechanisms behind a number of pathological and physiological conditions that involve meningeal blood circulation, for example migraine.

In the past, the functional magnetic resonance imaging (fMRI) [126] provides an unsurpassed tool to image non-invasively the hemodynamic response of meningeal vessels in pre-clinical as well as clinical settings. However, interpretation of fMRI data is often confounded by relatively poor specificity to vascular events because current fMRI,

even at its highest imaging resolution, cannot resolve the detailed dural vascular plexus and its functional blood flow. Therefore, there has been a constant search for a noninvasive/minimally-invasive optical imaging technique that can be applied in preclinical animal models as a guiding tool and as an alternative to standard angiography requiring contrast agents or excisional biopsy. Optical imaging methods such as laser speckle imaging [127] have shown the ability to visualize dural vessels with spatial resolution of ~50µm, as well as to delineate hemodynamic response based on the Doppler effect induced by moving blood cells. Despite these advantages, this 2D imaging modality is not capable of providing the depth-resolved imaging of microcirculation. Thus, its measurement of vascular responses in the dura would most likely be contaminated by those from the cortex. Two-photon microscopy [128], a widely used laboratory imaging technique capable of ultrahigh resolution (~1 µm) imaging, has been used to provide specific and accurate morphological information of blood vessels in the dura. In doing so, however, it requires removal of intervening bone to access the dura and cortex since its imaging depth is only up to 200 µm, which is not desirable for repeated and long-term imaging studies. In addition, it requires injection of fluorescent tissue markers, which may complicate the interpretation of the results [129].

OMAG [63] is a novel extension of optical coherence tomography technology [58, 60], which is capable of producing 3D images of dynamic blood perfusion within micro-circulatory tissue beds at an imaging depth up to approximately one transport-mean-free-path below the surface (~2 mm in brain). OMAG produces imaging contrasts via endogenous light scattering from flowing blood cells within open vessels; thus, it is a label free imaging technology. Previously, we have demonstrated the feasibility of OMAG in imaging cerebral microcirculation in mice with the cranium left intact [130]. Due to its depth-resolved imaging capability, studies have also shown that OMAG was able to separate the blood circulations within the meninges from those in the cortex [131, 132]. In these studies, the rich capillary loops within the meninges were not imaged, even though large vessels such as the meningeal arterioles and venules were clearly imaged. This failure is attributed to that the previous reported OMAG system was only capable of

imaging minimal blood flow at ~160 µm/s, limited by the optical heterogeneous property of the cranium and brain tissue [74, 132]. However, the blood flow in the meningeal vessels, particularly in the capillaries, is very slow, ranging from tens of microns per second (in capillaries) to millimeters per second (in large vessels) [104]. In order to visualize the capillary plexus in dura mater, the sensitivity of OMAG to the blood flow must be improved.

Most recently based on OMAG, we have further developed an UHS-OMAG system [77], capable of imaging blood flows within patent vessels with an unprecedented sensitivity to the blood flow, ranging from 4 µm/s to 22.2 mm/s. With such high sensitivity to the flow, imaging of the true capillary blood flows within human skin [77] and human retina [133] were successfully demonstrated. The primary objective of this paper is to demonstrate the utility of the UHS-OMAG to image the detailed meningeal and cortical vasculatures at capillary level resolution. The secondary objective is to evaluate the capability of UHS-OMAG for *in vivo* chronic imaging of dural vessel morphology and blood flow changes in mice under both healthy and pathologic conditions. To achieve this, we adopted a well-established, ferric chloride-induced thrombosis model [134]. Upon the topical application of ferric chloride on the cranium surface of a mouse, we used the UHS-OMAG system to image the dynamic thrombosis formation in meningeal and cortical blood vessels. The results from this dynamic study on induced microvascular thrombosis and occlusions within the meninges show that UHS-OMAG may provide valuable and useful information in the meningeal thrombosis research and the preclinical drug development.

3.3.3 Materials and Methods

All experimental animal procedures were performed in conformity with the guidelines of the US National Institutes of Health. The laboratory animal protocol for this work was approved by the Animal Care and Use Committee of Oregon Health & Science University (Portland, OR, USA).

3.3.3.1 UHS- OMAG system setup

The system setup used to achieve UHS-OMAG is shown in **Fig. 3.10A**, similar to the one used in our previous work [77, 130]. Briefly, the setup used a broadband infrared superluminescent diode (SLD) as the light source, which has a central wavelength of 1310 nm and bandwidth of 65 nm that provided a ~12 μm axial resolution in air (~8.9 μm in biological tissue). The light from the SLD was coupled into a fiber-based Michelson interferometer. The light emerging at the output of interferometer was sent to a custom-built high-speed spectrometer, which had a designed spectral resolution of ~0.141 nm that provided a detectable depth range of ~3.0 mm in air (2.22mm in biological tissue). To match the lateral resolution with the axial resolution while keeping sufficient depth of focus for imaging the meningeal vessels through the intact cranium, we improved the sampling arm optics by having the beam diameter of ~3 mm and using an objective lens with a focal length of 30 mm (**Fig. 3.10B**). With this modification, the system provided a measured lateral resolution of ~9 μm and a depth of focus of ~ 400 μm. Because the average size of capillary vessel is about 10 μm, we expect that the system with designed spatial resolution of ~10 μm in x-y-z would be able to image the capillaries in the intracranial dura mater. The system sensitivity was ~105 dB measured at the focal spot of the sampling beam with ~3.0 mW power of light incident on the object and an exposure time of ~21.0 μs.

When imaging, the sample beam was rapidly scanned over the sample with a x-y scanner, while the line-scan camera in the spectrometer was continuously recording the OMAG signals formed between the reference and the sampling light. The camera was running at 47,000 Hz, meaning that the imaging speed was 47,000 depth-scans (A-scan) per second. With this imaging speed, we acquired 256 A-scans in the x-direction (B-scan) of 2.56 mm to form one cross-sectional image (B frame). This configuration determined the system frame rate at 180 frames per second (fps). In the y-direction, we captured a high density C-scan (i.e. y-direction scan), consisting of 1500 B-scans over 2.56mm. Accordingly, it required ~8 sec to acquire a complete 3D data volume of 2.56x2.56x2.22 mm^3. Then, a UHS-OMAG algorithm [77] was applied to this 3D data set to obtain

morphological and microcirculatory images of the scanned tissue volume. With this setup, our OMAG system is capable of imaging blood flow ranging from ~4 µm/s to ~22.2 mm/s [77], which is sufficient to image the meningeal blood circulation.
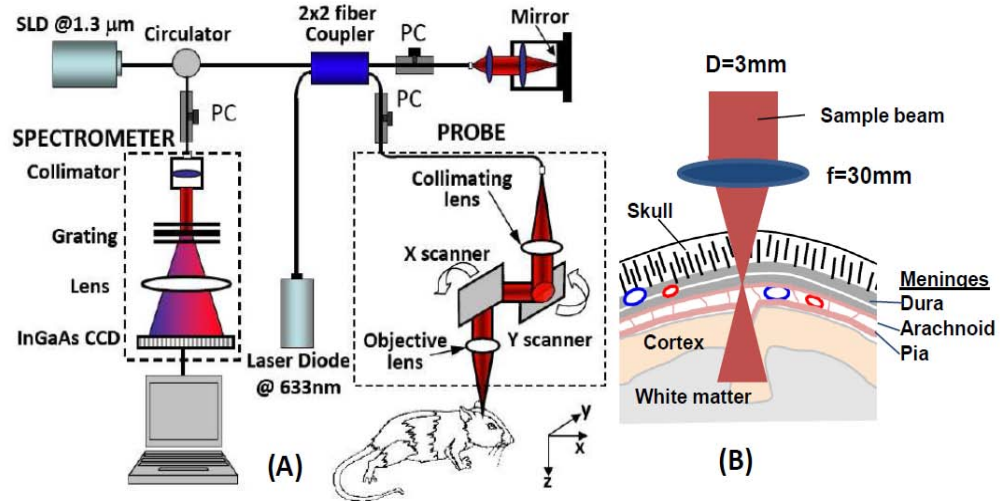
Figure 3.10 (A) Schematic of the UHS-OMAG system where PC represents the polarization controller. (B) Sketch of the designed probe beam targeting the meninges (drawing not to scale).

3.3.3.2 In vivo imaging

To test the performance of the UHS-OMAG imaging of the dural as well as cortical vascular networks *in vivo*, three-month-old C57 BL/6 mice were used in this study. The mice, each weighing 23 to 28 g, were prepared for OMAG one day before the experiments by shaving the heads followed by a depilatory cream to remove all remaining hair from the top of the scalp. During the imaging, the animal was immobilized in a stereotaxic stage and was lightly anesthetized with isoflurane (0.2 L/min O_2, 0.8 L/min air). The body temperature was kept between 35.5-36.5 °C by use of a warming blanket, and monitored by a rectal thermal probe throughout the experiment. An incision of ~1 cm was made along the sagittal suture and the frontal parietal and interparietal bones were exposed by pulling the skin to the sides. The animal was then positioned under the scanning optical probe, with the meninges carefully placed within the depth of focus of the probe beam (see **Fig. 3.10B**) as monitored by real time UHS-OMAG/OCT structural images displayed on the computer screen on the fly.

To better show the results, a volume segmentation algorithm [96] was then applied to each 3D UHS-OMAG image to isolate the blood flow signals in the meninges from those in the cortex. The segmentation resulted in two volumetric flow images, one for the meninges and the other for the cortex. The maximum amplitude projection was applied to each segmented meningeal and cortical volumes, resulting in the blood flow distribution maps. To evaluate the feasibility of using UHS-OMAG as a useful tool in characterizing meningeal blood flow over a larger area of dural mater, we collected the multiple 3D images over the different regions on the entire brain. The UHS-OMAG images from 16 different regions were then combined as a mosaic, covering an area of ~10×10 mm^2 over the entire mouse head.

3.3.3.3 Thrombosis experiments

To evaluate the capability of UHS-OMAG for *in vivo* longitudinal imaging of dural vessel morphology and blood flow changes. We adopted a well-established, ferric chloride-induced thrombosis mouse model [134]. With this model, vascular injury and thrombus formation were artificially induced. For UHS-OMAG imaging, an imaging region [~2.5mm(X)×~1.3mm(Y)] was selected next to the posterior coronal suture (PCS) as shown in **Fig. 3.13A**. Following Nagai et al [135], we induced thrombus formation via topical application of 10% FeCl$_3$-soaked paper (1×3 mm) placed over the exposed posterior coronal suture along the dotted outline shown in **Fig.3.13A**. The piece of paper was then removed after 5 min and the administration region was washed twice with warm saline. The microvascular occlusion and thrombus formation was monitored in real time by the optical imaging system. 3D optical data set were acquired once every five minutes for total 35 min since the application of FeCl$_3$.

3.3.3.4 Blood flow quantification

To quantify the meningeal blood flow, we applied the phase-resolved technique [67] to the UHS-OMAG flow signals, which measures the phase changes in optical signal due to flowing erythrocytes [74]. Because the phase changes linearly relates to the velocity of moving particles, we calculated the phases from adjacent B-scans collected at the same

position, and then the absolute velocity was obtained by converting the calculated phases to the velocities scaled by the Doppler angle. The Doppler angle was obtained from the 3-D blood vessel network because the angle of the incident beam was known *a priori*. Five repeated B-scans at each location were collected at each x-y position for phase estimation. This method has previously been validated in flow phantoms [77]. Cross sectional flow profiles across the vessels of interest were fit to a second-order polynomial and corrected for the angle of incident beam to provide the velocity in millimeters per second, from which the mean blood velocity (V_{mean}) and the vessel inner diameter (D) were determined. The flow rate in the vessel was calculated as a product between the average velocity and the cross sectional area of the vessel $\left[V_{mean} * \pi * \left(\frac{D}{2} \right)^2 \right] [V_{mean} * \pi * (D/2)^2]$. The blood volume in the imaging region in each time point was evaluated from the UHS-OMAG 3D flow data and then normalized by the baseline.

3.3.4 Results

3.3.4.1 Imaging of meningeal and cortical microvascularization

The depth-resolved imaging results using UHS-OMAG for blood perfusion within an area of ~2.5×2.5 mm^2 are shown in **Fig. 3.11**. **Fig. 3.11A** gives one typical cross-sectional image (B-scan) within the UHS-OMAG structural volume, which is identical to the conventional OCT image where typical morphological features, such as cranium and cortex, are visualized. **Fig. 3.11B** gives the corresponding blood flow image obtained from UHS-OMAG, where the micro-blood flows (e.g., pointed by arrows) originating from the dura mater as well as the rich cortical blood flows are clearly identified. Considering that the dural plexus is a vascular network exclusively above the cortical plexus, the flow signals above the cortical layer were simply treated as signals from the dural vessels, which were usually at the depths from 100 to 200μm below the cranium surface. With this as the reference, we applied the segmentation algorithm [96] to separate the blood flows within the meninges from those in cortical layers. This segmentation resulted in the blood flow distribution maps shown in **Figs. 3.11C** (meninges) and **3.11D** (cortex), respectively. From **Fig. 3.11C**, the dural blood vessels

are seen to be tortuous. Further, the large vessels do not greatly diminish in size, in spite of giving off many side branches. More importantly, the UHS-OMAG is capable of visualizing the rich anastomotic, as well as the splitting vessels (e.g., pointed by the arrows) in the meninges. These appearances of the dural vessels are directly resulted from characteristic slow blood circulation in the intracranial dura mater. These findings from the UHS-OMAG correspond well to what is called the primary or secondary anastomotic network in standard dural histopathology [123]. Because of its capability of imaging much slower blood flows, it is not surprising that UHS-OMAG gave an image of greater vascular density for the cortex (**Fig.3.11D**).
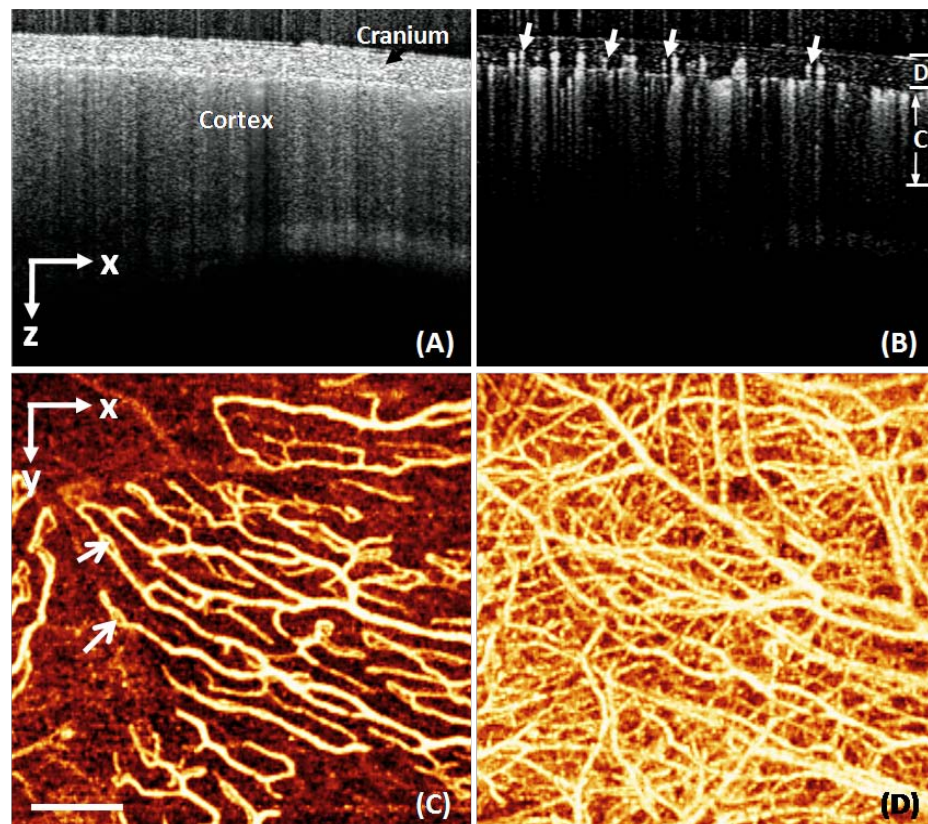
Figure 3.11 Typical in vivo UHS-OMAG images of the cerebral microcirculation in mice. Images were taken with the skull left intact. (A) is one typical UHS-OMAG cross-sectional image (B-scan) of microstructures showing morphological features, such as cranium and cortex, and (B) is the corresponding blood flow image where the dural microvessels (e.g., pointed by arrows) are distinguishable from the vessels in cortex. The projection maps of functional blood vessel network within (C) the meninges and (D) the cortex, respectively, obtained from one 3D scan. White bar = 500µm.

Fig.3.12 shows whole-brain mosaic flow images from both the dura (**Fig. 3.12A**) and cortex (**Fig. 3.12B**), providing volumetric measurements of detailed microcirculation through the vascular tree down to the capillary level with the skull left intact, without a need for dye injections, contrast agents, or surgical craniotomy. The dural vessels are seen to distribute unevenly as they course over the dural surface. The fine vascular network is concentrated on three typical sutures, ie, sagittal suture (SS), anterior coronal suture (ACS) and posterior coronal suture (PCS), and in the non-suture area cross-linked blood vessels are directed more towards the posterior than the anterior segment (**Fig. 3.12A**). These features from dural vessels do not resemble those of cortical vessel distribution (**Fig. 3.12B**). Such appearances observed from UHS-OMAG are consistent with the vascular convolution described in the well-known references [122, 124], demonstrating potential power of the UHS-OMAG in the investigations of neurological diseases and complications that may involve the meningeal microcirculations.
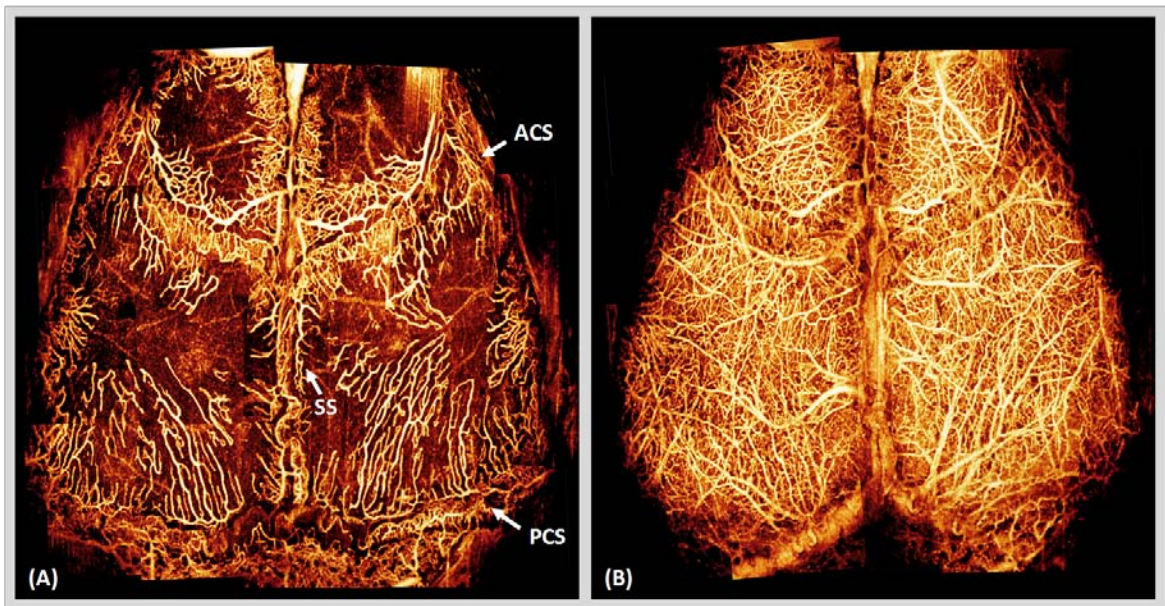
Figure 3.12 The functional blood flow networks of the entire brain in mice were imaged by UHS-OMAG in vivo. Because of its depth-resolved imaging capability, OMAG is capable of providing simultaneous imaging of microcirculations within (A) the meninges and (B) the cortex of a mouse. SS, sagittal suture; ACS, anterior coronal suture; PCS, posterior coronal.

3.3.4.2 Dynamic imaging of thrombosis within meninges and cortex

Meningeal or cortical blood vessel occlusions due to the thrombus formation can occur in diseases and pathophysiological processes. An ability to non-invasively image microvasculature in preclinical models is useful for testing and evaluating new thrombolytic drugs capable of dissolving thrombi or preventing thrombus formation.

Figure 3.13 shows dural microvascular network of a region in a mouse during thrombus formation initiated by the topical application of $FeCl_3$. Progress of the occlusion and the subsequent effect on the functional vessels were observed for 35 minutes with the UHS-OMAG data sets acquired every five minutes. **Figure 3.13B** shows the time serial images of the region outlined by the small box in **Fig. 3.13A**, which shows the gradual change in functional vessel density as thrombi formed over time. Vascular occlusion gradually propagated over approximately 35 min, resulting in decreased functional vessel density due to restricted and occluded blood flow. To examine the blood flow dynamics in more detail, relative flow magnitude were assessed in each single vascular branch in these serial optical reflectance maps. According to the location of the applied $FeCl_3$ solution and the occlusion sequences from the optical images, four main side-branches could be identified in the imaged region as shown in **Fig. 3.13C** where different vessels are differently colored and the numbers denote their occlusion sequence. It was interesting to note that in some vessels when thrombosis was formed in the distal end of vessels, the blood flow was ceased gradually in a direction to their main branch; and when thrombosis was formed in the main branch of vessels, the blood flow in the lower branches was ceased rapidly. For example, in vessel 2, the microvascular occlusion was firstly developed in the distal end ("D" in **Fig. 3.13C**) because the $FeCl_3$ solution is more easily absorbed by capillary with one-cell thickness vascular wall, and then the main branch ("M" in **Fig. 3.13C**) was occluded probably due to its position priority. This was followed by a rapid drop in the flow in the remaining part of the same vessel. Therefore, this vessel was an arteriole, flowing from the main branch to its distal end. These sequential events also inform that the thrombotic plugs were dynamic structures that expanded during the observation period of 35 min and grew

from the distal end. Moreover, within the region we observed, complete cessation of the blood flow only occurred in the vessel 1; whereas the vessels 2 and 3 did not even though their flow was dropped dramatically. Another interesting phenomenon is that the blood flow in some branches was decreased initially, but later was compensated by those from the branches connected with the functional neighboring vessels.
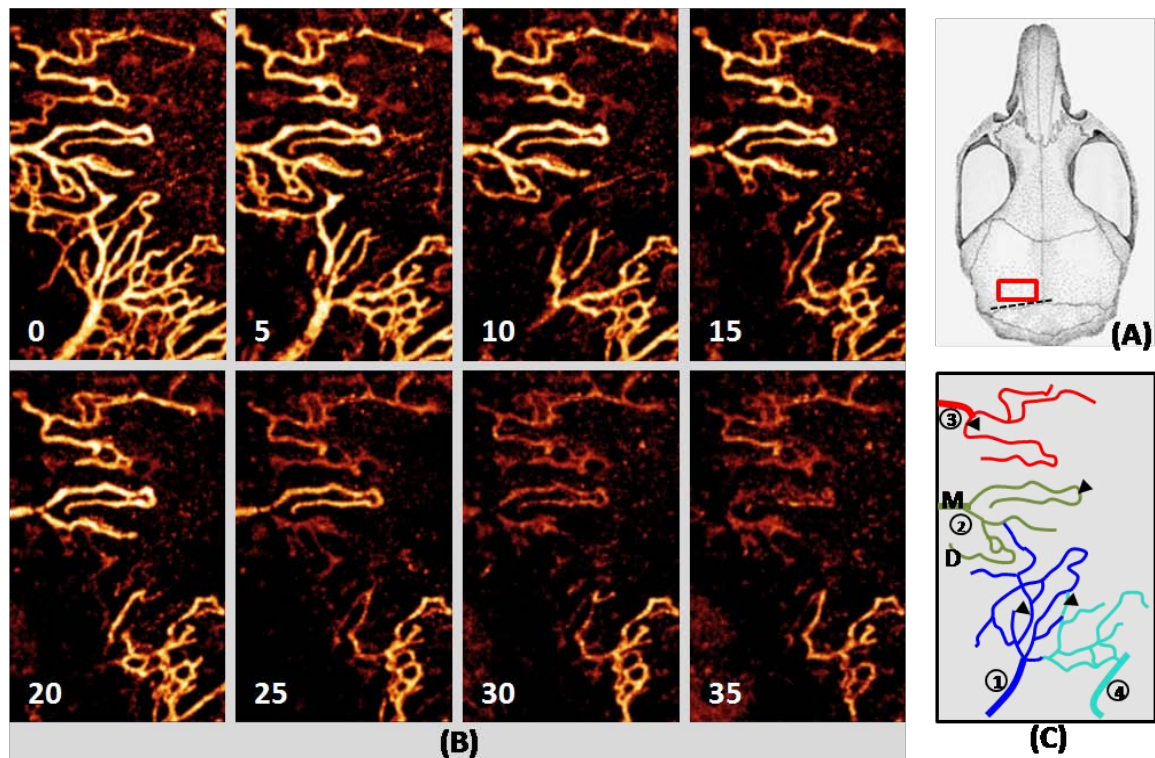
Figure 3.13 Representative meningeal microvascular network during thrombus formation induced by FeCl₃. (A) is a sketch of the mouse skull; the red box indicates the region imaged by UHS-OMAG and the dotted line indicates the place where the $FeCl_3$ was topically applied. (B) shows serial OMAG images of microvascular occlusion and blood flow changes, indicating development of thrombus for the region shown in (A). Numbers in the bottom left corner of each panel are minutes after application of $FeCl_3$. (C) is a vascular sketch based on the vascular occlusion sequence in (B), where four vessels are indicated in different colors, the numbers indicate their occlusion sequence and the arrows show four regions of interest in which blood flow will be quantified.

Besides the dynamic imaging of the meningeal vascular flow, the flow dynamics in the cortical layer can also be visualized by OMAG. As shown in **Fig. 3.14**, the dark shadows starting from the left bottom corner indicate a gradual propagation of the

thrombosis in the vicinity of FeCl$_3$ solution, resulting in an expansion of the occlusion front. This occlusion front advanced about 35μm/min during the observation period. Compared with the occluding speed within first 15 minutes, it seems that the occlusion front moved slower during the remaining 20 min of the observation period. In addition, from the growth of the occlusion in the cortex, it can be seen that the thrombosis mainly occurred on the side branches of the main vessel.
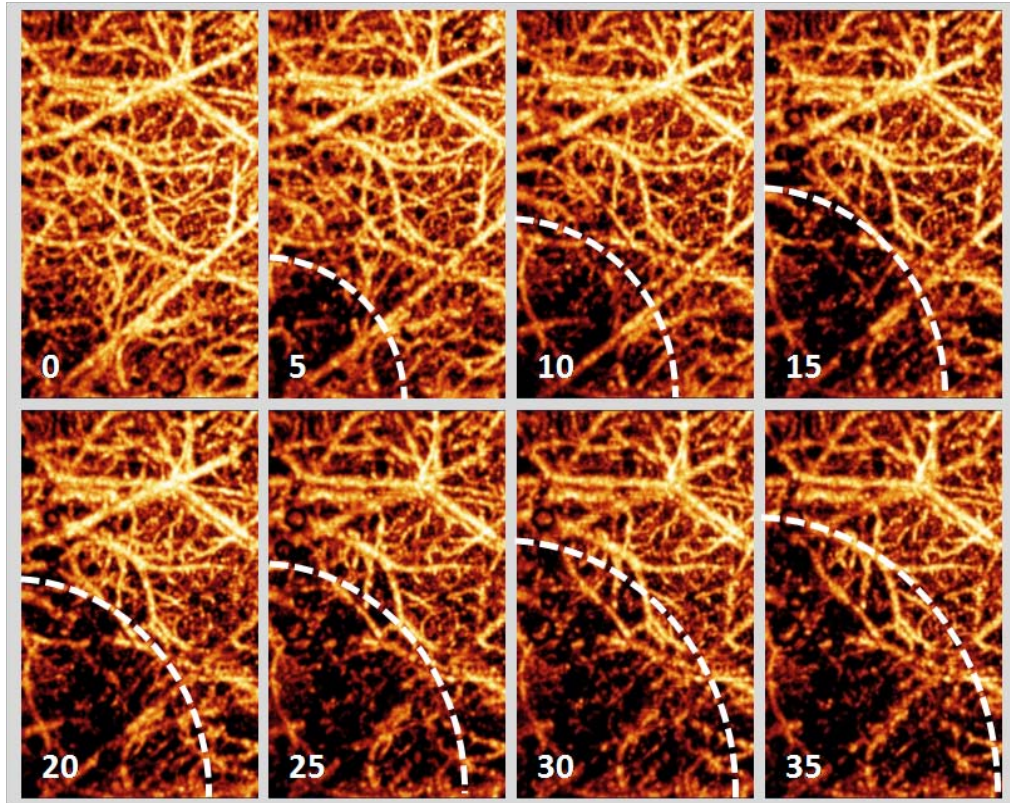
Figure 3.14 Representative cortical microvascular network during thrombus formation in the region shown in Fig. 3.13A. Numbers on the bottom left corner are minutes after application of FeCl$_3$. The dark shadows starting from 5 mins indicate a gradual propagation of the thrombosis in the vicinity of FeCl$_3$ solution, resulting in expansion of the occlusion fronts shown by the dotted outlines.

3.3.4.3 Quantitative measurement of meningeal and cortical blood flow during thrombosis

In order to be more informative about the thrombus growth and microvessel occlusion, blood flow on the microvessel level was quantified via UHS-OMAG. The velocity

profiles across the dural vessels 1 and 2 (**Fig. 3.13C**, pointed by black arrows) are shown in **Fig. 3.15** along with the second-order polynomial fit and the R-squared value of the fit at the time points as shown [0-15min (vessel 1), 15-30min (vessel 2)]. The shape and peak of the velocity profile changes with time, indicating the decrease in vessel diameter and flow velocity over the 35-min time course.
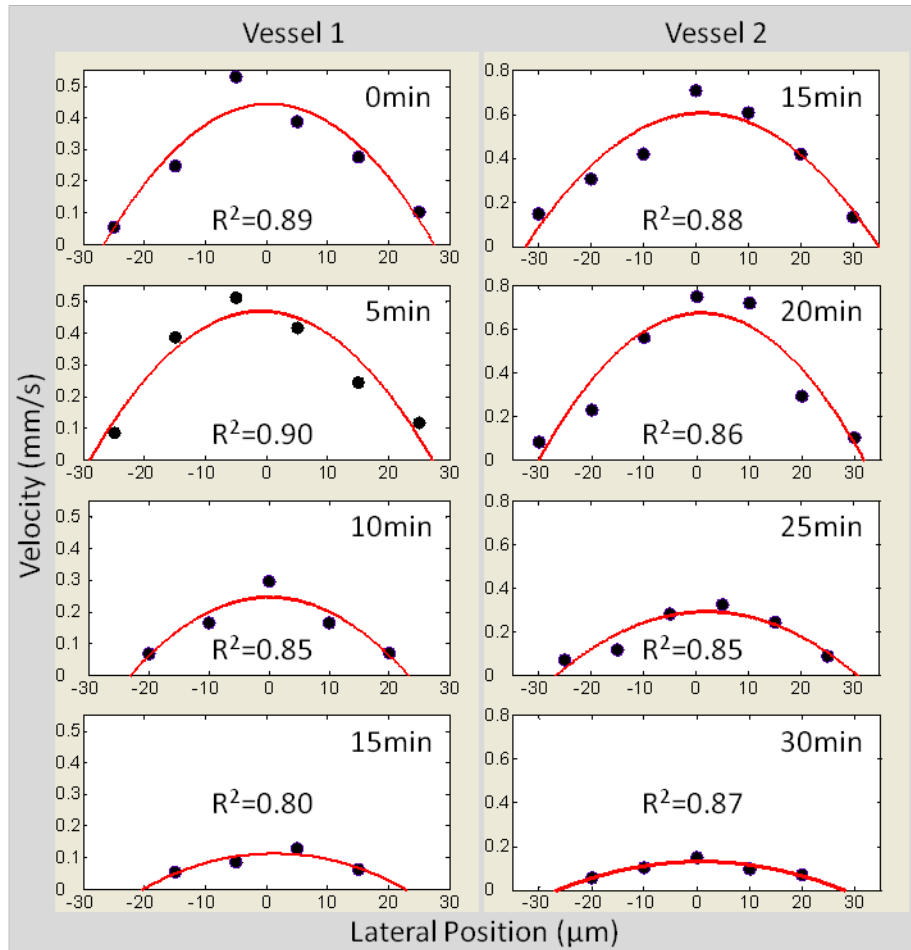
Figure 3.15 Plots of the velocity profiles across the dural vessels 1 and 2 pointed by arrows in Fig.3C, respectively, along with the second-order polynomial fit and the R-squared value of the fit at the time point as shown [0-15min (vessel 1), 15-30min (vessels 2)]. The time of imaging in minutes is given in the upper right corner of each plot.

Figure 3.16 shows quantitative measurements of the mean velocity (**Fig. 3.16A**), the vessel inner diameter (**Fig. 3.16B**), and the flow rate (**Fig. 3.16C**) over the 35-min time course for four individual feeding vessels (numbered in **Fig. 3.13C**). These plots indicate that all variables change with time. Each vessel appears to vary differently with

time, especially in terms of the velocity (**Fig. 3.16A**) and flow rate (**Fig. 3.16C**) parameters. For example, the vessel 1 reacted more rapidly than other three vessels. In vessel 2, the three parameters were slightly over the baseline during a period from 5 minutes to 20 minutes after the topical administration of $FeCl_3$ and then decreased dramatically. In vessel 4, the blood flow was down to its extreme low point at 20 minutes and then slowly reperfused by its proximal bypass connected to another vessel. Despite discrepancy between them, the velocity and blood flow in all regions at 25 minutes declined to at least 50 percent of their baseline. Comparing the baseline with the endpoint, the vessel diameter did not diminish greatly except the vessel 1.
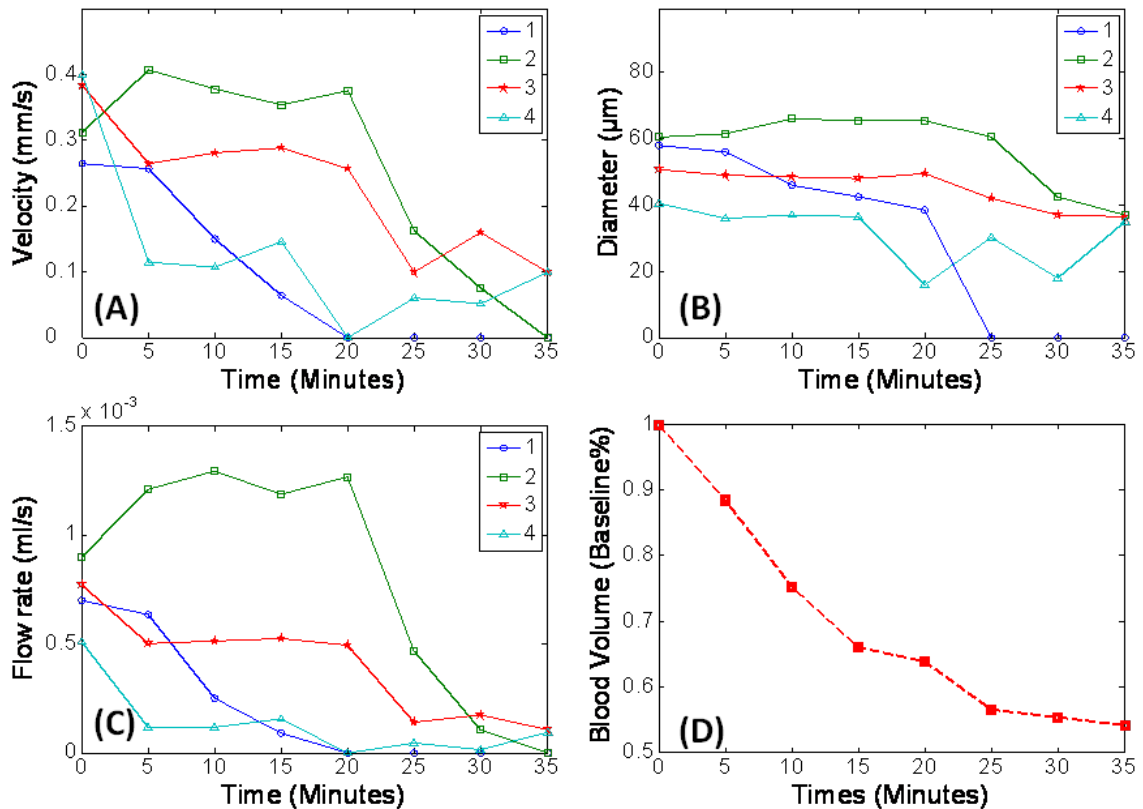
Figure 3.16 Quantitative measures of the vessel mean velocity (A), vessel inner diameter (B), and flow rate (C) over the 35-min time course in four individual feeding vessels (see Fig. 3C), following the induction of thrombus. The time evolution of blood volume changes in cortex for the imaged region is shown in (D).

With respect to the flow dynamics in cortex, the time evolution of blood volume is shown in **Fig. 3.16D**. There was a significant decrease from the baseline to 25 minutes

and a slight decline during the remaining 10 minutes. This is in agreement with the results observed from the meningeal vessels that indicated that 25 minutes is a critical transition point.

3.3.5 Discussion

The optical imaging method presented in this article provides an attractive alternative to other methods because of its ability to accurately image the meningeal and cortical blood flow responses in living animals over an area of a few millimeters with the cranium left intact. This imaging modality is non-invasive, relatively inexpensive, and fast. These attributes are well suited for long-term repeated measurement of blood flow *in vivo*. Through comparison of the time-lapse 3D images, the dynamic alterations of microcirculation associated with the cerebral pathophysiologic events, such as thrombosis, can be observed. More importantly, due to the depth-resolved feature of the UHS-OMAG, the dynamic responses of the microcirculation within the meninges can be decoupled from those in the cortex.

In addition to its capability of visualizing the detailed functional microcirculation (e.g. **Figs. 3.11 and 3.12**) and the relative flow distribution along the whole pathological event (e.g. **Figs. 3.13 and 3.14**), UHS-OMAG is able to quantify the flow-related parameters, such as velocity, vessel diameter and flow rate of the individual vessels of interest, which are critical in investigating the cerebral flow responses to a certain insult. With a sensitivity to the flow as low as 4µm/s, we believe that the reported UHS-OMAG imaging technique is the most precise method to date for quantifying localized blood flow and visualizing the detailed microcirculations within the scanned tissue beds *in vivo*.

Any cerebral blood flow is tightly coupled to the underlying neuronal response. The meningeal blood flow has no exception. It is crucial to monitor the spatial and temporal extent of the meningeal blood flow changes in the studies of functional activation and pathophysiologic conditions accompanied by uncoupling, such as the thrombosis. Optical imaging of the functional microcirculations using UHS-OMAG showed the gradual formation of the chemically induced thrombi and the effects of the thrombi on the microcirculation within the meninges and cortex. With the help of the

flow quantification algorithm on the serial 3D datasets, OMAG can provide the dynamic flow parameters due to thrombosis formation and micro-vessel occlusion. The results may give additional useful information, if together with the systemic physiological measurements, to assess local micro-vessel physiology during a thrombotic event. Real-time imaging of the thrombotic event as well as its associated changes in microflow parameters is also useful in the development of new therapeutic agents designed to treat the pathological thrombi, because OMAG makes it possible to observe subtle differences in the timing and the magnitude of drug action on the microvessel physiological response and thrombus formation.

As shown in this study, one of the advantages of the OMAG technique over other methods, such as laser speckle, is that it provides sufficient depth resolution to differentiate the contributions of the meningeal microcirculations from those of the cortical vessels. This ability would make the UHS-OMAG a useful and attractive tool in the investigations of the meningeal hemodynamic responses to other functional activation or neurovascular disorders, such as migraine headache, in which the changes in blood flow within dural vessels play an important role in the etiology, pathogenesis, prognosis, and responses to treatment.

3.3.6 Conclusion

We have demonstrated the utility of the ultrahigh sensitive OMAG in imaging the detailed blood perfusion distributions, including capillaries, within meninges and cortex in mice with the cranium left intact. We have shown that the UHS-OMAG method is capable of yielding longitudinal measurements of vascular responses to the thrombotic treatment, unraveling the localized hemodynamics along with the dynamic formation of the thrombosis event. Therefore, we expect that UHS-OMAG can be a very useful tool in guiding the design and development of therapeutic strategies to mitigate the microcirculatory complications occurring in pathophysiological conditions, such as migraine.

Chapter 4

Assessment of Optical Micro-AngioGraphy in Peripheral Blood Flow

As opposed to blood that flows to the vital organs, PBF refers to blood flow to extremities. PBF plays a prominent role in maintaining normal metabolism of tissues in lower extremities, such as skin, muscle and nerve [27]. Plenty of diseases are associated with the aberration of PBF, for example, PAD [35] and DPN [38]. To date, LDF is the widely used method to study dynamics of PBF, and microscopic method is the best candidate to study the detail of peripheral microvasculature. The studies presented in Chapter 4 discuss an example of an application of OMAG on PBF. Except that OMAG can discover the microvasculature of peripheral nerves, in this study DPN animal model established in our collaborator's lab was used to demonstrate OMAG can track and differentiate the functional changes of PBF caused by stimulant in normal and diabetic mice.

4.1 In vivo optical imaging of functional vasa nervorum and peripheral microvascular tree in diabetic mice[3]

4.1.1 Abstract

DPN is, at least in part, associated with the functional attenuation of vasa nervorum, the microvascular structure of peripheral nerves. Microvascular imaging options for vasa nervorum still remain limited. In this work, OMAG, a volumetric, label-free imaging technique is utilized for characterizing, with high resolution, blood perfusion of peripheral nerve in diabetic mice. We demonstrate that OMAG is able to visualize the structure of microvasculature and to quantify the changes of dynamic blood flow and vessel diameters during administration of vessel stimulator in both diabetic and normal mice. The results indicate the potential of OMAG to assess the blood supply of nerve involved in the pathology and treatment of DPN.

4.1.2 Background

DPN is the most common complication of diabetes mellitus, affecting up to 60% of diabetic patients [136]. Loss of sensation in the feet, the most frequent manifestation of DPN, frequently leads to foot ulcers and may progress into amputation of the limb [137]. Despite a continuous increase in the incidence of diabetes mellitus and DPN, the pathogenic basis underlying DPN has remained uncertain, and current treatments have yet to effectively treat DPN [138]. It has been noted in multiple previous reports that experimental DPN is characterized by reduced microcirculation in peripheral nerves resulting from the decrease in blood flow through the vasa nervorum, the microvessels that provide blood supply to peripheral nerves and thus the restoration of nerve blood flow supply may mitigate neuropathy despite persistent diabetes [139].

---

[3] This work has been published in *Journal of Innovative Optical Health Sciences.*[Y.L. Jia, and R.K. Wang, "Label-free 3D optical microangiography imaging of functional vasa nervorum and peripheral microvascular tree in the hind limb of diabetic mice", Journal of Innovative Optical Health Sciences, 3(4), 307-313 (2010)]

Accordingly, to investigate the association between the changes of blood flow in the vasa nervorum and DPN, and to further evaluate the treatments on DPN by administrating the factors increasing the nerve perfusion, a non-invasive technique for assessing blood perfusion in vasa nervorum (visualizing and quantifying blood circulation), would be of great value. Currently, the common research methods to study the vascular supply of peripheral nerves in diabetic animal models are fluorescent imaging of vascular architecture [140] and laser Doppler imaging of blood flow [141-143]. Although they have made significant contributions to our understanding of vascular pathology associated with DPN, their important limitations still remain. Fluorescent imaging cannot provide dynamic images on same animals due to its invasiveness and laser Doppler perfusion imaging only produces the relative values of blood flow and is only valid for the perfusion on the tissue surface. In this letter, we demonstrate a potential method for functional imaging blood perfusion of vasa nervorum in vivo.

OMAG [63] is a volumetric, label-free imaging technique that is recently developed in our group for imaging dynamic blood perfusion. The imaging is achieved by separating the signals backscattered by moving blood cells from those originated from tissue microstructures. Because its imaging contrast is based on endogenous light scattering from moving blood cells within biological tissue; thus, no exogenous contrast agents are required for imaging. Its imaging depth is up to 2mm in biological tissue and, Wang et al. recently demonstrated mouse brain imaging through both intact scalp and skull [96]. This noninvasive feature is highly desirable for functional or chronic studies. Its current spatial resolution (lateral resolution: 16μm, axial resolution: 8μm) allows to resolve microcirculations and even capillaries. Combined with phase-resolved method, now the second version of OMAG could extract flow velocities from flow signals and produce the flow map and velocity map simultaneously [74]. In this letter, in an attempt to show the potential of OMAG to visualize the dysfunctional microcirculation after DPN and monitor the regulation on blood flow after treatments, we used OMAG to noninvasively monitor the changes of blood flow in both diabetic and wide-type mice with topical application to the skin of sensory stimulant chemical, menthol.

4.1.3 Materials and Methods

4.1.3.1 Animal care

A total of 14 male mice (8 diabetic Ins2$^{Akita/+}$ and 6 non-diabetic, wild-type littermates, aged 16 to 24 months) were subjected to the OMAG. The animals originated from a colony of Ins2Akita mice that was established and maintained at the OHSU Animal Care Facility by mating heterozygous (C57BL/6-Ins2$^{Akita/+}$J) males (Jackson Laboratory strain number 003548) to wild-type (C57BL/6-Ins2$^{+/+}$/J) females.

4.1.3.2 OMAG in vivo imaging

The configuration and operating principles of OMAG system can be found elsewhere [74]. Briefly, the system used in this study employed a broadband infrared superluminescent diode with a central wavelength of 1.3 µm. The spectral interferogram formed by lights between the sample and reference arms was sent to a home built high-speed spectrometer that employed a line scan infrared InGaAs detector to achieve an imaging speed of 20 frames per second (fps) with 1000 A scans (axial scans) in each B scan (lateral direction). The system has the imaging resolution of $16\times16\times8$ µm^3 in the x-y-z direction, and an imaging depth of ~3mm in air.

The experimental protocol was in compliance with the Federal guidelines for care and handling of small rodents and approved by the Institutional Animal Care and Use Committee. Before functional optical imaging, the right hind limb of mice was shaved and depilated. In order to further improve the resolution of the images, a small patch was excised to form a small (~3×3mm^2) window over the subcutaneous tissues being imaged. During the imaging, the animal was immobilized in a custom made stereotaxic stage and was lightly anesthetized with isoflurane (0.2 L/min O^2, 0.8 L/min air). The body temperature was kept between 35.5-36.5 °C by use of a warming blanket, and monitored by a rectal thermal probe throughout the experiment. Saphenous nerve, a representative peripheral nerve, was chosen as imaging objective due to its superficial location and positioned under the scanning probe. The imaging area was kept moist under a piece of plastic foil. Before administrating sensory irritant, a control C scan (3D) and repeated B

scan of one minute were acquired as baseline for future comparison. The imaging sites of C san and B scan were shown by solid line box and dash line, respectively, in Fig. 1D. Then a little cotton ball was dipped in 40% menthol ethonal solution and gently loaded on the lower end of hind limb. Once menthol was administrated, B scan was initiated and repeated for six minutes. Then final C scan recorded the perfusion with stimulation on the same site as control. The total imaging acquisition time in this process was 8 minutes.

4.1.4 Results

4.1.4.1 Imaging of mouse nerve vessel anatomy and blood flow

The original raw data cube (spectral interferograms) was first processed frame by frame,

and then the resulted images, including structural, flow and velocity images, were combined to produces 3D volumetric visualization of the scanned tissue volume. The results for a typical limb tissue volume of 2.5x2.5x2.0 mm^3 are given in **Fig. 4. 1**. **Fig. 4. 1A** is a volumetric visualization rendered by merging the micro-structural 3D image with the corresponding 3D image of functional blood flows, where the precise location of blood flow can be identified with the microstructures of the tissue. In this image, a cut away view is utilized to show how the blood vessels are distributed in the tissue volume. **Fig. 4. 1B** shows the volumetric network of blood vessels within the scanned tissue volume, where the bundle of vessels indicated in a rectangle box was vasa nervorum running longitudinally in the saphenous nerve and beside the femoral artery and vein. It also can be noted that the longitudinal vessels in the epineurium are connected with one another by transverse anastomoses pointed by white arrows. To show in detail the blood vessel networks, the maximum projection approach was used to obtain x-y projection network in **Fig. 4. 1C**, in which numerous strips caused by the heart beat were clearly shown on the formal artery. The corresponding velocity information for the imaged blood flows are shown in **Fig. 4. 1E and 1F**. The directional flow information was coded with colors, where the green color means the blood moves toward the incident beam direction and red color otherwise. In the light of this, the vessels of varying flow direction are demonstrable within the microvascular architecture of the peripheral nerve.

Previous studies [144] reported the individual vascular cord in vasa neuvorum consists of nutrient arterioles, venules and capillary plexus. Although capillary plexus cannot be clearly delineated in our OMAG flow and velocity images due to the close positions between the arteriole and the venule, the cloudy flowing signals backscattered from capillary are distributed in the single vessel cord indicated by an arrow. Here, OMAG velocity images provide a potential tool to quantify blood perfusion within the microcirculation tissue beds in vasa nervorum *in vivo*.
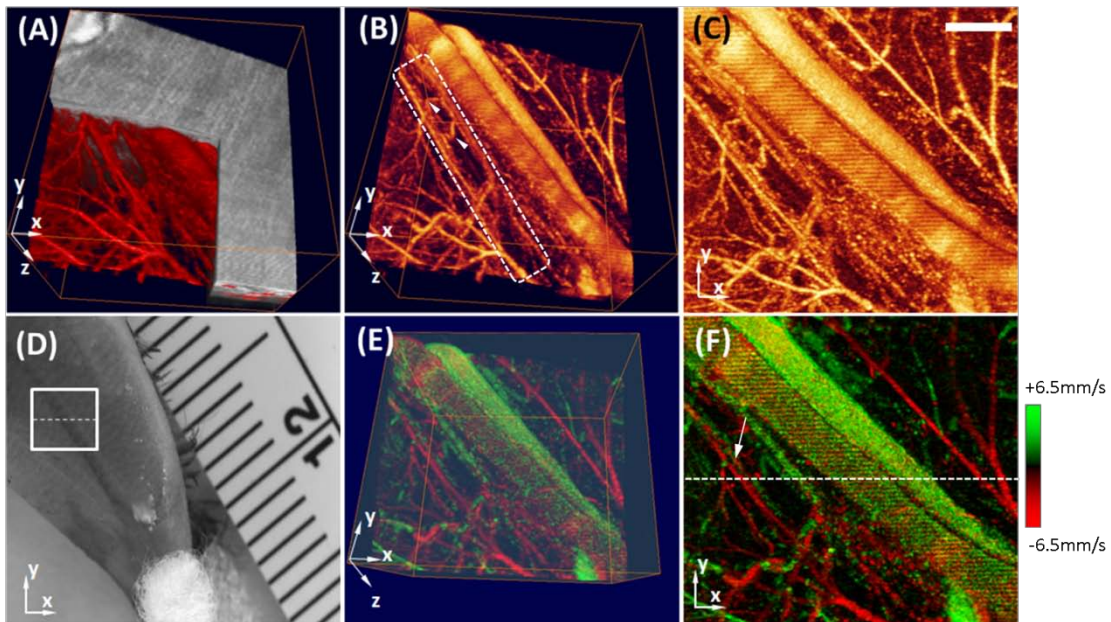
Figure 4.1 *In vivo* 3D OMAG imaging of the hind limb of mouse in the area covering a part of saphenous nerve indicated by open box in (D). The volumetric visualization was rendered by (A) merging the 3D micro-structural image with the 3D blood flow image, (B) the 3D signals of blood flow in Vasa Nervorum and vessels around it, (E) the corresponding image of velocities in 3D vascular network. (C) and (F) are the maximum projection view (x-y) of (B) and (E). The green color in (E) and (F) represents the blood moves towards the incident probe beam, and otherwise the red color.

Next, shown in **Fig. 4.2** are the representative results from a single B scan (frame) of a mouse hind limb, the position of which is indicated by the white dash line in **Fig. 4.1F**. **Fig. 4.2A** is the OMAG structural image, where the important histological structures, including the formal artery and vein, the nerve bundle. **Fig. 4.2B** shows the corresponding image of localized blood flow that permeates this cross-section in **Fig. 4.2A**. The flow velocity information along the light beam direction extracted from **Fig.**

4.2B is given in **Fig. 4.2C**. As has been expected, the flow velocity in the microcirculation at depth of ~1.5mm within the vasa nevorum is imaged by OMAG, which is circled by dash line. As a comparison, in **Fig. 4.2D**, a cross-section of mouse hind leg tissue immunostained is used to show the position of the blood vessel in the vicinity of the saphenous nerve. Saphenous nerve and its branches detected with a myelin basic protein antibody are shown in green. Femoral artery and vein detected with an antibody to CD31 are the large blood vessels with the lumen outlined in red. The endoneurial blood vessels belonging to the vasa nervorum of the saphenous nerve and the blood vessels belonging to the vasa nervori of the nerve branches are pointed by white arrows. A traditional H&E staining image in the left corner of **Fig. 4.2D** also shows the location of saphenous nerve and artery, but the endoneurial blood vessels are not easily distinguished.
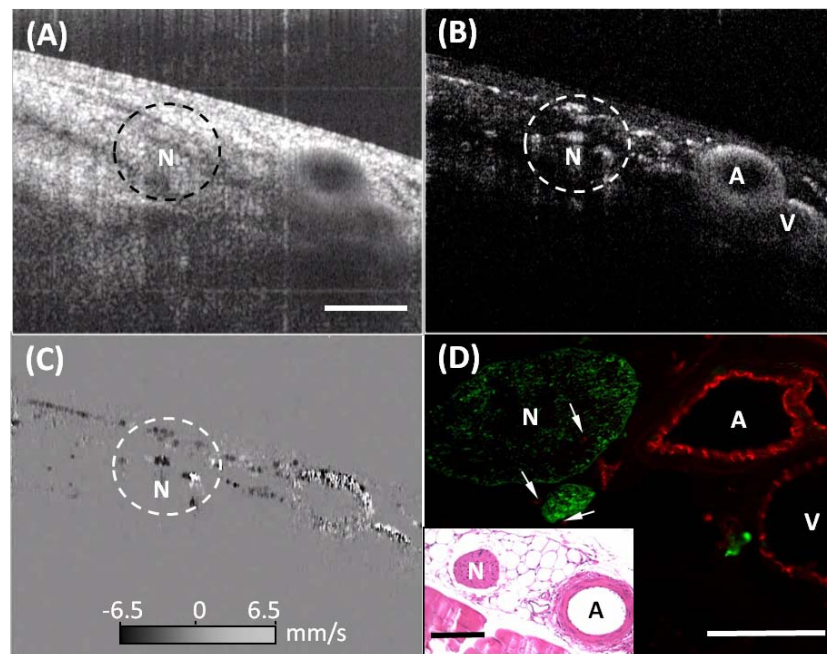
Figure 4.2 Comparison between in vivo OMAG (B-scan) and histological imaging of the Vasa Nervorum within peripheral nerve bundle of mice. Shown are the OMAG structural image (A), corresponding OMAG flow image (B) and OMAG velocity image (C), and histology images (D), respectively. N, nerve; A, artery; V, vein. Bars are 500µm.

4.1.4.2 Dynamic imaging of nerve blood flow stimulated by menthol

In addition to volumetric visualizing microcirculation within the vasa nevorum, the OMAG system enables us, by noninvasive means, to quantitatively examine the dynamic parameters of localized blood flow around or within nerve bundles, for example, the inner diameter of the vessel and the localized flow velocity and blood flow rate. The quantitative time courses of mean flow velocity with Doppler angle correction in the representative arteriole with same size in both diabetic and wide-type mice before and after the administration of sensory irritants, menthol, are presented in **Fig. 4.3A** and **3B**, respectively. The time point of stimulation is indicated by black arrows. It is noted that before the administration of this vessel stimulator (baseline), the diabetic animal is easily be distinguished from the wide-type one due to the lower blood flow velocity. After topical application of 40% menthol to the skin at a location 3mm distal to the skin window, the blood flow in single vessel of vasa nevorum was accelerated immediately and reached the maximum value (~3.2mm/s) within a few minutes in diabetic mouse. Whereas, the blood flow in wide-type mouse firstly dropped down to the eighty percent of baseline which probably caused by the normal sensitivity of peripheral nerve to skin cooling along with menthol ethanol solution and then continuously increase without maximum within the imaging time range possibly due to the proper mechanical properties of vessel walls. Compared to wide-type mouse, the vascular reaction on the temperature change was retarded in diabetic mouse, and the time duration of response to the stimulator was short, due to the vascular malfunction involved in the DPN.

Accompanying the increase of blood flow velocity, in both diabetic and wide-type mice, the inner diameters of vessels are also increased by comparison of two OMAG flow images between baseline and the end point (7th minute). An example from a diabetic animal is presented in **Fig. 4.3C** and **3D**. The vasodilation in vasa nevorum are clearly indicated by white arrows in **Fig. 4.3D**.
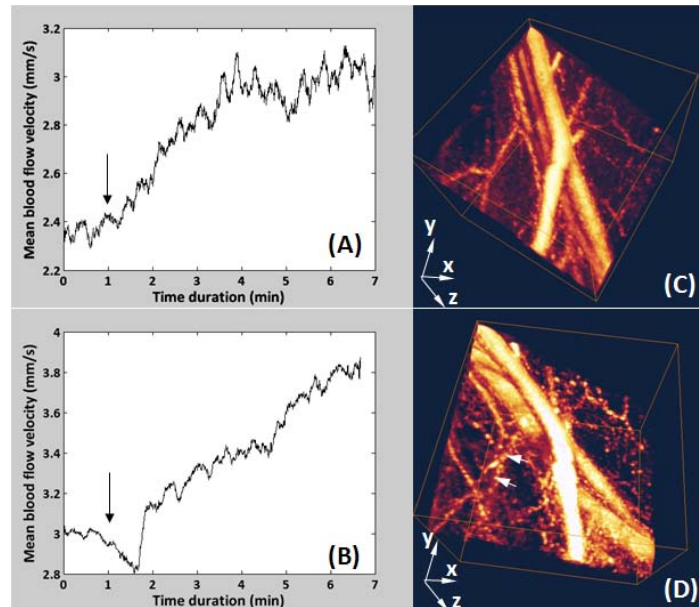
Figure 4.3 In vivo characterization of the dynamic fluctuation of blood flow velocity in the representative arterioles of both diabetic (A) and wide-type (B) mice before and after chemical stimulation. Vasodilation in vasa nevorum are also shown by comparing of 3D OMAG between baseline (C) and end point of stimulation (D) in diabetic animal.

4.1.4.3 Evaporative skin cooling effect on nerve blood flow

Control experiment in a wild-type mouse revealed that the ethanol (95% v/v) vehicle causes an immediate, transient reduction (~50%) in blood flow (**Fig. 4.3**). We tentatively ascribe this blood flow reduction to a reflex response due to excitation of cold-sensitive primary afferent neurons by evaporative cooling.

Shown in **Figs. 4.4(A) & (B)** are OMAG micro-structual image and corresponding blood flow image. Clearly seen are the saphenous nerve, artery, vein. In **Figs. 4.4 (C) & (D),** the baseline blood flow velocity and a transient reduction are seen from vessel A and B, respectively, indicated by arrows in **Fig. 4.4 (B)** following cutaneous administration of ethanol (at the time marked by the vertical arrow); **Figs. 4.4 (E) & (F)** are superior views of 3D blood flow image collected from baseline and after 15-min data collection. The blue arrows point to the blood vessels that comprise the vasa nervorum of the saphenouse nerve which runs more or less parallel to the main artery and vein.
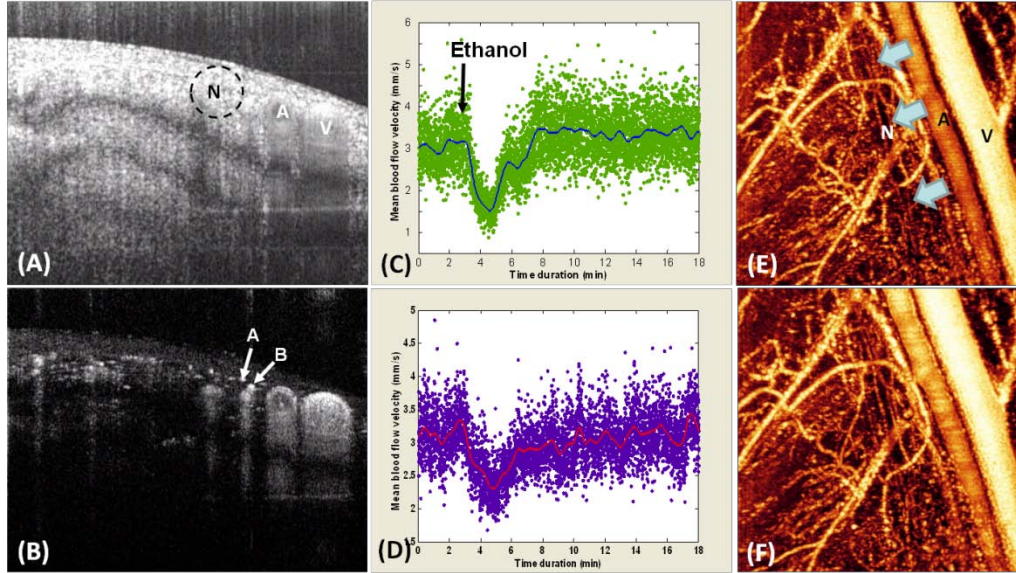
Figure 4.4 Transient reduction in blood flow evoked by topical application of ethanol to the skin. (A) OMAG micro-structual image. Clearly seen are the saphenous nerve (N), artery (A), vein (V); (B) corresponding blood flow image; (C)&(D) Baseline blood flow velocity and a transient reduction seen from vessel A and B, respectively, indicated by arrows in (B) following cutaneous administration of ethanol (at the time marked by the vertical arrow); (E)&(F) are superior views of 3D blood flow image collected from baseline and after 15-min data collection. The blue arrows point to the blood vessels that comprise the vasa nervorum of the saphenouse nerve which runs more or less parallel to the main artery (A) and vein (V).

4.1.5 Discussion

Our study showed that OMAG has the ability to visualize the 3D structure of blood vessels in vivo and quantify blood flow in these blood vessels in a tissue volume of 2.5 mm by 2.5mm wide and up to 1.5 mm deep below the tissue surface. Axial resolution for resolving flow dimension in OMAG is determined by the bandwidth of the light source used (1310 nm). For the OMAG system employed in the present study the theoretical resolution was ~8 μm within the biological tissue (12 μm in air). Because capillaries in the vasa nervorum have a somewhat larger size than the typical capillary diameter of elsewhere in the body [145] this means that OMAG has the unique ability to image the 3-D structure of the vasa nervorum in its natural state in vivo with a resolution approaching or equal to the capillary level while simultaneously measuring (in absolute

units) the blood flows within the individual microvessels. By using OMAG we were able to demonstrate that perfusion of hindlimb blood vessels, including those of the saphenous nerve vasa nervorum, can be increased by sensory irritants applied to the skin.

OMAG can quantify blood flow within tissue non-invasively. OMAG produces imaging contrast via endogenous light scattering from moving particles (e.g., flowing blood cells within open vessels), thus no exogenous contrast agents are necessary. OMAG is a real-time method capable of resolving 3-D distribution of dynamic blood perfusion within the microcirculatory tissue beds at a high spatial (<10 μm) and temporal (0.1 s) resolution. The detailed functional architecture of the perfused microvascular network can be revealed and the volumetric rheology and perfusion status of a nerve and the surrounding tissue quantified in its native state. The present study using OMAG provided unprecedented information regarding blood flows in the hindleg of the mouse, including individual microvessels belonging to the vasa nervorum.

In this present study, interestingly, in the mouse cutaneous application of menthol it caused a prolonged increase in perfusion of nearby tissue, sometimes preceded by a transient decrease in blood flow. This transient blood flow decrease resembled that evoked by the ethanol vehicle applied alone. We tentatively ascribe the initial reduction in blood flow to a reflex vasoconstriction initiated by excitation of cold-sensitive primary afferent neurons by evaporative cooling of skin. The subsequent increase in the blood flows above baseline presumably was due to activation by the sensory irritants of either an axon reflex [146] or a dorsal root reflex mechanism [147]. Because we did not monitor systemic blood pressure we cannot exclude the possibility that the increases in the blood flows were secondary to an increase in blood pressure in response to cutaneous nociceptor stimulation by menthol. The immediate facilitation of microcirculation by menthol (Fig.3) is puzzling because menthol needs time to diffuse through the skin. In human skin there is a delay before topical application of menthol excites C fibers [148]. It is possible that menthol solution or vapor gained access to nerve fibers or blood vessels without much delay by entering through the skin window and avoiding a major diffusion barrier.

In this pilot study we demonstrated the feasibility of using OMAG for measuring blood flow in hindlimb vasa nervorum in the mouse. We illustrated measurements performed in both wild-type and Type 1 diabetic (Ins2Akita/+) mice. It should therefore be possible to apply OMAG to the problem of diabetic peripheral neuropathy. Diabetic neuropathy [149] is a common disorder involving a large proportion of diabetic patients, yet its pathophysiology is controversial [147]. Despite many studies, the issue of microvascular contribution to diabetic sensory neuropathy remains unresolved. Measurements of nerve blood flow in both experimental and clinical diabetic neuropathy yielded divergent results (some authors report early reduction in nerve blood flow, while others find no change or an increase). Technical differences in the preparations and flawed methodology most likely contributed to the discrepant results [150]. Studies of nerve perfusion are challenging because nerve blood perfusion is provided by a complex longitudinal network of the peri-, epi- and endoneurial blood vessels and their anastomoses [151]. The ability of OMAG to simultaneously visualize and measure blood flows in individual microvessels should prove a major advantage over the traditional methods for nerve blood flow measurement.

4.1.6 Conclusion

In summary, we have successfully demonstrated the use of OMAG for *in vivo* 3D view of microcirculation within vasa nervorum in peripheral nerve. By regulating the flow of blood in the nerve, we also demonstrated OMAG is able to directly examining the dynamic circulatory parameters. In the future, a simple combination of OMAG and neurophysiological methods should permit evaluation of the degree to which is dependent on the circulation in the nerve and enables determination of the effects of vascular-related pharmacological inventions on DPN.

Chapter 5

Conclusions

5.1 Summary

The main purpose of this thesis is to assess OMAG for imaging 3D blood flow within microcirculatory tissue beds in vivo, so that this may be accepted as a standard imaging modality for preclinical study on vascular diseases. Thus, in this work we established four animal models which closely mimics cerebral and peripheral pathological conditions observed in humans. We evaluated the utility of OMAG imaging and quantifying of blood perfusion within microcirculatory tissue beds in vivo and then we assessed the feasibility of OMAG for differentiating the vascular responses between vehicle and treated animals or between healthy and diseased animals, in an attempt to facilitate the application of OMAG on evaluating therapeutic effects.

To be specific, we firstly introduced the basic knowledge of cerebral and peripheral blood flow, described the close relationships between these blood flow and the tissues they perfused, and presented the important vascular diseases due to their aberrations and describe the possible strategies for their restoration.

We provided an overview of the vascular imaging methods for preclinical purpose and then introduced the system used in this study, OMAG. We described the basic principles of OMAG and reported its validation results for quantification of blood flow in vitro or in vivo. We also briefly described the recent generations of OMAG: DOMAG and UHS-OMAG.

We detailed three cerebral experiments using OMAG and quantification methods developed. In trauma experiment, we demonstrated OMAG can monitor in vivo post-traumatic revascularization and evaluate agents that promote this process by quantifying

the restored blood volume in injury site. In stroke experiment, we demonstrated OMAG can in vivo evaluate the vascular response during intra-ischemic period by visualizing and quantifying residual blood volume and real time track neovascularization in the post-ischemic period by longitudinally imaging and measuring vessel density. In meningeal thrombosis experiment, we found UHS-OMAG method is able to dynamically visualize meningeal microcirculation decoupled from the cortical blood flow and chronically measure blood velocity, vessel diameter, flow rate and blood volume during thrombotic event. Then we examined OMAG in one peripheral experiment. OMAG was utilized to characterize blood perfusion of peripheral nerve in diabetic mice. The results indicate the potential of OMAG for assessing the blood supply of nerve involved in the pathology and evaluating the treatment of peripheral diabetic neuropathy.

Therefore, the major contribution of this work are (1) the establishment of experimental ground work for applying OMAG in the animal models studied and corresponding biological tissues, (2) the discovery of the characteristics of vascular development in animal models explored and the effects of interested agents which promote tissue perfusion restoration.

5.2 Future work

In our preliminary work, the ultra-high sensitive OMAG was tested to image meningeal microvessels in mice [78]. The UHS-OMAG is the most recently developed OMAG imaging technique that has improved flow sensitivity (~4 microns per second) to blood flow. With such high sensitivity to the blood flow, UHS-OMAG is capable of imaging the slow circulations, particularly those from capillary blood vessels. More important, because cerebral blood flow under pathophysiologic conditions is sometimes very slow, it would be beneficial to systematically test whether UHS-OMAG is useful in imaging the cerebral blood flow responses to local injuries presented in the current cerebral disease models, such as trauma and stroke.

Although UHS-OMAG is good for detecting the blood cell movements within capillary vessels, the size of capillary is about 5-8 microns in average. However, the axial imaging resolution of our current system was ~10 microns. This leads to a blurred appearance of the capillaries that are imaged by the system. Therefore, a useful effort should be paid to increase the system axial imaging resolution, so that the capillary vessels are imaged with increased accuracy. In this way, we would be able to provide more precise quantitative information as to how capillary beds respond to the local injuries. The limited axial resolution was determined by the light source used in the system, which typically has a bandwidth of 60 nm. To increase the axial resolution, a light source with a spectral bandwidth wider than 60 nm would be needed. Recently, supercontinuum light source has been reported to have a spectral bandwidth of more than 200 nm. If this light source can be employed to illuminate our OMAG system, then the axial resolution can be improved to ~ 2 microns, sufficient to provide a sharp image of capillary blood flow within tissue beds. Consequently, it would be worthwhile to explore the use of supercontinuum light source in the OMAG imaging system in order to visualize healing-associated neovascularization with more comprehensive details in trauma and stroke models.

Perhaps the most exciting and challenging prospects for OMAG is associated with mapping the oxygenation status of blood perfusion by combining with spectroscopic technique, which relies on the different molar extinction coefficients between the oxygenated and de- oxygenated hemoglobin in the near-infrared region at 800 nm wavelength band [152]. To this end, our group is currently working on constructing a functional spectroscopic OMAG to image oxygen saturation in blood vessels. This instrument is intended to be utilized in trauma and stroke models for providing the simultaneous, quantitative assessment of cerebral perfusion and oxygen consumption within a scanned tissue volume non-invasively and without the use of labeling techniques.

Another further improvement in OMAG to be anticipated is its imaging speed, considering its application on drug discovery. Although this work demonstrated OMAG non-invasive imaging cerebral perfusion in stroke model over an extended period of time,

unfortunately it performed only at a few time points during this period. We still envision using super speed camera to increase the temporal resolution of OMAG in hopes of further enhancing its automated imaging speed. If this critical issue is resolved, we could explore in real time the effects of stroke-limiting treatments, such as tissue-type plasminogen activator (tPA), which is an approved treatment by FDA [153]. Real-time imaging may allow us to control the experiment more precisely and provides us with more reliable information as to the evaluation of the efficacy of the treatments.

In addition to the advances that are being made in OMAG technique for investigating abnormal cerebral perfusion, we also need to optimize the animal models used in this work for future robust application in preclinical studies. For example, the trauma model we used in this work is a penetrating brain injury model for easy handling and rapid localizing new vessels. Another type of injury commonly used in literature is closed brain injury with diffuse effect [154]. By comparing OMAG's performance in traumatic brain injury with different features, we can limit or extend its applications in the field of trauma.

References

[1] N. Ferrara, "Role of vascular endothelial growth factor in the regulation of angiogenesis," Kidney Int 56(3), 794-814 (1999)

[2] E. Ruoslahti, "Targeting tumor vasculature with homing peptides from phage display," Seminars in Cancer Biology 10(6), 435-442 (2000)

[3] N. A. Lassen, "Normal average value of CBF in young adults is 50 ml 100 g^{-1} min^{-1} " J Cereb Blood Flow Metab 5(1), 347-349 (1985)

[4] T. J. Sick, M. Rosenthal, J. C. LaManna and P. L. Lutz, "Brain potassium ion homeostasis, anoxia, and metabolic inhibition in turtles and rats," Am J Physiol 243(3), R281-288 (1982)

[5] E. Hamel, "Perivascular nerves and the regulation of cerebrovascular tone," J. Appl. Physiol. 100(3), 1059-1064 (2006)

[6] S. L. Harper, H. G. Bohlen and M. J. Rubin, "Arterial and microvascular contributions to cerebral cortical autoregulation in rats," Am J Physiol 246(1), H17-24 (1984)

[7] W. Kuschinsky and M. Wahl, "Local chemical and neurogenic regulation of cerebral vascular resistance," Physiol. Rev. 58(3), 656-689 (1978)

[8] J. E. Brian Jr, F. M. Faraci and D. D. Heistad, "Recent insights into the regulation of cerebral circulation," Clin. Exp. Pharmacol Physiol. 23(6-7), 449-457 (1996)

[9] B. John, Jr. and W. A. Hauser, "The Epidemiology of Traumatic Brain Injury: A Review," Epilepsia 44(s10), 2-10 (2003)

[10] J. Nortje and D. K. Menon, "Traumatic brain injury: physiology, mechanisms, and outcome," Curr. Opin. Neurol. 17(6), 711-718 (2004)

[11] C. Werner and K. Engelhard, "Pathophysiology of traumatic brain injury," Br. J. Anaesth. 99(1), 4-9 (2007)

[12] H. M. Bramlett and W. D. Dietrich, "Pathophysiology of cerebral ischemia and brain trauma[colon] Similarities and differences," J Cereb Blood Flow Metab 24(2), 133-150 (2004)

[13] A. Rodríguez-Baeza, F. Reina-de la Torre, A. Poca, M. Martí and A. Garnacho, "Morphological features in human cortical brain microvessels after head injury: A three-dimensional and immunocytochemical study," Anat Rec Part A 273A(1), 583-593 (2003)

[14] D. S. DeWitt and D. S. Prough, "Traumatic Cerebral Vascular Injury: The Effects of Concussive Brain Injury on the Cerebral Vasculature," J Neurotrauma 20(9), 795-825 (2003)

[15] J. r. Overgaard and W. A. Tweed, "Cerebral circulation after head injury," J Neurosurg 41(5), 531-541 (1974)

[16] Y. Inoue, T. Shiozaki, O. Tasaki, T. Hayakata, H. Ikegawa, K. Yoshiya, T. Fujinaka, H. Tanaka, T. Shimazu and H. Sugimoto, "Changes in Cerebral Blood Flow from the Acute to the Chronic Phase of Severe Head Injury," J Neurotrauma 22(12), 1411-1418 (2005)

[17] J. P. Coles, T. D. Fryer, P. Smielewski, D. A. Chatfield, L. A. Steiner, A. J. Johnston, S. P. M. J. Downey, G. B. Williams, F. Aigbirhio, P. J. Hutchinson, K. Rice, T. A. Carpenter, J. C. Clark, J. D. Pickard and D. K. Menon, "Incidence and Mechanisms of Cerebral Ischemia in Early Clinical Head Injury," J Cereb Blood Flow Metab 24(2), 202-211 (2004)

[18] C. M. Michaud, C. J. L. Murray and B. R. Bloom, "Burden of Disease--Implications for Future Research," JAMA 285(5), 535-539 (2001)

[19] J. A. Zivin, "Cerebrovascular Disease: Pathophysiology, diagnosis, and management," N Engl J Med 339(19), 1402-a-1403 (1998)

[20] A. Durukan and T. Tatlisumak, "Acute ischemic stroke: Overview of major experimental rodent models, pathophysiology, and therapy of focal cerebral ischemia," Pharmacology Biochemistry and Behavior 87(1), 179-197 (2007)

[21] U. Dirnagl, C. Iadecola and M. A. Moskowitz, "Pathobiology of ischaemic stroke: an integrated view " Trends Neurosci 22(9), 391-397 (1999)

[22] M. D. Ginsberg, "Adventures in the Pathophysiology of Brain Ischemia: Penumbra, Gene Expression, Neuroprotection: The 2002 Thomas Willis Lecture," Stroke 34(1), 214-223 (2003)

[23] G. J. Bouma and J. P. Muizelaar, "Cerebral blood flow, cerebral blood volume, and cerebrovascular reactivity after severe head injury," J. Neurotrauma 9(1), S333-S348 (1992)

[24] R. Morgan, C. W. Kreipke, G. Roberts, M. Bagchi and J. A. Rafols, "Neovascularization following traumatic brain injury: possible evidence for both angiogenesis and vasculogenesis," Neurol Res. 29(4), 375-381 (2007)

[25] M. Chopp, Z. G. Zhang and Q. Jiang, "Neurogenesis, angiogenesis, and MRI Indices of functional recovery from stroke," Stroke 38(2), 827-831 (2007)

[26] W. Risau, "Mechanisms of angiogenesis," Nature 386(6626), 671-674 (1997)

[27] P. C. Jackson, "The peripheral circulation," Wiley, New York (1978).

[28] E. M. Landis, "The Peripheral Circulation," Ann. Rev. Phys. 7(1), 201-230 (1945)

[29] J. J. Friedman, "Microcirculation," in Physiology E. E. Selkurt, Ed., Little, Brown & Company, Boston (1971).

[30] H. V. Sparks and F. L. Belloni, "The Peripheral Circulation: Local Regulation," Ann. Rev. Phys. 40(1), 67-92 (1978)

[31] B. Folkow, "Regulation of the peripheral circulation," Br. Heart J. 33(Suppl), 27-31 (1971)

[32] M. H. Laughlin , R. J. Korthuis, D. J. Duncker and R. J. Bache, "control of blood flow to cardiac and skeletal muscle during exercise," in Handbook of Physiology. Exercise: Regulation and Integration of Multiple Systems, pp. 705-769, Am. Physiol. Soc., Bethesda, MD (1996).

[33] M. H. Laughlin, R. J. Korthuis, D. J. Duncker and R. J. Bache, "control of blood flow to cardiac and skeletal muscle during exercise," in Handbook of Physiology. Exercise: Regulation and Integration of Multiple Systems, pp. 705-769, Am. Physiol. Soc., Bethesda, MD (1996).

[34] D. E. Strandness, Jr. and J. F. Eidt, "Peripheral Vascular Disease," Circulation 102(90004), IV-46-51 (2000)

[35] M. H. Criqui, A. Fronek, E. Barrett-Connor, M. R. Klauber, S. Gabriel and D. Goodman, "The prevalence of peripheral arterial disease in a defined population," Circulation 71(3), 510-515 (1985)

[36] J. W. Olin and B. A. Sealove, "Peripheral Artery Disease: Current Insight Into the Disease and Its Diagnosis and Management," Maya Clin. Proc. 85(7), 678-692 (2010)

[37] H. L. Gornik and J. A. Beckman, "Peripheral Arterial Disease," Circulation 111(13), e169-172 (2005)

[38] Y. Harati, "Diabetic Peripheral Neuropathies," Ann. Intern. Med. 107(4), 546-559 (1987)

[39] M. Tavakoli, O. Asghar, U. Alam, I. N. Petropoulos, H. Fadavi and R. A. Malik, "Review: Novel insights on diagnosis, cause and treatment of diabetic neuropathy: focus on painful diabetic neuropathy," Ther. Adv. Endocrinol. Metab 1(2), 69-88 (2010)

[40] W. Schaper and W. D. Ito, "Molecular Mechanisms of Coronary Collateral Vessel Growth," Circ. Res. 79(5), 911-919 (1996)

[41] W. D. Ito, M. Arras, D. Scholz, B. Winkler, P. Htun and W. Schaper, "Angiogenesis but not collateral growth is associated with ischemia after femoral artery occlusion," Am. J. Physiol. 273(3), H1255-1265 (1997)

[42] M. Arras, W. D. Ito, D. Scholz, B. Winkler, J. Schaper and W. Schaper, "Monocyte activation in angiogenesis and collateral growth in the rabbit hindlimb," J Clin Invest. 101(1), 40-50 (1998)

[43] I. Buschmann and W. Schaper, "Arteriogenesis Versus Angiogenesis: Two Mechanisms of Vessel Growth," News Physiol Sci 14(3), 121-125 (1999)

[44] D. J. Collinson and R. Donnelly, "Therapeutic Angiogenesis in Peripheral Arterial Disease: Can Biotechnology Produce an Effective Collateral Circulation?," European Journal of Vascular and Endovascular Surgery 28(1), 9-23 (2004)

[45] E. P. Meyer, A. Ulmann-Schuler, M. Staufenbiel and T. Krucker, "Altered morphology and 3D architecture of brain vasculature in a mouse model for Alzheimer's disease," PNAS 105(9), 3587-3592 (2008)

[46] S. Zhang, J. Boyd, K. Delaney and T. H. Murphy, "Rapid Reversible Changes in Dendritic Spine Structure In Vivo Gated by the Degree of Ischemia," J. Neurosci. 25(22), 5333-5338 (2005)

[47] P. Li and T. H. Murphy, "Two-Photon Imaging during Prolonged Middle Cerebral Artery Occlusion in Mice Reveals Recovery of Dendritic Structure after Reperfusion," J. Neurosci. 28(46), 11970-11979 (2008)

[48] E. X. Wu, H. Tang and J. H. Jensen, "Applications of ultrasmall superparamagnetic iron oxide contrast agents in the MR study of animal models," NMR in Biomedicine 17(7), 478-483 (2004)

[49] H. Moreno, F. Hua, T. Brown and S. Small, "Longitudinal mapping of mouse cerebral blood volume with MRI," NMR in Biomedicine 19(5), 535-543 (2006)

[50] J. B. Mandeville, J. J. A. Marota, B. E. Kosofsky, J. R. Keltner, R. Weissleder, B. R. Rosen and R. M. Weisskoff, "Dynamic functional imaging of relative cerebral blood volume during rat forepaw stimulation," Magnetic Resonance in Medicine 39(4), 615-624 (1998)

[51] F. Calliada, R. Campani, O. Bottinelli, A. Bozzini and M. G. Sommaruga, "Ultrasound contrast agents: Basic principles," European Journal of Radiology 27(Suppl.2), S157-S160 (1998)

[52] A. K. Dunn, H. Bolay, M. A. Moskowitz and D. A. Boas, "Dynamic Imaging of Cerebral Blood Flow Using Laser Speckle," J Cereb Blood Flow Metab 21(3), 195-201 (2001)

[53] A. N. Nielsen, M. Fabricius and M. Lauritzen, "Scanning laser-Doppler flowmetry of rat cerebral circulation during cortical spreading depression," J. Vasc. Res. 37(1), 513-522 (2000)

[54] K. Wardell, A. Jakobsson and G. E. Nilsson, "Laser Doppler perfusion imaging by dynamic light scattering," Biomedical Engineering, IEEE Transactions on 40(4), 309-316 (1993)

[55] A. Limbourg, T. Korff, L. C. Napp, W. Schaper, H. Drexler and F. P. Limbourg, "Evaluation of postnatal arteriogenesis and angiogenesis in a mouse model of hind-limb ischemia," Nat. Protocols 4(12), 1737-1748 (2009)

[56] H. F. Zhang, K. Maslov, G. Stoica and L. V. Wang, "Functional photoacoustic microscopy for high-resolution and noninvasive in vivo imaging," Nat Biotech 24(7), 848-851 (2006)

[57] O. Sakurada, C. Kennedy, J. Jehle, J. D. Brown, G. L. Carbin and L. Sokoloff, "Measurement of local cerebral blood flow with iodo [14C] antipyrine," Am J Physiol Heart Circ Physiol 234(1), H59-66 (1978)

[58] P. H. Tomlins and R. K. Wang, "Theory, development and applications of optical coherence tomography," J Phys. D: Appl. Phys. 38(2519-2535 (2005)

[59] D. Huang, E. A. Swanson, C. P. Lin, J. S. Schuman, W. G. Stinson, W. Chang, M. R. Hee, T. Flotte, K. Gregory, C. A. Puliafito and a. et, "Optical coherence tomography," Science 254(5035), 1178-1181 (1991)

[60] A. F. Fercher, W. Drexler, C. K. Hitzenberger and T. Lasser, "Optical Coherence Tomography - Principles and Applications," Rep Prog Phys 66(239-303 (2003)

[61] J. M. Schmitt, "Optical coherence tomography (OCT): a review," Selected Topics in Quantum Electronics, IEEE Journal of 5(4), 1205-1215 (1999)

[62] Z. Chen, Y. Zhao, S. Srinivas, J. Nelson, N. Prakash and R. Frostig, "Optical Doppler tomography," Selected Topics in Quantum Electronics, IEEE Journal of 5(4), 1134-1142 (1999)

[63] R. K. Wang, S. L. Jacques, Z. Ma, S. Hurst, S. Hanson and A. Gruber, "Three dimensional optical angiography," Opt Express 15(4083-4097 (2007)

[64] Z. Chen, T. E. Milner, S. Srinivas, X. Wang, A. Malekafzali, M. J. C. van Gemert and J. S. Nelson, "Noninvasive imaging of in vivo blood flow velocity using optical Doppler tomography," Opt. Lett. 22(14), 1119-1121 (1997)

[65] J. A. Izatt, M. D. Kulkarni, S. Yazdanfar, J. K. Barton and A. J. Welch, "In vivo bidirectional color Doppler flow imaging of picoliter blood volumes using optical coherence tomography," Opt. Lett. 22(18), 1439-1441 (1997)

[66] Y. Zhao, Z. Chen, C. Saxer, S. Xiang, J. F. de Boer and J. S. Nelson, "Phase-resolved optical coherence tomography and optical Doppler tomography for imaging blood flow in human skin with fast scanning speed and high velocity sensitivity," Opt. Lett. 25(2), 114-116 (2000)

[67] Y. H. Zhao, Z. P. Chen, Z. H. Ding, H. Ren and J. S. Nelson, "Real-time phase-resolved functional optical coherence tomography by use of optical Hilbert transformation," Opt Lett 27(98-100 (2002)

[68] H. Ren, Z. Ding, Y. Zhao, J. Miao, J. S. Nelson and Z. Chen, "Phase-resolved functional optical coherence tomography: simultaneous imaging of in situ tissue structure, blood flow velocity, standard deviation, birefringence, and Stokes vectors in human skin," Opt. Lett. 27(19), 1702-1704 (2002)

[69] R. Leitgeb, L. Schmetterer, W. Drexler, A. Fercher, R. Zawadzki and T. Bajraszewski, "Real-time assessment of retinal blood flow with ultrafast acquisition by color Doppler Fourier domain optical coherence tomography," Opt. Express 11(23), 3116-3121 (2003)

[70] J. Zhang and Z. Chen, "In vivo blood flow imaging by a swept laser source based Fourier domain optical Doppler tomography," Opt. Express 13(19), 7449-7457 (2005)

[71] B. Vakoc, S. Yun, J. de Boer, G. Tearney and B. Bouma, "Phase-resolved optical frequency domain imaging," Opt. Express 13(14), 5483-5493 (2005)

[72] R. A. Leitgeb, L. Schmetterer, C. K. Hitzenberger, A. F. Fercher, F. Berisha, M. Wojtkowski and T. Bajraszewski, "Real-time measurement of in vitro flow by Fourier-domain color Doppler optical coherence tomography," Opt. Lett. 29(2), 171-173 (2004)

[73] B. White, M. Pierce, N. Nassif, B. Cense, B. Park, G. Tearney, B. Bouma, T. Chen and J. de Boer, "In vivo dynamic human retinal blood flow imaging using ultra-high-speed spectral domain optical coherence tomography," Opt. Express 11(25), 3490-3497 (2003)

[74] R. K. Wang and L. An, "Doppler optical micro-angiography for volumetric imaging of vascular perfusion in vivo," Opt. Express 17(11), 8926-8940 (2009)

[75] R. K. Wang, "In vivo full range complex Fourier domain optical coherence tomography," Appl. Phys. Lett. 90(5), 054103 (2007)

[76] L. An and R. K. Wang, "Use of a scanner to modulate spatial interferograms for in vivo full-range Fourier-domain optical coherence tomography," Opt. Lett. 32(23), 3423-3425 (2007)

[77] L. An, J. Qin and R. K. Wang, "Ultrahigh sensitive optical microangiography for in vivo imaging of microcirculations within human skin tissue beds," Opt. Express 18(8), 8220-8228 (2010)

[78] Y. Jia, L. An and R. K. Wang, "Label-free and highly sensitive optical imaging of detailed microcirculation within meninges and cortex in mice with the cranium left intact," J Biomed. Opt. 15(3), 030510-030513 (2010)

[79] W. Zhang, J. J. Iliff, C. J. Campbell, R. K. Wang, P. D. Hurn and N. J. Alkayed, "Role of soluble epoxide hydrolase in the sex-specific vascular response to cerebral ischemia," J Cereb Blood Flow Metab 29(8), 1475-1481 (2009)

[80] B. K. Siesjo, Brain Energy Metabolism, Wiley, New York (1978).

[81] P. T. Fox and M. E. Raichle, "Focal physiological uncoupling of cerebral blood flow and oxidative metabolism during somatosensory stimulation in human subjects," PNAS 83(4), 1140-1144 (1986)

[82] D. M. McDonald and P. L. Choyke, "Imaging of angiogenesis: from microscope to clinic," Nat Med 9(6), 713-725 (2003)

[83] P. Carmeliet, "The development of blood vessels," in Assembly of the Vasculature and Its Regulation R. J. Tomanek, Ed., pp. 1-20, Berlin: Birkhäuser (2002).

[84] F. Arnold and D. C. West, "Angiogenesis in wound healing," Pharmacol Ther 52(3), 407-422 (1991)

[85] S. Patan, L. L. Munn, S. Tanda, S. Roberge, R. K. Jain and R. C. Jones, "Vascular Morphogenesis and Remodeling in a Model of Tissue Repair: Blood Vessel Formation and Growth in the Ovarian Pedicle After Ovariectomy," Circ. Res. 89(8), 723-731 (2001)

[86] R. K. Clark, E. V. Lee, C. J. Fish, R. F. White, W. J. Price, Z. L. Jonak, G. Z. Feuerstein and F. C. Barone, "Development of tissue damage, inflammation and

resolution following stroke: An immunohistochemical and quantitative planimetric study," Brain Research Bulletin 31(5), 565-572 (1993)

[87] J. Folkman, "Therapeutic Angiogenesis in Ischemic Limbs," Circulation 97(12), 1108-1110 (1998)

[88] J. Krupinski, J. Kaluza, P. Kumar, S. Kumar and J. M. Wang, "Role of angiogenesis in patients with cerebral ischemic stroke," Stroke 25(9), 1794-1798 (1994)

[89] M. Frontczak-Baniewicz and M. Walski, "New vessel formation after surgical brain injury in rat's cerebral cortex. Formation of the blood vessels proximally to the surgical injury," Acta Neurobiol Exp 63(65-75 (2003)

[90] R. Morgan, C. W. Kreipke, G. Roberts, M. Bagchi and J. A. Rafols, "Neovascularization following traumatic brain injury: possible evidence for both angiogenesis and vasculogenesis," Neurol Res 29(375-381 (2007)

[91] E. F. Ellis, R. J. Police, L. Yancey, J. S. McKinney and S. C. Amruthesh, "Dilation of cerebral arterioles by cytochrome P-450 metabolites of arachidonic acid," Am J Physiol 259(4), H1171-1177 (1990)

[92] C. Zhang and D. R. Harder, "Cerebral Capillary Endothelial Cell Mitogenesis and Morphogenesis Induced by Astrocytic Epoxyeicosatrienoic Acid," Stroke 33(12), 2957-2964 (2002)

[93] J. J. Iliff and N. J. Alkayed, "Soluble epoxide hydrolase inhibition: targeting multiple mechanisms of ischemic brain injury with a single agent," Future Neurol 4(2), 179-199 (2009)

[94] C. Morisseau and B. D. Hammock, "Epoxide hydrolases: Mechanisms, Inhibitor Designs, and Biological Roles," Annu Rev Pharmacol Toxicol 45(1), 311-333 (2005)

[95] W. Zhang, T. Otsuka, N. Sugo, A. Ardeshiri, Y. K. Alhadid, J. J. Iliff, A. E. DeBarber, D. R. Koop and N. J. Alkayed, "Soluble Epoxide Hydrolase Gene Deletion Is Protective Against Experimental Cerebral Ischemia," Stroke 39(7), 2073-2078 (2008)

[96] R. K. Wang and S. Hurst, "Mapping of cerebrovascular blood perfusion in mice with skin and cranium intact by Optical Micro-AngioGraphy at 1300nm wavelength," Opt Express 15(18), 11402-11412 (2007)

[97] L. Fina, H. V. Molgaard, D. Robertson, N. J. Bradley, P. Monaghan, D. Delia, D. R. Sutherland, M. A. Baker and M. F. Greaves, "Expression of the CD34 gene in vascular endothelial cells," Blood 75(12), 2417-2426 (1990)

[98] G. Mazur, T. Wrobel, P. Dziegiel, M. Jelen, K. Kuliczkowski and M. Zabel, "Angiogenesis measured by expression of CD34 antigen in lymph nodes of patients with non-Hodgkin's lymphoma," Folia Histochem Cytobiol 42(241-243 (2004)

[99] L. Schaerer, M. H. Schmid, B. Mueller, R. G. Dummer, G. Burg and W. Kempf, "Angiogenesis in Cutaneous Lymphoproliferative Disorders: Microvessel Density Discriminates Between Cutaneous B-Cell Lymphomas and B-Cell Pseudolymphomas," Am J Dermatopathol 22(2), 140-143 (2000)

[100] J. D. Briers, "Laser Doppler, speckle and related techniques for blood perfusion mapping and imaging," Physiol Meas 22(R35-66 (2001)

[101] P. Carmeliet, "Blood vessels and nerves: common signals, pathways and diseases," Nat Rev Genet 4(9), 710-720 (2003)

[102] C. Leventhal, S. Rafii, D. Rafii, A. Shahar and S. A. Goldman, "Endothelial Trophic Support of Neuronal Production and Recruitment from the Adult Mammalian Subependyma," Mol Cell Neurosci 13(6), 450-464 (1999)

[103] T. D. Palmer, A. R. Willhoite and F. H. Gage, "Vascular niche for adult hippocampal neurogenesis," J Comp Neurol 425(4), 479-494 (2000)

[104] H. H. Lipowsky, "Microvascular Rheology and Hemodynamics," Microcirculation 12(1), 5 - 15 (2005)

[105] J. H. Garcia, N. A. Lassen, C. Weiller, B. Sperling and J. Nakagawara, "Ischemic Stroke and Incomplete Infarction," Stroke 27(4), 761-765 (1996)

[106] J. Krupinski, J. Kaluza, P. Kumar, M. Wang and S. Kumar, "Prognostic value of blood vessel density in ischaemic stroke," Lancet 342(742 (1993)

[107] Z. G. Zhang, L. Zhang, Q. Jiang, R. Zhang, K. Davies, C. Powers, N. v. Bruggen and M. Chopp, "VEGF enhances angiogenesis and promotes blood-brain barrier leakage in the ischemic brain," J Clin Invest 106(7), 829-838 (2000)

[108] M. Chopp, Y. Li and J. Zhang, "Plasticity and remodeling of brain," J Neurol Sci. 265(1-2), 97-101 (2008)

[109] N. J. Alkayed, I. Harukuni, A. S. Kimes, E. D. London, R. J. Traystman and P. D. Hurn, "Gender-linked brain injury in experimental stroke," Stroke 29(159-165 (1998)

[110] U. Dirnagl, B. Kaplan, M. Jacewicz and W. Pulsinelli, "Continuous measurement of cerebral cortical blood flow by laser-Doppler flowmetry in a rat stroke model," J Cereb Blood Flow Metab 9(589-596 (1989)

[111] L. Zhang, R. L. Zhang, Y. Wang, C. Zhang, Z. G. Zhang, H. Meng and M. Chopp, "Functional Recovery in Aged and Young Rats After Embolic Stroke: Treatment With a Phosphodiesterase Type 5 Inhibitor," Stroke 36(4), 847-852 (2005)

[112] Y. Sun, K. Jin, L. Xie, J. Childs, X. O. Mao, A. Logvinova and D. A. Greenberg, "VEGF-induced neuroprotection, neurogenesis, and angiogenesis after focal cerebral ischemia," J Clin Invest 111(12), 1843-1851 (2003)

[113] H. Athiraman, Q. Jiang, G. L. Ding, L. Zhang, Z. G. Zhang, L. Wang, A. S. Arbab, Q. Li, S. Panda, K. Ledbetter, A. M. Rad and M. Chopp, "Investigation of relationships between transverse relaxation rate, diffusion coefficient, and labeled cell concentration in ischemic rat brain using MRI," Magn Reson Med 61(3), 587-594 (2009)

[114] M. Liu, P. D. Hurn and N. J. Alkayed, "Cytochrome P450 in neurological disease," Curr Drug Metab 5(225-234 (2004)

[115] D. H. Munzenmaier and D. R. Harder, "Cerebral microvascular endothelial cell tube formation: role of astrocytic epoxyeicosatrienoic acid release," Am J Physiol Heart Circ Physiol 278(4), H1163-1167 (2000)

[116] W. Zhang, I. P. Koerner, R. Noppens, M. Grafe, H.-J. Tsai, C. Morisseau, A. Luria, B. D. Hammock, J. R. Falck and N. J. Alkayed, "Soluble epoxide hydrolase: a novel therapeutic target in stroke," J Cereb Blood Flow Metab 27(12), 1931-1940 (2007)

[117] A. C. Webler, U. R. Michaelis, R. Popp, E. Barbosa-Sicard, A. Murugan, J. R. Falck, B. Fisslthaler and I. Fleming, "Epoxyeicosatrienoic acids are part of the VEGF-activated signaling cascade leading to angiogenesis," Am J Physiol Cell Physiol 295(5), C1292-1301 (2008)

[118] W. C. Aird, J. M. Edelberg, H. Weiler-Guettler, W. W. Simmons, T. W. Smith and R. D. Rosenberg, "Vascular bed-specific expression of an endothelial cell gene is programmed by the tissue microenvironment," J Cell Biol 138(5), 1117-1124 (1997)

[119] Q. Jiang, Z. G. Zhang, G. L. Ding, L. Zhang, J. R. Ewing, L. Wang, R. Zhang, L. Li, M. Lu, H. Meng, A. S. Arbab, J. Hu, Q. J. Li, S. Pourabdollah Nejad D, H. Athiraman and M. Chopp, "Investigation of neural progenitor cell induced angiogenesis after embolic stroke in rat using MRI," NeuroImage 28(3), 698-707 (2005)

[120] P. S. Manoonkitiwongsa, C. Jackson-Friedman, P. J. McMillan, R. L. Schultz and P. D. Lyden, "Angiogenesis After Stroke Is Correlated With Increased Numbers of Macrophages[colon] The Clean-up Hypothesis," J Cereb Blood Flow Metab 21(10), 1223-1231 (2001)

[121] L. Wei, J. P. Erinjeri, C. M. Rovainen and T. A. Woolsey, "Collateral Growth and Angiogenesis Around Cortical Stroke," Stroke 32(9), 2179-2184 (2001)

[122] G. F. Rowbotham and E. Little, "Circulations of the cerebral hemispheres," Brit J Surg 52(1), 8-21 (1965)

[123] C. W. Kerber and T. H. Newton, "The macro and microvasculature of the dura mater," Neuroradiology 6(4), 175-179 (1973)

[124] J. Roland, C. Bernard, S. Bracard, A. Czorny, J. Floquet, J. M. Race, P. Forlodou and L. Picard, "Microvascularization of the intracranial dura mater," Surg Radiol Anat 9(1), 43-49 (1987)

[125] G. F. Rowbotham and E. Little, "New concepts on the etiology and vascularization of meningioma; the mechanisms of migraine; the chemical processes of the cerebrospinal fluid; and the formation of collections of blood or fluid in the subdural space," Brit J Surg 52(21-24 (1965)

[126] A. Lindner, K. Reiners and K. V. Toyka, "Meningeal Hyperperfusion Visualized by MRI in a Patient With Visual Hallucinations and Migraine," Headache: The Journal of Head and Face Pain 36(1), 53-57 (1996)

[127] H. Bolay, U. Reuter, A. K. Dunn, Z. Huang, D. A. Boas and M. A. Moskowitz, "Intrinsic brain activity triggers trigeminal meningeal afferents in a migraine model," Nat Med 8(136–142 (2002)

[128] I. Bartholomaus, N. Kawakami, F. Odoardi, S. C., D. Miljkovic, J. W. Ellwart, W. E. F. Klinkert, C. Flugel-Koch, T. B. Issekutz, H. Wekerle and A. Flugel, "Effector T cell interactions with meningeal vascular structures in nascent autoimmune CNS lesions," Nature 462(94-98 (2009)

[129] T. Misgeld and M. Kerschensteiner, "In vivo imaging of the diseased nervous system," Nat Rev Neurosci 7(6), 449-463 (2006)

[130] Y. Jia, N. Alkayed and R. K. Wang, "Potential of optical microangiography to monitor cerebral blood perfusion and vascular plasticity following traumatic brain injury in mice in vivo," J Biomed Opt 14(4), 040505-040503 (2009)

[131] R. K. Wang, "Directional blood flow imaging in volumetric optical microangiography achieved by digital frequency modulation," Opt. Lett. 33(16), 1878-1880 (2008)

[132] R. K. Wang, "Optical Microangiography: A Label Free 3D Imaging Technology to Visualize and Quantify Blood Circulations within Tissue Beds in vivo. ," IEEE J Sel Topics Quantum Electron 16(545-554 (2010)

[133] R. K. Wang, L. An, P. Francis and D. J. Wilson, "Depth-resolved imaging of capillary networks in retina and choroid using ultrahigh sensitive optical microangiography," Opt. Lett. 35(9), 1467-1469 (2010)

[134] X. Wang and L. Xu, "An optimized murine model of ferric chloride-induced arterial thrombosis for thrombosis research," Thromb. Res. 115(1-2), 95-100 (2005)

[135] M. Nagai, C. E. Yilmaz, D. Kirchhofer, C. T. Esmon, N. Mackman and D. N. Granger, "Role of Coagulation Factors in Cerebral Venous Sinus and Cerebral Microvascular Thrombosis," Neurosurgery 66(3), 560-566 (2010)

[136] J. Partanen, L. Niskanen, J. Lehtinen, E. Mervaala, O. Siitonen and M. Uusitupa, "Natural history of peripheral neuropathy in patients with non-insulindependent diabetes mellitus," N Engl J Med. 333(2), 89-94 (1995)

[137] G. E. Reiber, E. J. Boyko and D. G. Smith, "Lower extremity foot ulcers and amputations in diabetes," in Diabetes in America M. I. Harris, C. C. Cowie, M. P. Stern, E. J. Boyko, G. E. Reiber and P. H. Bennett, Eds., pp. 409-427, National Institute of Diabetes and Digestive and Kidney Diseases, Washington, DC (1995).

[138] Z. Simmons and E. L. Feldman, "Update on diabetic neuropathy," Curr Opin Neurol. 15(5), 595-603 (2002)

[139] K. F. Kusano, K. L. Allendoerfer, W. Munger, R. Pola, M. Bosch-Marce, R. Kirchmair, Y.-s. Yoon, C. Curry, M. Silver, M. Kearney, T. Asahara and D. W. Losordo, "Sonic Hedgehog Induces Arteriogenesis in Diabetic Vasa Nervorum and Restores

Function in Diabetic Neuropathy," Arterioscler Thromb Vasc Biol 24(11), 2102-2107 (2004)

[140] P. Schratzberger, D. H. Walter, K. Rittig, F. H. Bahlmann, R. Pola, C. Curry, M. Silver, J. G. Krainin, D. H. Weinberg, A. H. Ropper and J. M. Isner, "Reversal of experimental diabetic neuropathy by VEGF gene transfer," J Clin Invest. 107(9), 1083-1092 (2001)

[141] I. Rundquist, Q. R. Smith, M. E. Michel, P. Ask, P. A. Oberg and S. I. Rapoport, "Sciatic nerve blood flow measured by laser Doppler flowmetry and [14C]iodoantipyrine," Am J Physiol Heart Circ Physiol 248(3), H311-317 (1985)

[142] D. W. Zochodne and P. A. Low, "Adrenergic control of nerve blood flow," Exp. Neurol. 109(3), 300-307 (1990)

[143] G. J. Biessels, A. Kamal, G. M. Ramakers, I. J. Urban, B. M. Spruijt, D. W. Erkelens and W. H. Gispen, "Place learning and hippocampal synaptic plasticity in streptozotocin-induced diabetic rats," Diabetes 45(9), 1259-1266 (1996)

[144] G. Lundborg and P. I. Branemark, "Microvascular structure and function of the peripehral nerves: vital microscopic studies of the tibial nerve in the rabbit," Adv Microcirc 1(2), 66-88 (1968)

[145] M. A. Bell and A. G. M. Weddell, "A morphometric study of intrafascicular vessels of mammalian sciatic nerve," Muscle & Nerve 7(7), 524-534 (1984)

[146] H. Hotta, A. Sato, Y. Sato and S. Uchida, "Stimulation of saphenous afferent nerve produces vasodilatation of the vasa nervorum via an axon reflex-like mechanism in the sciatic nerve of anesthetized rats," Neurosci. Res. 24(3), 305-308 (1996)

[147] D. W. Zochodne, "Diabetes mellitus and the peripheral nervous system: Manifestations and mechanisms," Muscle & Nerve 36(2), 144-166 (2007)

[148] N. Cameron, "The etiology of neuropathy in experimental diabetes.," Br. J. Diabetes and Vascular Disease 3(1), 98-105 (2003)

[149] P. J. Dyck and P. K. Thomas, Diabetic Neuropathy, W.B. Saunders Co., Philadelphia (1999).

[150] D. W. Zochodne, "Is early diabetic neuropathy a disorder of the dorsal root ganglion? A hypothesis and critique of some current ideas on the etiology of diabetic neuropathy," J. Peripher. Nerv. Syst. 1(2), 119-130 (1996)

[151] G. Lundborg, "Ischemic nerve injury. Experimental studies on intraneural microvascular pathophysiology and nerve function in a limb subjected to temporary circulatory arrest," Scand. J. Plast. Reconstr. Surg. Suppl. 6(2), 3-113 (1970)

[152] O. Hazeki and M. Tamura, "Quantitative analysis of hemoglobin oxygenation state of rat brain in situ by near-infrared spectrophotometry," J Appl Physiol 64(2), 796-802 (1988)

[153] J. M. Wardlaw and C. P. Warlow, "Thrombolysis in acute ischemic stroke: does it work?," Stroke 23(12), 1826-1839 (1992)

[154] C. Edward Dixon, G. L. Clifton, J. W. Lighthall, A. A. Yaghmai and R. L. Hayes, "A controlled cortical impact model of traumatic brain injury in the rat," Journal of Neuroscience Methods 39(3), 253-262 (1991)

Publications

Journal papers

1. **Y.L. Jia**, and R.K. Wang, "Label-free in vivo optical imaging of functional microcirculations within meninges and cortex in mice", *Journal of Neuroscience Methods* (In press, 2010)

2. **Y.L. Jia**, M. R. Grafe, A. Gruber, N. J. Alkayed and R.K. Wang, "In vivo optical imaging of revascularization after brain trauma in mice", *Microvascular Research* (In press, 2010)

3. **Y.L. Jia**, and R.K. Wang, "Label-free 3D optical microangiography imaging of functional vasa nervorum and peripheral microvascular tree in the hind limb of diabetic mice", *Journal of Innovative Optical Health Sciences*, 3(4), 307-313 (2010)

4. **Y.L. Jia**, L. An, and R.K. Wang, "Label-free and highly sensitive optical imaging of detailed microcirculation within meninges and cortex in mice with the cranium left intact," *Journal of Biomedical Optics*, 15 (May/June), 030510 (2010). (*Results are featured in the cover of the Journal*)

5. **Y.L. Jia**, and R.K. Wang, "Optical micro-angiography images structural and functional cerebral blood perfusion in mice with cranium left intact", *Journal of Biophotonics*, 1–7 (2010) / DOI 10.1002/jbio.201000001

6. **Y.L. Jia**, L. An, and R.K. Wang, "Doppler optical micro-angiography improves the quantification of local fluid flow and shear stress within 3D porous constructs", *Journal of Biomedical Optics (Letters)*, 14, 050504 (2009)

7. **Y.L. Jia**, N.J. Alkayed, R.K. Wang, "The potential of optical micro-angiography to monitor cerebral blood perfusion and vascular plasticity following traumatic brain injury in mice in vivo", *Journal of Biomedical Optics (Letters)*, 14, 040505 (2009)

8. **Y.L. Jia** , P. Bagnaninchi , Y. Yang , A. El Haj , M. Hinds , S. Kirkpatrick , R.K. Wang, "Doppler optical coherence tomography imaging of local fluid flow and shear

stress within microporous scaffolds", *Journal of Biomedical Optics*, 14(3), 034014 (2009)

Book Chapters

1. L An, **Y.L. Jia**, and R.K. Wang, "Label-free optical micro-angiography for functional imaging of microcirculations within tissue beds in vivo". Chapter 15 in *Handbook of Photonics for Biomedical Science*. Edited by V Tuchin, Taylor & Francis Publisher,301-325 (2010)

Conference Papers

1. Y. Yang, A. Iftimia, **Y.L. Jia**, "The study of effects of pore architecture in chitosan scaffolds on the fluid flow pattern by Doppler OCT" *Proceedings of the SPIE*, 75660J (2010).

2. **Y.L. Jia**, P.O. Bagnaninchi, R.K. Wang, "In situ monitoring of localized shear stress and fluid flow within developing tissue constructs by Doppler optical coherence tomography ", *Proceedings of the SPIE*, 68580G(2008).

Abstracts and Talks

1. **Y.L. Jia**, R.K. Wang, "Depth-resolved Optical Imaging of Hemodynamic Response in Mouse Brain within Macro- and Micro-circulatory Beds" SPIE Photonics West, San Francisco, CA, 2011.

2. **Y.L. Jia**, R.K. Wang, "Label-free in vivo optical imaging of functional microcirculations within meninges and cortex in mice with high sensitivity and imaging depth" SPIE Photonics West, San Francisco, CA, 2011.

3. **Y.L. Jia**, R.K. Wang, "Ultrahigh Sensitive Optical Microangiography dynamically reveals depth-resolved Microcirculations within Skeletal Muscles" SPIE Photonics West, San Francisco, CA, 2011.(Invited Talk)

4. **Y.L. Jia**, R.K. Wang, "Long-term Monitoring Cerebrovascular Response in Focal traumatic and ischemic brain injuries" SPIE Photonics West, San Francisco, CA, 2010.

5. **Y.L. Jia**, R.K. Wang, "Optical Micro-AngioGraphy detecting Angiogenesis in Brain Trauma" SPIE Photonics West, San Francisco, CA, 2010.

6. **Y.L. Jia**, R.K. Wang, "Doppler optical micro-angiography improves the quantification of local fluid flow and shear stress within 3D porous constructs " SPIE Photonics West, San Francisco, CA, 2010.

7. **Y.L. Jia**, R.K. Wang, "Noninvasive Optical Micro-AngioGraphy for structural and functional in vivo imaging of cerebro-vascular blood perfusion" SPIE Photonics West, San Jose, CA, 2009.

8. **Y.L. Jia**, R.K. Wang, "In vivo monitoring cerebral blood flow and vascular plasticity following Traumatic Brain Injury by Optical Micro AngioGraphy" SPIE Photonics West, San Jose, CA, 2009.

9. **Y.L. Jia**, R.K. Wang, "Doppler optical coherence tomography imaging of local fluid flow and shear stress within microporous scaffolds" SPIE Photonics West, San Jose, CA, 2009.

10. **Y.L. Jia**, P.O. Bagnaninchi, R.K. Wang, "The relationship between tissue development and shear stress characterized by Doppler Optical Coherence Tomography" SPIE Photonics West, San Jose, CA, 2008.

11. **Y.L. Jia**, Y. Yang, R.K. Wang, "Ultra high-resolution whole field optical coherence tomography of cell morphology and cell dynamics in three dimensional tissue models" SPIE Photonics West, San Jose, CA, 2008.